Czech Technical University in Prague

Faculty of Nuclear Sciences and Physical Engineering

Department of Physics

Doctoral Thesis

High Precision CP-Violation Measurements in Flavour Physics at the ATLAS Experiment

Prague, 2018

Ing. Tomáš Jakoubek

Bibliographic Entry

Author	Ing. Tomáš Jakoubek, Czech Technical University in Prague, Faculty of Nuclear Sciences and Physical Engineering, Department of Physics
Title of Dissertation	High Precision CP-Violation Measurements in Flavour Physics at the ATLAS Experiment
Degree Programme	Application of Natural Sciences
Field of Study	Nuclear Engineering
Supervisor	prom. fyz. Václav Vrba, CSc., Czech Technical University in Prague, Faculty of Nuclear Sciences and Physical Engineering, Department of Physics
Academic Year	2017/2018
Number of Pages	154
Keywords	ATLAS, Flavour Physics, B Physics, CP-Violation, B_s^0 meson

Bibliografický záznam

Autor	Ing. Tomáš Jakoubek, České vysoké učení technické v Praze, Fakulta jaderná a fyzikálně inženýrská, Katedra fyziky
Název práce	Přesná měření narušení CP symetrie ve flavour fyzice na experimentu ATLAS
Studijní program	Aplikace přírodních věd
Studijní obor	Jaderné inženýrství
Školitel	prom. fyz. Václav Vrba, CSc., České vysoké učení technické v Praze, Fakulta jaderná a fyzikálně inženýrská, Katedra fyziky
Akademický rok	2017/2018
Počet stran	154
Klíčová slova	ATLAS, Flavour fyzika, B fyzika, narušení CP symetrie, B_s^0 meson

Abstract

The Standard Model can not sufficiently explain the large matter-antimatter asymmetry observed in the Universe. The $B_s^0 \to J/\psi\phi$ decay channel is expected to be sensitive to possible new contributions to the CP-violation phenomena. This thesis reports the results of the high precision measurement of CP-violation parameters, including the weak phase ϕ_s and the decay width difference $\Delta\Gamma_s$, in the $B_s^0 \to J/\psi(\mu^+\mu^-)\phi(K^+K^-)$ decay in pp collisions at centre-of-mass energy of 7 TeV with 4.9 fb^{-1} and 8 TeV with 14.3 fb^{-1} of data collected using the ATLAS detector. The physical parameters are extracted using the flavour-tagged time-dependent angular analysis of the final state particles. All systematic uncertainties are carefully evaluated and thus the measurement is limited by the statistics. The 7 TeV and 8 TeV data samples are analysed separately and then statistically combined into the final result. Presented measurement is consistent with results obtained by the other experiments and with the predictions of the Standard Model as well. None of the existing results is accurate enough to exclude the possible new physics contributions to the CP-violation.

Abstrakt

Standardní model nedokáže uspokojivě vysvětlit velkou nesymetrii mezi hmotou a antihmotou pozorovanou v celém Vesmíru. V procesu $B_s^0 \to J/\psi\phi$ je narušení CP-symetrie velmi přesně předpovězeno a jakákoli odchylka od daných hodnot je jasným znakem nových fyzikálích procesů narušujících tuto symetrii. Předkládaná práce popisuje přesné měření parametrů narušení CP-symetrie v kanálu $B_s^0 \to J/\psi(\mu^+\mu^-)\phi(K^+K^-)$, včetně slabé fáze ϕ_s a rozdílu rozpadových šířek $\Delta\Gamma_s$, s použitím dat z pp srážek o energii 7 TeV a 8 TeV zaznamenaných detektorem ATLAS, o integrované luminositě 4.9 fb^{-1}, resp. 14.3 fb^{-1}. Parametry jsou určeny pomocí časově závislé úhlové analýzy koncových produktů rozpadu využívající techniku pro určování “vůní” původních částic. Všechny systematické neurčitosti byly započítány s velkou pečlivostí a tak je celková přesnost měření limitována množstvím dat. Srážky o energii 7 TeV, resp. 8 TeV byly analyzovány odděleně a měření byla poté statisticky zkombinována do konečného výsledku. Ten je konzistentní s výsledky ostatních experimentů i s předpovědí Standardního modelu. Dosud není žádné měření tak přesné, aby vyloučilo možnost nových zdrojů naručení CP-symetrie v tomto sektoru.

Acknowledgement

I would like to thank to my supervisor Václav Vrba for introducing me to the ATLAS experiment at CERN and for his invaluable help during my work and my studies.

Many thanks belong to Mária Smižanská for the leadership of our analysis group, and to all the present and former members of the group, especially to Pavel, Adam, and James, who always helped me with the problems I came across.

I am also grateful to the Institute of Physics of the Academy of Sciences of the Czech Republic and to my Alma Mater, Czech Technical University in Prague Faculty of Nuclear Sciences and Physical Engineering, for the material support and all the education they have provided me.

I would also like to thank to all my colleagues and friends, namely:

- Kuba Cúth, Peter Švihra, Radek Novotný, and Lukáš Novotný for helping with proofreading of the thesis,
- Jirka Popule for the organizational support during my work,
- Mito, Honza, Majk & Majka, Tomáš, and Jiřík for making CERN a better place to live.

Many thanks belong to all my skydiving, sailing, and skiing friends as well as all buddies from the KM training, because, as a wise man said, “Sound in body, sound in mind.”

Last but not least, I would like to thank to my parents and to my fiancée Jája for supporting me in everything I do. A warm hug belongs to our son Vašík for all the smiles, for being here with me, and for letting me sleep when I need.

Declaration

I hereby declare that I have written this thesis independently and I have used only the sources listed in the Bibliography.

In Prague, September 2018 Tomáš Jakoubek

Contents

Chapter 1

Introduction

For almost fifty years, the Standard Model of Particle Physics (SM) has been the most successful theory of fundamental particles and their interactions. It is a relativistic quantum gauge field theory formulated in its current form in 1970s. It postulates that all known matter is built from twelve fundamental fermions, their antiparticles, and three forces which govern them. Since its development the SM has passed all experimental tests and all its predictions have been confirmed with high precision. The last piece of puzzle was discovered in 2012, when the ATLAS [1] and CMS [2] experiments at the Large Hadron Collider (LHC) [3] at CERN announced their observation [4, 5] of a new particle consistent with the Higgs boson predicted by the Standard Model.

Despite its great success, the SM is in many ways an unsatisfactory theory. It has 19 free parameters, e.g. masses of the fundamental particles, whose numerical values need to be estimated by experiments. It also does not include gravitation (the fourth fundamental interaction), does not predict the existence of both dark matter and dark energy, nor explains the origin of the large dominance of matter in the universe.

The asymmetry between matter and antimatter is an example of the breakdown of symmetry under the combined application of charge conjugation C (which transforms a particle into its antiparticle) and parity P (which creates the mirror image of a physical system), also called CP-violation. It was first observed in the decays of neutral kaons by James Cronin and Val Fitch in 1964 [6].

This thesis is focused to the high precision measurement of CP-violation in the decays of neutral B_s^0 meson to $J/\psi(\mu^+\mu^-)\phi(K^+K^-)$ final state, using data collected by the ATLAS experiment at the LHC [7, 8, 9]. In this process, both B_s^0 and $\overline{B_s^0}$ mesons can decay to the same final state. The CP-violation occurs due to interference between the $B_s^0 - \overline{B_s^0}$ mixing and the direct decay amplitudes.

This decay channel is expected to be sensitive to new (unexpected) contributions to CP-violation and thus it provides an insight to a new phenomena beyond the predictions of the SM.

The thesis is structured into following chapters: chapter 2 gives a theoretical overview, including a brief summary of the SM, fundamental symmetries, CP-violation, and decays of neutral mesons. The Large Hadron Collider, the ATLAS experiment, trigger system, and computing are described in chapter 3. The author has spent many days (and nights) doing a technical work (so-called "shifts") on the ATLAS Inner Detector, which has significantly improved his knowledge and understanding of the detector, trigger, and data acquisition. By doing the shifts, the author has contributed to the *real* data-taking. Chapter 4 then gives an overview of the data used in the analysis. The author has developed the framework and was responsible for the monitoring of the B-physics data quality and for the validation of the data and B-physics triggers relevant to the analysis. Thanks to this, the large trigger bias of lifetime was discovered in early 2012 data-taking periods. The author has also contributed to the production of datasets used in the analysis. Chapter 5 provides a detailed insight into the unbinned likelihood fitting method, which is used to extract the parameters describing the CP-violation in the decay. Chapters 6, 7, and 8 are then presenting the main subject of this thesis – the measurement of the CP-violation in the $B_s^0 \to J/\psi\phi$ decay using untagged and tagged analysis of the 7 TeV data and tagged analysis of the 8 TeV data, respectively. Author's contributions are described in the next paragraphs. At the end of the thesis, in chapter 9, a statistical combination of the results is explained. Chapter 10 then concludes the thesis.

2011 Data Analysis

In the analysis of the 2011 data, the author was responsible for the optimization of the selection of a primary vertex used for the calculation of the B_s^0 meson lifetime and also for the systematic studies of the effect of primary vertex multiplicity, which was increasing during the data-taking. Another author's responsibility was to test the likelihood fit stability with increasing luminosity provided by the LHC. The author has also contributed to the preparation and testing of the alternative acceptance maps, optimization of the selection cuts, and various Monte Carlo based lifetime stability tests. In the middle of the 2011 analysis, he took the responsibility for the description and fitting of the B_s^0 tag probability distributions.

2012 Data Analysis

The author has contributed to the development and tuning of the new fitting framework for the 2012 analysis and subsequently he was responsible for the description of the B_s^0 mass background, description of the B_s^0 tag probability distributions, B_s^0 mass and lifetime uncertainty and transverse momentum distributions, their fitting and implementation into the code. The author has also taken a part in the tuning of the Monte Carlo samples to the data and has performed many systematic analysis, including the study of the effect of the mass selection cuts, estimation of the systematic uncertainties due to the selection of models used in the likelihood fit, and he partially contributed to the tagging and specific B_d^0 background systematic uncertainties estimation.

Note About the $B_s^0\pi$ Analysis

Methods and statistical treatment of data used in the presented analysis have also been used in the slightly related study *Search for tetraquark in $B_s^0\pi$ decays* [10]. This analysis uses the same decay channel ($B_s^0 \to J/\psi\phi$) and shares most of the reconstruction techniques with the CP-violation measurement, but there is no relation to the CP-violation at all. The author has spent almost two years working on this measurement as one of the main analysers. He was responsible for or contributed to almost every aspect of the analysis, beginning with the Monte Carlo models and tunings, $B_s^0\pi^\pm$ selection cuts, probability density functions and the unbinned maximum likelihood fits, calculation of yields and efficiency functions, and systematics due to fit models. The author thus thinks that the paper deserves to be at least included in the appendices.

Chapter 2

Theoretical Overview

2.1 The Standard Model

The Standard Model of Particle Physics is the most successful theory describing behaviour of elementary particles. According to this theory all known matter in the visible universe is built from twelve elementary fermions with $\frac{1}{2}$ spin: six flavours of quarks (**u**p, **d**own, **c**harm, **s**trange, **t**op, **b**ottom) and six flavours of leptons (electron e, muon μ, tau τ, and respective neutrions $\nu_{e/\mu/\tau}$). They can be grouped into three generations, each containing two quarks and two leptons, as shown in table 2.1. In addition, each elementary fermion has an antiparticle with equal mass, but with opposite electric charge. Throughout this thesis the usual particle-physics convention of natural units ($\hbar = c = 1$) is used, and thus mass and momentum are given in the energy units eV.

	Q [e]	1^{st} generation		2^{nd} generation		3^{rd} generation	
			mass		mass		mass
Leptons	-1	e	0.511 MeV	μ	105.658 MeV	τ	1776.86 ± 0.12 MeV
	0	ν_e	< 2 eV	ν_μ	< 0.19 MeV	ν_τ	< 18.2 MeV
Quarks	$+\frac{2}{3}$	u	$2.2^{+0.5}_{-0.4}$ MeV	c	$1.275^{+0.025}_{-0.035}$ GeV	t	173.0 ± 0.4 GeV
	$-\frac{1}{3}$	d	$4.7^{+0.5}_{-0.3}$ MeV	s	95^{+9}_{-3} MeV	b	$4.18^{+0.04}_{-0.03}$ GeV

Table 2.1: Generations of fundamental fermions together with their charges Q and masses. Charge is given in units of an electron charge. Data taken from [11].

All four known interactions play a role in the world of elementary particles, but only three of them (strong, weak, and electromagnetic) are included in the SM. The gravitational interaction has a negligible effect on the scale of elementary particles - it is by far the weakest of all these interactions, see table 2.2. Moreover, the gravitational interaction is described by the General relativity and not by the relativistic quantum field theory, which make it difficult to incorporate it into the SM. The fundamental interactions in the SM describe the relevant forces between the fermions by exchange of mediators – bosons, as summarized in the table 2.3.

Strong	Electromagnetic	Weak	Gravity
1	10^{-2}	10^{-7}	10^{-39}

Table 2.2: Approximate relative magnitudes of the fundamental interactions (strength of the force between protons when just in contact). Taken from [12].

2.1.1 Electromagnetic Interaction

Electromagnetic interaction is described by Quantum ElectroDynamics (QED), which is the gauge theory having the Abelian $U(1)$ symmetry. It has one free parameter, corresponding to one intermediate boson (massless photon γ). This interaction affects only particles with non-zero electric charge. Photons are massless and thus the range of the electromagnetic force is infinite (however, the potential rapidly decreases with distance $\sim \frac{1}{r}$). The strength of the electromagnetic interaction is specified by the dimensionless coupling constant

$$\alpha = \frac{e^2}{4\pi} \approx \frac{1}{137}, \tag{2.1}$$

called *the fine structure constant*, because it determines the fine structure (spin-orbit splitting) in atomic spectra.

2.1.2 Weak Interaction

Theory of a weak interaction was developed to explain observation of nuclear β-decay, but in time, it turned into a powerful and complex tool describing problems such as quark mixing and CP-violation. Weak interaction takes place between all fermions, i.e. both quarks and leptons, and is the only interaction of the SM that affects neutrinos (with no electric or strong charge). Since this interaction is a few orders of magnitude weaker (see table 2.2) and less probable (in terms of a typical cross-section σ, see table 2.3) than strong and electromagnetic interactions, it is usually drowned by them – unless these are forbidden by some conservation rule.

Weak force is mediated by massive $W^{\pm}$ and Z^0 bosons and thus the interaction acts on extremely short distance ($\sim 10^{-18}$ m [12]). Also a typical lifetime τ is significantly longer than for the strong or the electromagnetic interactions (see table 2.3). At high energies (above 100 GeV), weak and electromagnetic interactions are unified into electroweak interaction with $SU(2) \times U(1)$ symmetry. However, this symmetry is broken – the electromagnetic mediator photon is massless, while the weak mediators $W^{\pm}$ and Z^0 bosons are heavy. The spontaneous symmetry breaking is explained by a Higgs mechanism [13, 14], as an interaction with a Higgs field. An excitation of this field, the Higgs boson, was observed in 2012 at the LHC [4], [5].

Interaction	Electromagnetic	Strong	Weak
Acts on	charged particles	quarks, gluons	quarks, leptons
Source	electrical charge	colour charge	weak charge
Mediators	photon γ	8 gluons g	$W^{\pm}$, Z^0 bosons
Mass [GeV]	0	0	$m_W = 80.379 \pm 0.012$ $m_Z = 91.1876 \pm 0.0021$
Typical τ [s]	10^{-20}	10^{-23}	10^{-10}
Typical σ [m^2]	10^{-33}	10^{-30}	10^{-39}
Range [m]	∞	$< 10^{-15}$	$\sim 10^{-18}$

Table 2.3: Fundamental interactions included in the SM and their properties. Data taken from [12], mediator masses taken from [11].

The weak interaction is capable of changing *flavour* of quarks. The mixing is governed by so-called *Cabibbo-Kobayashi-Maskawa* (CKM) matrix [15]

$$V_{\mathrm{CKM}} = \begin{pmatrix} V_{ud} & V_{us} & V_{ub} \\ V_{cd} & V_{cs} & V_{cb} \\ V_{td} & V_{ts} & V_{tb} \end{pmatrix}. \tag{2.2}$$

This matrix represents the flavour change probability, hence it must be unitary. Using the standard parametrization based on a generalization of Euler-type rotations, the CKM matrix can be written as [16]

$$V_{\mathrm{CKM}} = \begin{pmatrix} 1 & 0 & 0 \\ 0 & c_2 & s_2 \\ 0 & -s_2 & c_2 \end{pmatrix} \begin{pmatrix} c_1 & s_1 & 0 \\ -s_1 & c_1 & 0 \\ 0 & 0 & e^{i\delta} \end{pmatrix} \begin{pmatrix} 1 & 0 & 0 \\ 0 & c_3 & s_3 \\ 0 & -s_3 & c_3 \end{pmatrix} = \tag{2.3}$$

$$= \begin{pmatrix} c_1 & s_1c_3 & s_1s_3 \\ -s_1c_2 & c_1c_2c_3 - s_2s_3e^{i\delta} & c_1c_2s_3 + s_2c_3e^{i\delta} \\ s_1s_2 & -c_1s_2c_3 - c_2s_3e^{i\delta} & -c_1s_2s_3 + c_2c_3e^{i\delta} \end{pmatrix}, \tag{2.4}$$

where $c_i = \cos\theta_i$, $s_i = \sin\theta_i$ for $i = 1, 2, 3$ and δ is a weak phase allowing the CP-violation in the SM. Diagonal elements of the CKM matrix are close to unity, but the off-diagonal elements are small, such that $V_{ud} \gg V_{us} \gg V_{ub}$. This fact is usually expressed in terms of the Wolfenstein parametrization [17], [18]

$$V_{\text{CKM}} = \begin{pmatrix} 1-\lambda^2/2 & \lambda & A\lambda^3(\rho - i\eta) \\ -\lambda & 1-\lambda^2/2 & A\lambda^2 \\ A\lambda^3(1-\rho-i\eta) & -A\lambda^2 & 1 \end{pmatrix} + \mathcal{O}(\lambda^4), \tag{2.5}$$

where the parameters A, ρ, and η are assumed to be of order one.

The unitarity of the CKM matrix implies $\sum_{i=1}^{3} V_{ij}V_{ik}^* = \delta_{jk}$ and $\sum_{j=1}^{3} V_{ij}V_{kj}^* = \delta_{ik}$. The six vanishing combinations can be represented as *unitarity triangles* in a complex plane as shown in figure 2.1.

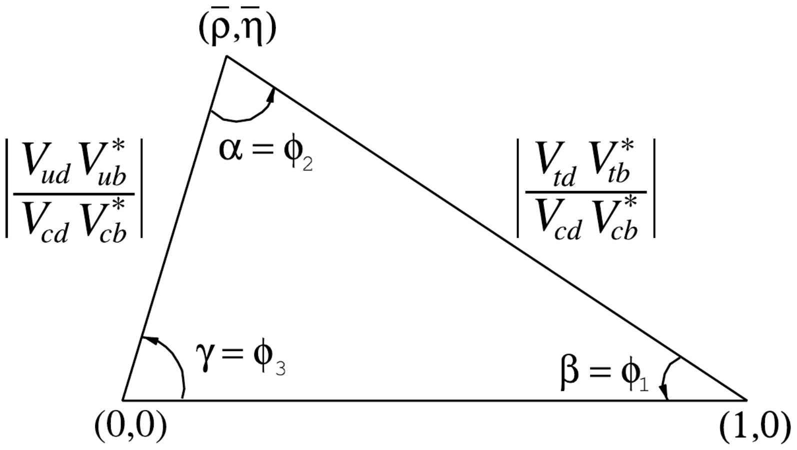

Figure 2.1: Unitarity triangle corresponding to the relation $V_{ud}V_{ub}^* + V_{cd}V_{cb}^* + V_{td}V_{tb}^* = 0$. Taken from [11].

2.1.3 Strong Interaction

Interaction, that binds quarks into hadrons (i.e. baryons, made of three quarks, and mesons, made of one quark and one antiquark), is formulated in the non-Abelian gauge theory with $SU(3)$ symmetry called Quantum ChromoDynamics (QCD). The interaction affects only particles carrying a quantum number "colour", but it does not distinguish between flavours. Mediating particles are massless gluons g.

There are three different colours and three anti-colours. A stable system bounded by the strong interaction (i.e. hadron) is formed only if a combination of constituents colour charges is zero (neutral or "white"). Gluons themselves carry a colour–anti-colour combination, and thus can interact with themselves (a crucial difference from QED, where the photon has no charge). Using three colours and three anti-colours, the total number of gluons should be 3^2; however, one of them is a colourless singlet state, leaving eight interacting gluon states.

Although the gluons are massless, the range of interaction is finite ($< 10^{-15}$ m [12]), mainly because of screening of the colour field. The coupling constant of the strong interaction can be defined with respect to a given energy scale k (running coupling)

$$\alpha_s(k^2) \equiv \frac{g_s^2(k^2)}{4\pi} \approx \frac{1}{\beta_0 \ln\left(\frac{k^2}{\Lambda_{\mathrm{QCD}}}\right)}, \tag{2.6}$$

where g_s is the strong charge of the constituent quarks, Λ_{QCD} is the scale where the perturbatively-defined coupling would diverge, and β_0 is a constant [19], [20]. At the scale of the Z^0 boson mass m_Z [11]

$$\alpha_s(m_Z^2) = 0.1181 \pm 0.0011. \tag{2.7}$$

Using equation (2.6) it is obvious that the coupling α_s becomes small for short distances or high energies with increasing k^2. The phenomenon is known as *asymptotic freedom.* On the other hand, for small k^2, as in the state of bound quarks, the α_S becomes large – so-called *colour confinement.* In hadrons, quarks move relatively freely, but if one tries to separate them, at some point it takes less energy to create a new $q\bar{q}$ pair than to resist the pulling. Thus single quarks cannot exist as free particles[1].

2.1.4 Symmetries and Conservation Laws

The Standard Model, as many other theories, is built up on symmetries. Using *local gauge symmetries* on the quantized fields describing the particles of the SM leads to a creation of *gauge fields* and corresponding intermediate bosons (described in the previous section). There are also three discrete symmetries:

---

[1] Except states of matter at extremely high temperature and density, called Quark-Gluon Plasma (QGP), where quarks and gluons become deconfined. This phase of matter is expected to exist at the very beginning of our Universe and can be recreated in head-on collisions between massive ions, such as gold or lead nuclei, as briefly described in the section 3.1.

Charge conjugation C transforms a particle into its antiparticle, reverting its electric charge and magnetic moment. Laws of QCD and QED are invariant under charge conjugation, but in the weak sector, particles and antiparticles can act differently (i.e. violate the C symmetry).

Parity inversion P creates the mirror image of a physical system, replacing each space coordinate $\mathbf{x}$ with $-\mathbf{x}$. Again, the strong and electromagnetic interactions are parity-conserving, while the weak interaction is not.

Time reversal T changes time coordinate t to $-t$ and thus reverses motion.

It was believed the combined operation of charge conjugation and parity inversion (CP) could save the symmetry in the physics laws, but that was disproved in the decays of neutral kaons by James Cronin and Val Fitch in 1964 [6]. Thus only a CPT theorem remains – it states that under combined operation of all three operators C, P, and T all interaction should be invariant. A conservation of the CPT symmetry has not yet been disproved. If it would, most physics theories and models would be invalidated.

2.2 Physics of Neutral Mesons

Neutral, weakly decaying, open-flavour[2] mesons can oscillate into their antiparticles and vice versa. This is also referred as neutral meson mixing. In the SM, these processes are described by *box diagrams*, as shown in figure 2.2, where mixing between mesons $B_s^0 = s\bar{b}$ and $\overline{B_s^0} = b\bar{s}$ is presented.

Following [11], the state $|\psi(t)\rangle$ of the $B_s^0 - \overline{B_s^0}$ system at time t is a superposition of $|B_s^0\rangle$ and $|\overline{B_s^0}\rangle$ states

$$|\psi(t)\rangle = a(t)|B_s^0\rangle + b(t)|\overline{B_s^0}\rangle, \tag{2.8}$$

where the time evolution operators $a(t)$ and $b(t)$ are governed by the time dependent Schrödinger equation

$$i\hbar\frac{\partial}{\partial t}\psi(t) = \mathbf{H}\psi(t), \tag{2.9}$$

where $\mathbf{H}$ is simplified 2×2 Hamiltonian, which can be expressed as a sum of two Hermitian matrices $\mathbf{M}$ and $\mathbf{\Gamma}$

$$\mathbf{H} = \mathbf{M} - \frac{i}{2}\mathbf{\Gamma} = \begin{pmatrix} M_{11} & M_{12} \\ M_{12}^* & M_{22} \end{pmatrix} - \frac{i}{2}\begin{pmatrix} \Gamma_{11} & \Gamma_{12} \\ \Gamma_{12}^* & \Gamma_{22} \end{pmatrix}. \tag{2.10}$$

---

[2] i.e. not a $q\bar{q}$ pair.

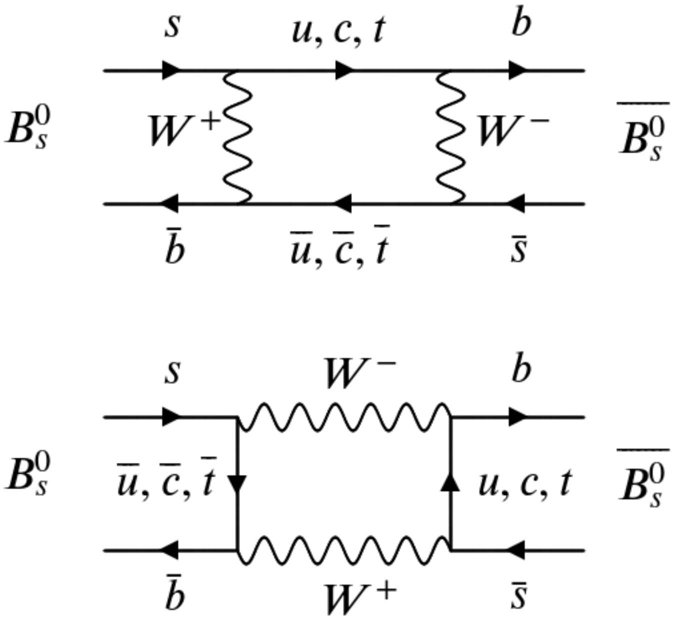

Figure 2.2: Feynman diagrams showing $B_s^0 - \overline{B_s^0}$ mixing.

However, the matrix **H** is *not* Hermitian, otherwise the mesons would only oscillate and not decay. Assuming CPT is conserved, the Hamiltonian **H** can be simplified using $M_{11} = M_{22} = M$ and $\Gamma_{11} = \Gamma_{22} = \Gamma$. Equation (2.9) can be solved by diagonalizing the matrix **H** – the equations decouple and the two mass eigenstates B_L (**L**ight) and B_H (**H**eavy) of the B_s^0 system can be written as

$$|B_L\rangle \equiv p|B_s^0\rangle + q|\overline{B_s^0}\rangle \tag{2.11}$$

$$|B_H\rangle \equiv p|B_s^0\rangle - q|\overline{B_s^0}\rangle, \tag{2.12}$$

where the two complex parameters follow $|p|^2 + |q|^2 = 1$ to normalize the wave function and

$$\left(\frac{q}{p}\right)^2 = \frac{M_{12}^* - \frac{i}{2}\Gamma_{12}^*}{M_{12} - \frac{i}{2}\Gamma_{12}}. \tag{2.13}$$

The real and imaginary parts of the eigenvalues

$$\omega_{L,H} = M - \frac{i}{2}\Gamma \pm \frac{q}{p}\left(M_{12} - \frac{i}{2}\Gamma_{12}\right), \tag{2.14}$$

corresponding to $|B_{L,H}\rangle$, represent their masses and decay widths. The differences between the widths $\Gamma_{L,H}$ and masses $m_{L,H}$ of the two mass eigenstates $B_{L,H}$ are defined as

$$\Delta m_s \equiv m_H - m_L = \mathcal{R}e(\omega_H - \omega_L) \tag{2.15}$$

$$\Delta\Gamma_s \equiv \Gamma_L - \Gamma_H = -2\mathcal{I}m(\omega_H - \omega_L). \tag{2.16}$$

Here Δm_s is positive by definition, but the sign of $\Delta\Gamma_s$ must be experimentally determined. It is predicted to be positive in the SM and this was also confirmed by the LHCb experiment [21].

2.2.1 Time Evolution

Solution of the equation (2.9) yields in a simple exponential form describing the evolution of the mass eigenstates in time t

$$|B_L(t)\rangle = e^{-i(m_L - \frac{i}{2}\Gamma_L)t}|B_L(0)\rangle, \tag{2.17}$$

$$|B_H(t)\rangle = e^{-i(m_H - \frac{i}{2}\Gamma_H)t}|B_H(0)\rangle. \tag{2.18}$$

Time evolution for flavour eigenstates B_s^0 and $\overline{B_s^0}$ can be obtained from equation (2.18) using equation (2.12)

$$|B_s^0(t)\rangle = g_+(t)|B_s^0(0)\rangle - \frac{q}{p}g_-(t)|\overline{B_s^0}(0)\rangle, \tag{2.19}$$

$$|\overline{B_s^0}(t)\rangle = g_+(t)|\overline{B_s^0}(0)\rangle - \frac{p}{q}g_-(t)|B_s^0(0)\rangle, \tag{2.20}$$

where

$$g_\pm(t) = \frac{1}{2}\left(e^{-im_Ht - \frac{1}{2}\Gamma_H t} \pm e^{-im_Lt - \frac{1}{2}\Gamma_L t}\right). \tag{2.21}$$

Time evolution of B_s^0mesons (2.18) is often expressed in terms of the mass difference Δm_s, the decay width difference $\Delta\Gamma_s$, the average mass $m_s = \frac{1}{2}(m_L + m_H)$, and the decay width $\Gamma_s = \frac{1}{2}(\Gamma_L + \Gamma_H)$ as follows

$$g_\pm(t) = \frac{1}{2}e^{-im_st - \frac{1}{2}\Gamma_s t}\left(e^{-\frac{i\Delta m_s t}{2} + \frac{\Delta\Gamma_s t}{4}} \pm e^{\frac{i\Delta m_s t}{2} - \frac{\Delta\Gamma_s t}{4}}\right). \tag{2.22}$$

Decay amplitudes of the B_s^0 ($\overline{B_s^0}$) meson to final state f ($\bar{f}$) can be defined as

$$\begin{aligned} A_f &= \langle f|\mathcal{H}|B_s^0\rangle, & \bar{A}_f &= \langle f|\mathcal{H}|\overline{B_s^0}\rangle, \\ A_{\bar{f}} &= \langle \bar{f}|\mathcal{H}|B_s^0\rangle, & \bar{A}_{\bar{f}} &= \langle \bar{f}|\mathcal{H}|\overline{B_s^0}\rangle, \end{aligned} \tag{2.23}$$

where $\mathcal{H}$ is a weak interaction Hamiltonian. Then, taking equations (2.19), (2.20), (2.22) and substituting them into A_f and $\bar{A}_f$, one can obtain time-dependent decay rates

$$\begin{aligned}\frac{\mathrm{d}\Gamma(B_s^0 \to f)}{\mathrm{d}t} = \mathcal{N}_f e^{-\Gamma_s t} \Bigg[& \left(|A_f|^2 + |(q/p)\bar{A}_f|^2\right) \cosh\left(\frac{\Delta\Gamma_s t}{2}\right) \\ & + \left(|A_f|^2 - |(q/p)\bar{A}_f|^2\right) \cos\left(\Delta m_s t\right) \\ & + 2\mathcal{R}e\left((q/p)A_f^*\bar{A}_f\right) \sinh\left(\frac{\Delta\Gamma_s t}{2}\right) \\ & - 2\mathcal{I}m\left((q/p)A_f^*\bar{A}_f\right) \sin\left(\Delta m_s t\right)\Bigg], \end{aligned} \tag{2.24}$$

$$\begin{aligned}\frac{\mathrm{d}\Gamma(\overline{B_s^0} \to f)}{\mathrm{d}t} = \mathcal{N}_f e^{-\Gamma_s t} \Bigg[& \left(|(p/q)A_f|^2 + |\bar{A}_f|^2\right) \cosh\left(\frac{\Delta\Gamma_s t}{2}\right) \\ & - \left(|(p/q)A_f|^2 - |\bar{A}_f|^2\right) \cos\left(\Delta m_s t\right) \\ & + 2\mathcal{R}e\left((p/q)A_f\bar{A}_f^*\right) \sinh\left(\frac{\Delta\Gamma_s t}{2}\right) \\ & - 2\mathcal{I}m\left((p/q)A_f\bar{A}_f^*\right) \sin\left(\Delta m_s t\right)\Bigg], \end{aligned} \tag{2.25}$$

where $\mathcal{N}_f$ is a common, time-independent, normalization factor. Decay rates $\frac{\mathrm{d}\Gamma(B_s^0\to\bar{f})}{\mathrm{d}t}$ and $\frac{\mathrm{d}\Gamma(\overline{B_s^0}\to\bar{f})}{\mathrm{d}t}$ can be derived analogously, using $\mathcal{N}_f = \mathcal{N}_{\bar{f}}$, $A_f \to A_{\bar{f}}$, and $\bar{A}_f \to \bar{A}_{\bar{f}}$.

Terms with $|A_f|^2$ or $|\bar{A}_f|^2$ correspond to decays without any $B_s^0 - \overline{B_s^0}$ oscillation, while terms with $|(p/q)A_f|^2$ or $|(q/p)\bar{A}_f|^2$ correspond to decays following the oscillation. Terms with $\sinh\left(\frac{\Delta\Gamma_s t}{2}\right)$ and $\sin\left(\Delta m_s t\right)$ are connected with the interference between direct decays and decays following oscillations. Any difference in the decay rate from equation (2.24) and equation (2.25) indicates CP-violation. These decay rates are valid for all neutral meson systems, not only for $B_s^0 - \overline{B_s^0}$.

2.2.2 Types of CP-Violation

We distinguish three different types of CP-violation according to the various sources from which it emerges. The classification has been developed for B decays but it can be used for decays of all mesons M.

CP**-violation in decay** (or direct CP-violation) is defined by

$$\left|\frac{\bar{A}_{\bar{f}}}{A_f}\right| \neq 1, \tag{2.26}$$

i.e. the decay amplitudes of $B_s^0 \to f$ and $\overline{B_s^0} \to \bar{f}$ are different. This is the only possible CP-violating effect in the decay of charged mesons.

CP-violation in mixing (or indirect CP-violation) is defined by

$$\left|\frac{q}{p}\right| \neq 1, \tag{2.27}$$

which means there is an asymmetry in the $B_s^0 - \overline{B_s^0}$ oscillations. It also means the CP-eigenstates are not equivalent to the mass eigenstates.

Mixing-induced CP-violation (sometimes called CP-violation in interference between a decay without mixing and a decay with mixing) is possible only if B_s^0 and $\overline{B_s^0}$ decay into the same final state f, i.e. the final state is reached via two different decay chains $B_s^0 \to f$ and $B_s^0 \to \overline{B_s^0} \to f$. It is defined by

$$\mathcal{I}m\,(\lambda_f) \neq 0, \tag{2.28}$$

where

$$\lambda_f = \frac{q}{p} \cdot \frac{\bar{A}_f}{A_f}. \tag{2.29}$$

The SM prediction of CP-violation in mixing for the $B_s^0 \to J/\psi\phi$ decay is $\left|\frac{q}{p}\right| = 1 + \mathcal{O}(10^{-3})$ and an upper limit has been estimated to be $\left|\frac{q}{p}\right| = 1.0003 \pm 0.0014$ [22]. Also a direct CP-violation in this decay is strongly suppressed [23] and thus the CP-violation in the $B_s^0 \to J/\psi\phi$ channel happens via interference of mixing and decay, as schematically shown in figure 2.3.

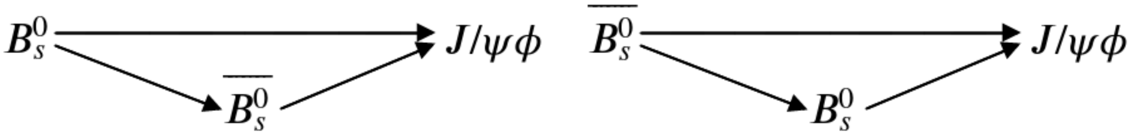

Figure 2.3: Interference between mixing and decay in the $B_s^0 - \overline{B_s^0}$ system.

2.2.3 CP-violation in the $B_s^0 \to J/\psi\phi$ decay

The decay of the B_s^0 meson into $J/\psi = c\bar{c}$ and $\phi = s\bar{s}$ mesons is in fact transition $b \to c\bar{c}\bar{s}$. Feynman diagrams of the tree level (t_f) and penguin (p_f^q) processes contributing to this transition are shown in figure 2.4. The same diagrams for the $\overline{B_s^0}$ decay can be derived by replacing all particles by their antiparticles. The total decay amplitude

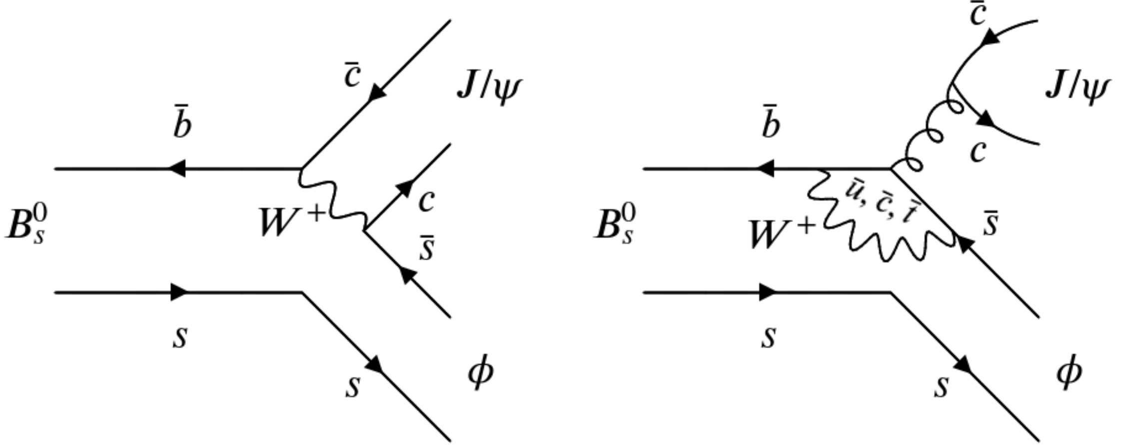

Figure 2.4: Tree (left) and penguin (right) Feynman diagrams contributing to the decay $B_s^0 \to J/\psi\phi$ within the SM.

A_f must be a function of both processes

$$A_f = (V_{cb}^* V_{cs}) t_f + \sum_{q=u,c,t} (V_{qb}^* V_{qs}) p_f^q, \tag{2.30}$$

where f denotes the final state $J/\psi\phi$. Using the CKM unitarity

$$\sum_{q=u,c,t} (V_{qb}^* V_{qs}) = 0, \tag{2.31}$$

equation (2.30) can be rewritten as

$$A_f = (V_{cb}^* V_{cs})(t_f + p_f^c - p_f^t) + (V_{ub}^* V_{us})(p_f^u - p_f^t). \tag{2.32}$$

The second term in equation (2.32) is suppressed because of $\frac{V_{ub}^* V_{us}}{V_{cb}^* V_{cs}} \sim \mathcal{O}(\lambda^2)$ (see the Wolfenstein parametrization of the CKM matrix given in equation (2.5)) and thus the effect of the penguin amplitude is expected to be very small [18]. Then, the ratio of decay amplitudes can be written as

$$\frac{\bar{A}_f}{A_f} = -\eta_f^{CP} \frac{V_{cb} V_{cs}^*}{V_{cb}^* V_{cs}}, \tag{2.33}$$

where $\eta_f^{CP} = +1$ for CP-even and $\eta_f^{CP} = -1$ for CP-odd final states.

In the SM, a ratio $\frac{q}{p} = -\frac{V_{ts} V_{tb}^*}{V_{ts}^* V_{tb}}$ to a good approximation [18] and thus using equation (2.33) in equation (2.29), where $f = J/\psi\phi$, one can obtain a parameter describing CP-violation in interference between mixing and decay for $B_s^0 \to J/\psi\phi$

$$\lambda_{J/\psi\phi} \approx \eta_{J/\psi\phi}^{CP} \frac{V_{ts}V_{tb}^* V_{cb} V_{cs}^*}{V_{ts}^* V_{tb} V_{cb}^* V_{cs}} = \eta_{J/\psi\phi}^{CP} e^{2i\beta_s} = \eta_{J/\psi\phi}^{CP} e^{-i\phi_s}, \tag{2.34}$$

where the weak phase ϕ_s is defined using an unitarity triangle $V_{us}V_{ub}^* + V_{cs}V_{cb}^* + V_{ts}V_{tb}^* = 0$ as

$$\phi_s \simeq -2\beta_s = -2\arg\left(-\frac{V_{ts}V_{tb}^*}{V_{cs}V_{cb}^*}\right). \tag{2.35}$$

The weak phase ϕ_s is the parameter determining the amount of CP-violation in the $B_s^0 \to J/\psi\phi$ decay. The SM prediction for this parameter is [24]

$$\phi_s^{\mathrm{SM}} = -0.0363^{+0.0016}_{-0.0015} \text{ rad.} \tag{2.36}$$

New phenomena beyond the predictions of the Standard Model could introduce additional contributions to the box diagrams describing the $B_s^0 - \overline{B_s^0}$ mixing and thus a sizeable deviation from the ϕ_s^{SM} value given in equation (2.36) would be a clear sign of the beyond Standard Model physics.

2.2.4 Transversity Formalism and Angular Analysis

The decay of the pseudoscalar B_s^0 to the vector-vector final state $J/\psi\phi$, followed by $J/\psi \to \mu^+\mu^-$ and $\phi \to K^+K^-$, results in an admixture of CP-odd (with orbital angular momentum $L = 1$) and CP-even ($L = 0, 2$) states. The CP states can be separated statistically using an angular analysis of the final-state particles. The following text defines the transversity basis, which is most suited to study CP-violation in time-dependent asymmetries in B_s^0 decays.

In this formalism, the spin of one daughter particle is projected onto the normal of the other daughter's decay plane and the decay amplitudes are decomposed using three independent linear polarization states A_0, $A_\perp$, and $A_\parallel$ of the vector mesons. For A_0 the spins of the vector particles are polarized longitudinally with respect to their momentum, for $A_\perp$ spins are perpendicular to each other, and for $A_\parallel$ they are parallel to each other. A linear combination of $A_\parallel$ and A_0 corresponds to the CP-even states and $A_\perp$ to the CP-odd state.

The transversity angles $(\theta_T, \psi_T, \phi_T)$ are defined in the rest frames of the final-state particles. The x-axis is determined by the direction of the ϕ meson in the J/ψ rest frame, and the K^+K^- system defines the x–y plane, where a y-component of the momentum $p_y(K^+) > 0$. The three angles are defined as:

- θ_T, the angle between the momentum $\mathbf{p}(\mu^+)$ and the normal to the x–y plane, in the J/ψ meson rest frame,

- ϕ_T, the angle between the x-axis and the momentum $\mathbf{p}_{xy}(\mu^+)$, the projection of the μ^+ momentum in the x–y plane, in the J/ψ meson rest frame,
- ψ_T, the angle between momentum $\mathbf{p}(K^+)$ and $-\mathbf{p}(J/\psi)$ in the ϕ meson rest frame.

These angles are schematically shown in figure 2.5. For each of the transversity amplitudes there is an associated phase: $\delta_0 = \arg(A_0)$, $\delta_\perp = \arg(A_\perp)$, and $\delta_\parallel = \arg(A_\parallel)$. Phase δ_0 is by convention set to be zero, since only phase differences between the amplitudes appear in the differential decay rate described in the next section.

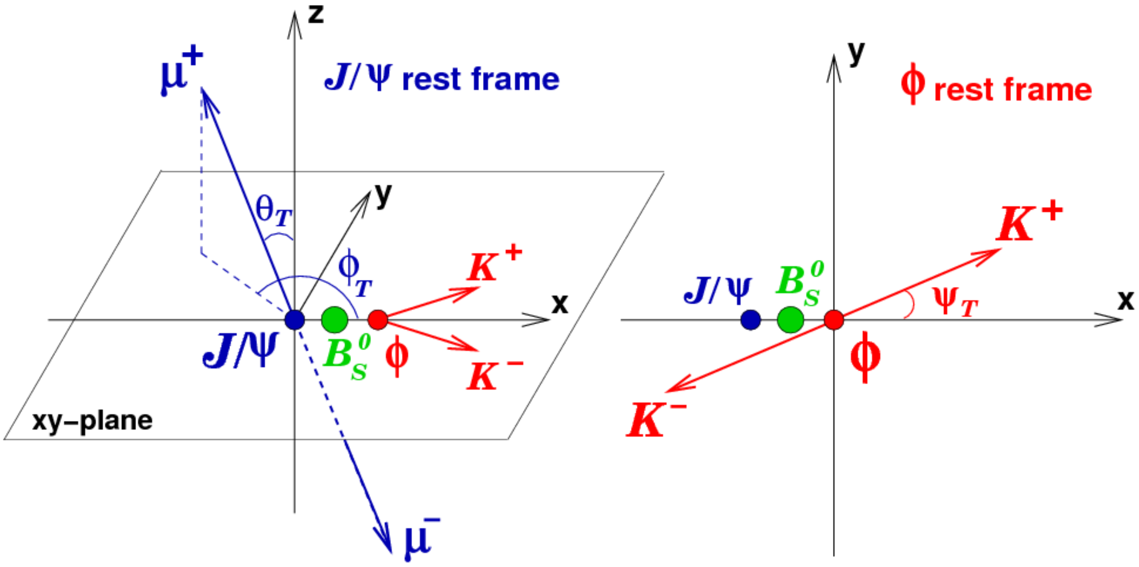

Figure 2.5: Illustration of the transversity angles between the final state particles in the $B_s^0 \to J/\psi\phi$ decay. Taken from [25].

2.2.5 Time-dependent Decay Rate

The previous sections describes the primary contributions from the orbital P-wave amplitudes. However, the same final state $\mu^+\mu^-K^+K^-$ can be reached via two other processes, that cannot be identified in the measured data. The first contribution is from $B_s^0 \to J/\psi f_0$ (with $f_0 \to K^+K^-$) decay and the second from the non-resonant $B_s^0 \to J/\psi K^+K^-$ decay. These S-wave states are CP-odd and can significantly bias the measurement of ϕ_s. Thus they have to be included in the final description of the decay, using their own amplitude A_S and phase δ_S.

The distribution for the time t and the transversity angles $\Omega(\theta_T, \psi_T, \phi_T)$ is given by the differential decay rate, derived in [26] and more generally in [18], as

$$\frac{\mathrm{d}^4\Gamma}{\mathrm{d}t\ \mathrm{d}\Omega} = \sum_{k=1}^{10} \mathcal{O}^{(k)}(t) g^{(k)}(\theta_T, \psi_T, \phi_T), \tag{2.37}$$

where $\mathcal{O}^{(k)}(t)$ are the time-dependent functions corresponding to the contributions of the four different amplitudes (A_0, $A_\parallel$, $A_\perp$, and A_S) and their interference terms, as shown in table 2.4. The angular functions $g^{(k)}(\theta_T, \psi_T, \phi_T)$ are defined in table 2.5. The formulae for the time-dependent functions have the same structure for B_s^0 and $\overline{B_s^0}$, but with a sign reversal in the terms containing Δm_s.

k	$\mathcal{O}^{(k)}(t)$
1	$\frac{1}{2}\lvert A_0(0)\rvert^2 \left[(1+\cos\phi_s)\, e^{-\Gamma_{\mathrm{L}}^{(s)}t} + (1-\cos\phi_s)\, e^{-\Gamma_{\mathrm{H}}^{(s)}t} \pm 2e^{-\Gamma_s t}\sin(\Delta m_s t)\sin\phi_s\right]$
2	$\frac{1}{2}\lvert A_\parallel(0)\rvert^2 \left[(1+\cos\phi_s)\, e^{-\Gamma_{\mathrm{L}}^{(s)}t} + (1-\cos\phi_s)\, e^{-\Gamma_{\mathrm{H}}^{(s)}t} \pm 2e^{-\Gamma_s t}\sin(\Delta m_s t)\sin\phi_s\right]$
3	$\frac{1}{2}\lvert A_\perp(0)\rvert^2 \left[(1-\cos\phi_s)\, e^{-\Gamma_{\mathrm{L}}^{(s)}t} + (1+\cos\phi_s)\, e^{-\Gamma_{\mathrm{H}}^{(s)}t} \mp 2e^{-\Gamma_s t}\sin(\Delta m_s t)\sin\phi_s\right]$
4	$\frac{1}{2}\lvert A_0(0)\rvert\lvert A_\parallel(0)\rvert\cos\delta_\parallel \left[(1+\cos\phi_s)\, e^{-\Gamma_{\mathrm{L}}^{(s)}t} + (1-\cos\phi_s)\, e^{-\Gamma_{\mathrm{H}}^{(s)}t} \pm 2e^{-\Gamma_s t}\sin(\Delta m_s t)\sin\phi_s\right]$
5	$\lvert A_\parallel(0)\rvert\lvert A_\perp(0)\rvert[\frac{1}{2}(e^{-\Gamma_{\mathrm{L}}^{(s)}t} - e^{-\Gamma_{\mathrm{H}}^{(s)}t})\cos(\delta_\perp-\delta_\parallel)\sin\phi_s \pm e^{-\Gamma_s t}(\sin(\delta_\perp-\delta_\parallel)\cos(\Delta m_s t) - \cos(\delta_\perp-\delta_\parallel)\cos\phi_s\sin(\Delta m_s t))]$
6	$\lvert A_0(0)\rvert\lvert A_\perp(0)\rvert[\frac{1}{2}(e^{-\Gamma_{\mathrm{L}}^{(s)}t} - e^{-\Gamma_{\mathrm{H}}^{(s)}t})\cos\delta_\perp\sin\phi_s \pm e^{-\Gamma_s t}(\sin\delta_\perp\cos(\Delta m_s t) - \cos\delta_\perp\cos\phi_s\sin(\Delta m_s t))]$
7	$\frac{1}{2}\lvert A_S(0)\rvert^2 \left[(1-\cos\phi_s)\, e^{-\Gamma_{\mathrm{L}}^{(s)}t} + (1+\cos\phi_s)\, e^{-\Gamma_{\mathrm{H}}^{(s)}t} \mp 2e^{-\Gamma_s t}\sin(\Delta m_s t)\sin\phi_s\right]$
8	$\lvert A_S(0)\rvert\lvert A_\parallel(0)\rvert[\frac{1}{2}(e^{-\Gamma_{\mathrm{L}}^{(s)}t} - e^{-\Gamma_{\mathrm{H}}^{(s)}t})\sin(\delta_\parallel-\delta_S)\sin\phi_s \pm e^{-\Gamma_s t}(\cos(\delta_\parallel-\delta_S)\cos(\Delta m_s t) - \sin(\delta_\parallel-\delta_S)\cos\phi_s\sin(\Delta m_s t))]$
9	$\frac{1}{2}\lvert A_S(0)\rvert\lvert A_\perp(0)\rvert\sin(\delta_\perp-\delta_S) \left[(1-\cos\phi_s)\, e^{-\Gamma_{\mathrm{L}}^{(s)}t} + (1+\cos\phi_s)\, e^{-\Gamma_{\mathrm{H}}^{(s)}t} \mp 2e^{-\Gamma_s t}\sin(\Delta m_s t)\sin\phi_s\right]$
10	$\lvert A_0(0)\rvert\lvert A_S(0)\rvert[\frac{1}{2}(e^{-\Gamma_{\mathrm{H}}^{(s)}t} - e^{-\Gamma_{\mathrm{L}}^{(s)}t})\sin\delta_S\sin\phi_s \pm e^{-\Gamma_s t}(\cos\delta_S\cos(\Delta m_s t) + \sin\delta_S\cos\phi_s\sin(\Delta m_s t))]$

Table 2.4: Table showing the ten time-dependent functions $\mathcal{O}^{(k)}(t)$ for the $B_s^0 \to J/\psi\phi$ decay. The ± and ∓ terms denote two cases: the upper sign describes the decay of a meson that was initially a B_s^0 meson, while the lower sign describes the decays of a meson that was initially $\overline{B_s^0}$ meson. Corresponding transversity angles $g^{(k)}(\theta_T, \psi_T, \phi_T)$ are shown in table 2.5.

k	$g^{(k)}(\theta_T, \psi_T, \phi_T)$
1	$2\cos^2\psi_T(1-\sin^2\theta_T\cos^2\phi_T)$
2	$\sin^2\psi_T(1-\sin^2\theta_T\sin^2\phi_T)$
3	$\sin^2\psi_T\sin^2\theta_T$
4	$\frac{1}{\sqrt{2}}\sin 2\psi_T\sin^2\theta_T\sin 2\phi_T$
5	$-\sin^2\psi_T\sin 2\theta_T\sin\phi_T$
6	$\frac{1}{\sqrt{2}}\sin 2\psi_T\sin 2\theta_T\cos\phi_T$
7	$\frac{2}{3}\left(1-\sin^2\theta_T\cos^2\phi_T\right)$
8	$\frac{1}{3}\sqrt{6}\sin\psi_T\sin^2\theta_T\sin 2\phi_T$
9	$\frac{1}{3}\sqrt{6}\sin\psi_T\sin 2\theta_T\cos\phi_T$
10	$\frac{4}{3}\sqrt{3}\cos\psi_T\left(1-\sin^2\theta_T\cos^2\phi_T\right)$

Table 2.5: Table showing the ten functions of the transversity angles $g^{(k)}(\theta_T, \psi_T, \phi_T)$ corresponding to the time-dependent functions $\mathcal{O}^{(k)}(t)$ in table 2.4.

2.3 Current Experimental Status

CP-violation parameters in the B_s^0 decay have been previously[3] measured by the D0, CDF, and LHCb experiments, as summarized in table 2.6. All measurements, as well as the combined result calculated by Heavy Flavour Averaging Group (HFLAG), are consistent with the SM expectation. 68 % CL contours in the $\phi_s - \Delta\Gamma_s$ plane obtained from individual and combined D0, CDF, and LHCb measurements are shown in figure 2.6.

	ϕ_s [rad]	$\Delta\Gamma_s[\mathrm{ps}^{-1}]$	Ref.
D0	$-0.55^{+0.38}_{-0.36}$	$0.163^{+0.065}_{-0.064}$	[27]
CDF	$[-0.60, 0.12]$, 68 % CL	$0.068 \pm 0.026 \pm 0.009$	[28]
LHCb	$-0.001 \pm 0.101 \pm 0.027$	$0.116 \pm 0.018 \pm 0.006$	[29], update [30]
HFLAG	$-0.044^{+0.090}_{-0.085}$	0.105 ± 0.015	[31]

Table 2.6: Summarized results of $B_s^0 \to J/\psi\phi$ CP-violation measurements from D0, CDF, and LHCb experiments. The first error is due to statistics, the second one to systematics. HFLAG combined result is based also on the LHCb $B_s^0 \to J/\psi\pi\pi$ measurement. Only measurements published before the first ATLAS $B_s^0 \to J/\psi\phi$ paper [7] are included.

---

[3] Before the first ATLAS $B_s^0 \to J/\psi\phi$ paper [7] was published.

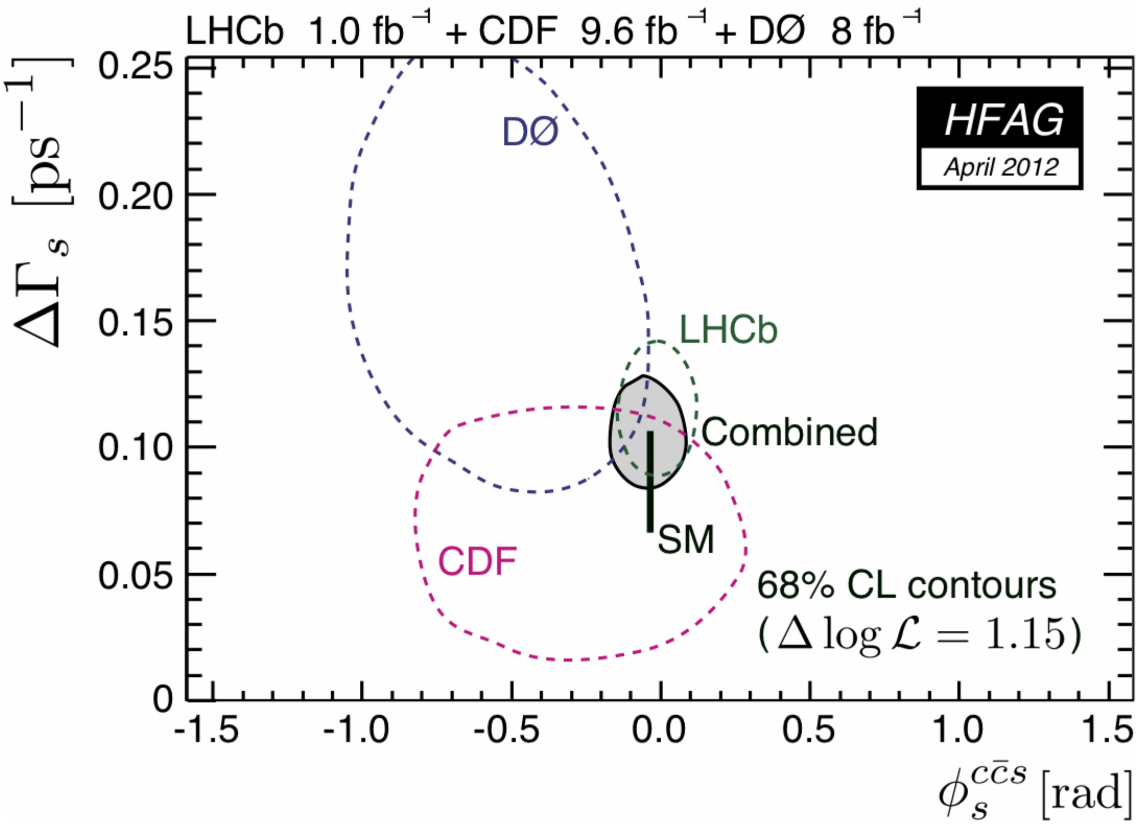

Figure 2.6: 68 % CL regions in B_s^0 width difference $\Delta\Gamma_s$ and weak phase ϕ_s obtained from individual and combined D0, CDF, and LHCb measurements. Only measurements published before the first ATLAS $B_s^0 \to J/\psi\phi$ paper [7] are included. The SM expectation is shown as the black rectangle. Taken from [31].

Chapter 3

The ATLAS Experiment

3.1 The Large Hadron Collider

The Large Hadron Collider (LHC) [3] is a synchrotron completed at CERN (near Geneva, Switzerland) in 2008, in the same 27 km long underground tunnel where the Large Electron-Positron collider (LEP) resided until 2001. Currently, it is the world's largest particle accelerator. The LHC was designed for pp collisions with the centre-of-mass energy of 14 TeV and also heavy ion collisions using lead Pb^{82+} with 2.56 TeV/nucleon. The machine started its operation at 450 GeV/beam in 2008, then moved to 1.18 TeV/beam in 2009 and thus become the world's most powerful particle accelerator. In 2010, energy was increased to 3.5 TeV/beam and to 4 TeV/beam in 2012. After two years break, the LHC was restarted in 2015 with energy 6.5 TeV/beam and it is running at this level until now (mid of 2018) [32].

The LHC makes use of a large variety of magnets, including dipoles, quadrupoles, sextupoles, octupoles, etc. giving a total of about 9600 magnets. Each type of magnet contributes to optimizing a particle's trajectory. The biggest magnets are the 1232 superconducting dipoles providing 8.33 T field and operating at temperature 1.9 K [33]. These magnets need to be "trained" before each energy increase [34].

In addition to the greatest energy, the LHC has also reached the greatest luminosity – number of collisions per time – defined as

$$\mathscr{L} = f_{\mathrm{rev}} \frac{n_b \cdot n_1 \cdot n_2}{4\pi \cdot \sigma_x \sigma_y}, \tag{3.1}$$

where f_{rev} is the revolution frequency, n_b is number of bunches, $n_{1,2}$ are numbers of particles in each bunch, and $\sigma_{x,y}$ are the profiles of the beam as a Gaussian distribution in the vertical and horizontal directions. LHC was designed to $\mathscr{L} = 10^{34}$ cm^{-2} s^{-1}, but already during 2017 this value increased to 2.06×10^{34} cm^{-2} s^{-1}

(twice the nominal value) [35]. Moreover, in 2017 first xenon nuclei Xe^{54+} were successfully injected, accelerated and collided with energy 2.72 TeV/nucleon [36].

Proton beams colliding in the LHC are formed from 2808 bunches (designed value which can vary from run to run; the highest value is currently 2544 bunches), each of them containing $\sim 1.15 \times 10^{11}$ protons. Bunches are separated by 25 ns, i.e. with the bunch crossing rate 40 MHz. Each beam is created by passing hydrogen through a magnetic field, ionising the gas and injecting protons into Linac2, where they are accelerated to 50 MeV. Then they are injected into the Proton Synchrotron Booster (PSB), which accelerates them to 1.4 GeV and injects the proton beam into the Proton Synchrotron (PS), where it is accelerated to 25 GeV. Protons are then sent to the Super Proton Synchrotron (SPS), where they are accelerated to 450 GeV and finally transferred to the LHC (both in a clockwise and an anticlockwise direction) where they are accelerated to the final energy. The accelerator chain is shown in figure 3.1. In the LHC itself the beams are powered by using superconducting radio-frequency cavities (eight cavities per beam, each delivering 2 MV at 400 MHz) and then kept on the orbit using almost 9600 magnets [33].

There are four major experiments (detectors) along the course of the LHC ring (their locations are also shown in figure 3.1):

ALICE (**A** **L**arge **I**on **C**ollider **E**xperiment) is a detector specialized in analysing heavy ion collisions and studying the properties of QGP.

ATLAS (**A** **T**oroidal **L**HC **A**pparatu**S**) is a general-purpose detector designed to cover the widest possible range of physics at the LHC. ATLAS is the largest collider detector ever constructed. Its parts will be described in following sections.

LHC*b* (**L**arge **H**adron **C**ollider **b**eauty) specializes in the study of the slight asymmetry between matter and antimatter present in interactions of B mesons.

CMS (**C**ompact **M**uon **S**olenoid) is also a general-purpose detector, optimized for tracking muons. The word “compact” means that is smaller than the ATLAS detector. CMS and ATLAS have the same physics goals, but different technical solutions and design. They can independently confirm the results flowing from the same physical phenomena and reduce systematic and random errors.

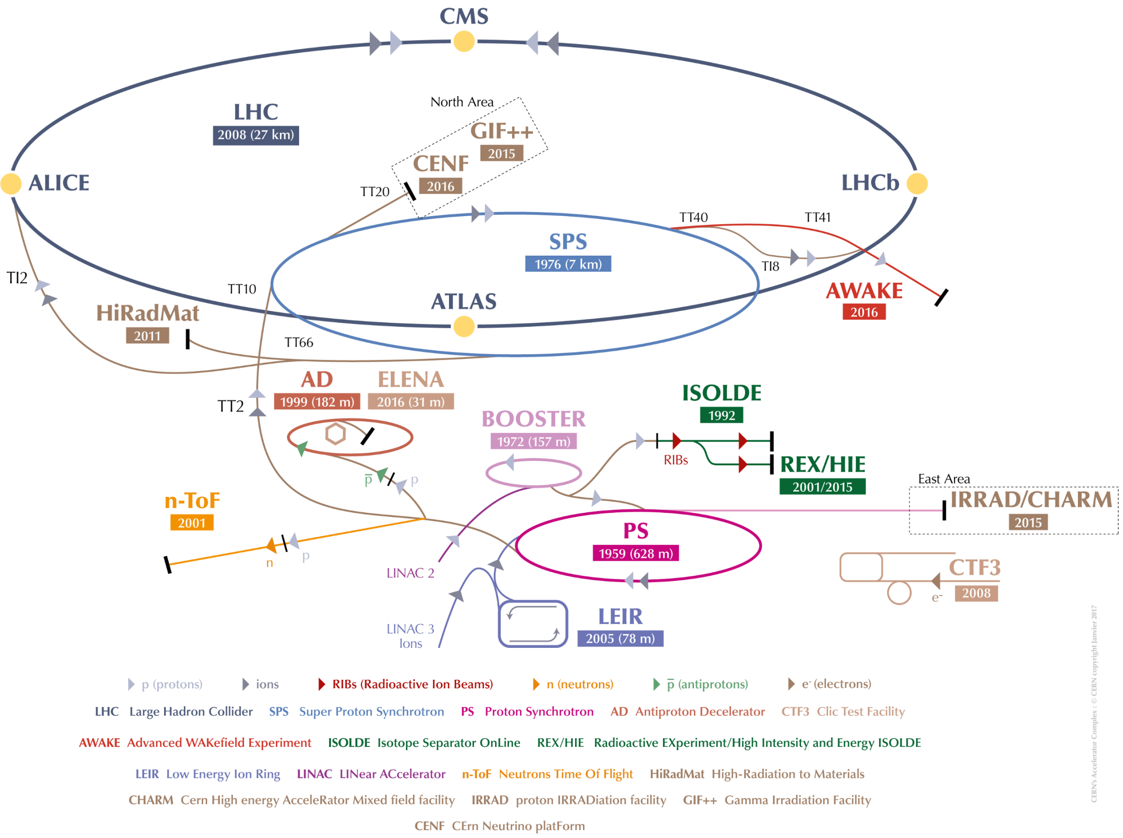

Figure 3.1: Schematic view of the CERN accelerators complex, including locations of experimental areas and major LHC detectors. Taken from [37].

3.2 The ATLAS Detector

ATLAS is the largest particle detector for a collider ever built: it is 46 m long, 26 m in diameter and weighs 7000 tonnes. It is a general-purpose detector with a broad physics program. The most famous of the ATLAS achievements is the Higgs boson discovery, but it is not the only one. There are searches for New Physics phenomena like supersymmetry, extra dimensions or dark matter, precision measurements of the SM parameters like masses of gauge bosons, CKM matrix elements, and of course, CP-violation.

The ATLAS detector consists of four major components: the Inner Detector, providing an efficient tracking of all charged particles, electromagnetic and hadronic calorimetry systems which measure the energies carried by the particles, the muon spectrometer to identify and measure muons and the magnet system. These will be described in next sections. A schematic view of the whole detector with all mentioned components is shown in figure 3.2. Data in following sections of this chapter are taken from [1] if not stated otherwise.

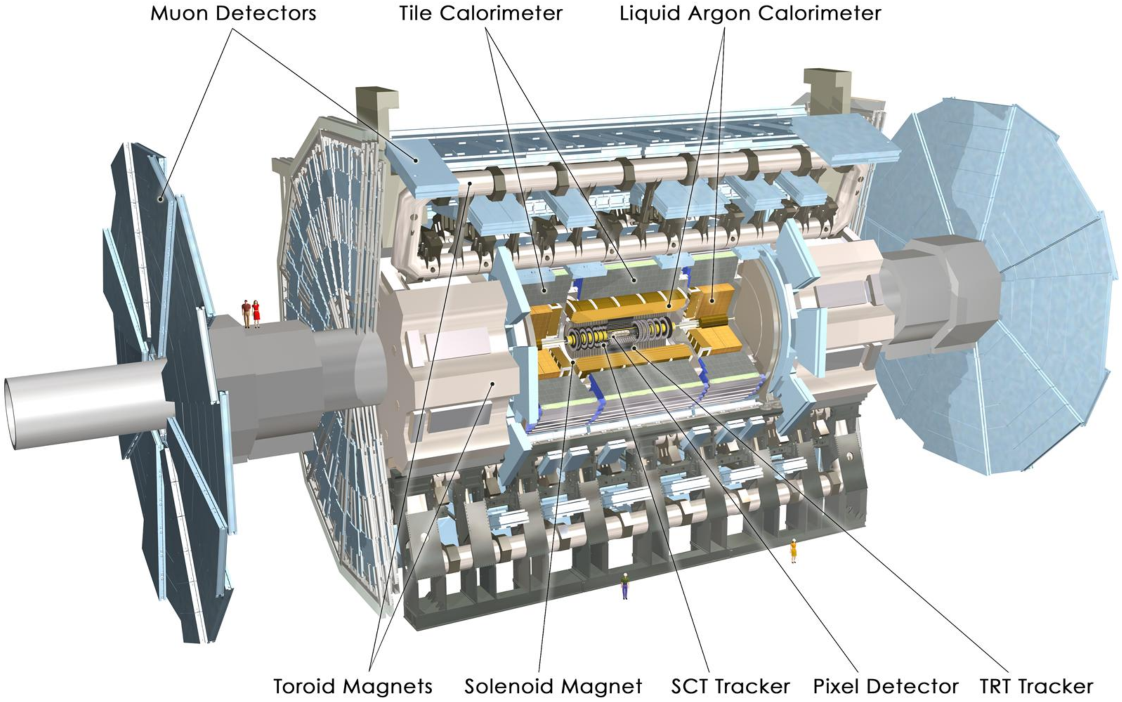

Figure 3.2: Schematic view of the ATLAS detector. Taken from [38].

3.2.1 Coordinate System

Throughout this thesis, the standard ATLAS coordinate system is employed. It is a right-handed system with the x-axis pointing to the centre of the LHC ring, the z-axis following the beam direction and the y-axis going upwards. In Point 1 (ATLAS), positive z points towards Point 8 (LHCb).

The azimuthal angle $\phi = 0$ corresponds to the positive x-axis and ϕ increases clock-wise looking into the positive z direction. ϕ is measured in the range $\langle -\pi, +\pi)$. The polar angle θ is measured from the positive z axis. Pseudorapidity η is defined by

$$\eta = -\ln\left(\tan\frac{\theta}{2}\right). \tag{3.2}$$

Transverse momentum $p_\mathrm{T} = p \cdot \sin\theta$ is the momentum perpendicular to the LHC beam axis. Transverse impact parameter d_0 is defined as the distance of the closest approach of helix to beampipe and longitudinal impact parameter z_0 as the z value at the point of closest approach.

3.2.2 Inner Detector

Precise tracking of the particles and vertex measurements in ATLAS are provided by the Inner Detector (ID), which combines high-resolution detectors at the inner part with continuous straws of transition radiation detector at the outer part. The ID is contained within a cylindrical envelope of length 7.02 m and of radius 1.15 m, inserted into the central 2 T solenoid (see section 3.2.5). It measures tracks and momenta of charged particles in the pseudorapidity range of $|\eta| < 2.5$. As shown in figure 3.3, the ID consists of three subsystems: a silicon pixel detector, a silicon microstrip detector and a transition radiation tracker. The ID is placed as close to the interaction point as possible (see figure 3.4). The environment there is demanding due to the high particle fluxes which inflict intense radiation damage degradation to ID components.

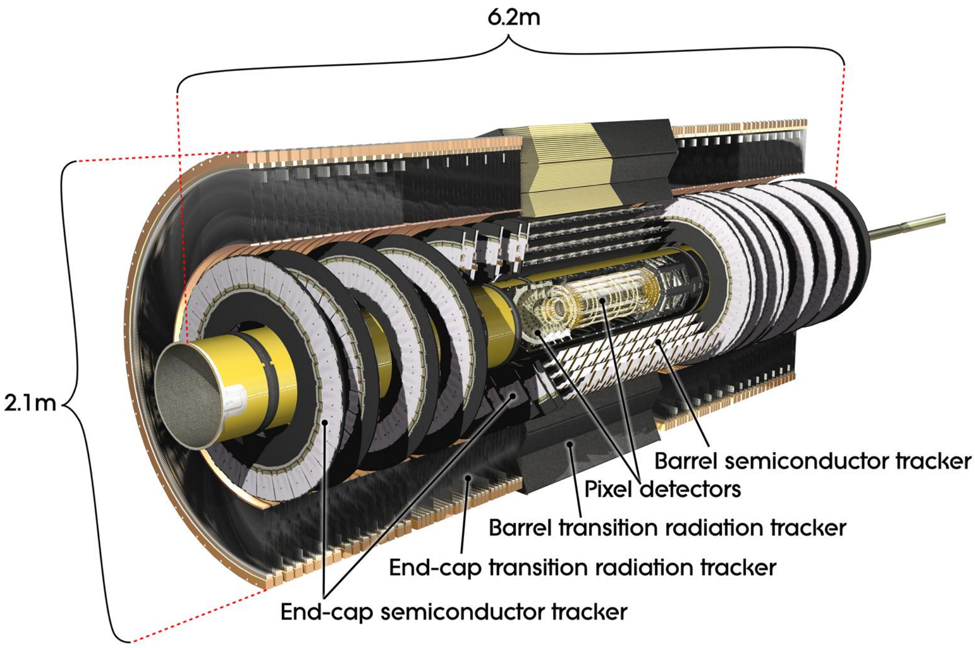

Figure 3.3: The schematic view of the ATLAS Inner Detector, with all disks and barrel layers. IBL is not shown in this figure. Taken from [39].

The **Pixel detector** is the innermost part of the ID. It provides a very high-granularity, high-precision set of measurements as close to the interaction point as possible, and thus it has the ability to find short-lived particles such as B-mesons. The detector consists of three barrels and three disks in each end-cap. The barrel layers are made of identical staves inclined with azimuthal angle of 20° and each stave is composed of 13 pixel modules. One end-cap disk is made of 8 sectors, with 6 modules in each sector (disk modules are identical to the barrel modules, except

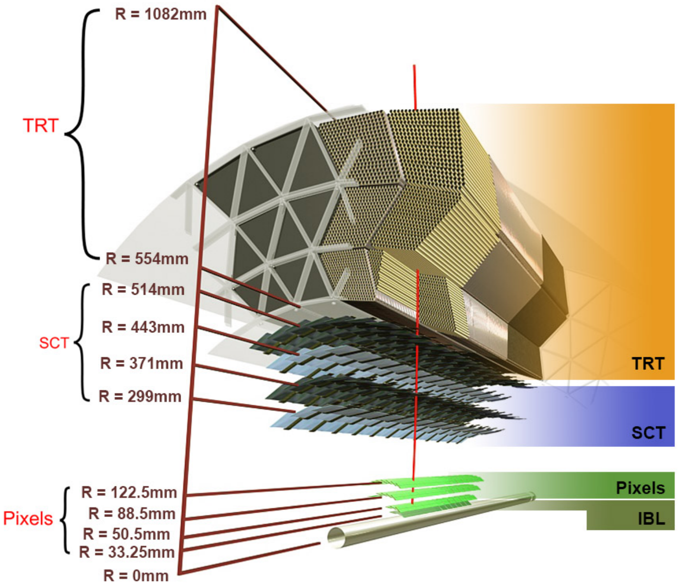

Figure 3.4: 3D visualization of the structure of the barrel of the ID, including the beam pipe and the IBL. Taken from [40].

the connecting cables). Altogether there are 1744 pixel modules with more than 80 million detection channels (pixels). The intrinsic resolution is 10 μm in the $R-\phi$ plane and 115 μm in z (barrel) or R (end-caps).

During the LHC Long Shutdown 1 (LS1), a new Insertable B-Layer (IBL) was added to the present ID[4]. It is the fourth layer with a radius 33.25 mm, inserted between a new beam pipe and the current inner pixel layer (B-layer), containing 280 pixel modules with the intrinsic resolution 8 μm × 40 μm.

The **SemiConductor Tracker** (SCT) is the second part of the ID. It is also a silicon detector, but instead of pixels it uses the silicon strips for detection. The SCT consists of 4088 modules with approximately 6.3 million readout channels, arranged in four barrel layers and two end-caps with nine wheels each. Eight silicon strip layers are grouped into pairs with small angle (40 mrad) stereo strips to measure both coordinates. The intrinsic resolution is 17 μm in $R-\phi$ plane and 580 μm in z (R) (arises from the 40 mrad stereo angle between back-to-back sensors on the modules).

The **Transition Radiation Tracker** (TRT) is the last part of the ID, covering the pseudorapidity range up to $|\eta| < 2.0$. The design is based on the use of straw detectors, which can operate at high rates due to their small diameter. This system detects the transition radiation photons which are created by passing particles. The

---

[4] Analysis presented in this thesis is based on ATLAS data from Run1 only, i.e. before the IBL was inserted into the ID.

barrel contains about 50000 straws, each divided in two at the center, and the end-caps contain 320000 radial straws. Each straw is 4 mm in diameter and equipped with a 30 μm diameter gold-plated tungsten wire. The TRT only provides $R - \phi$ information, for which it has an intrinsic accuracy of 130 μm per straw. In the barrel region, the straws are parallel to the beam axis and in the end-cap region, they are arranged radially in wheels.

Subdetector	Element Size	Intrinsic Resolution
IBL	50 μm × 250 μm	8 μm × 40 μm
Pixel	50 μm × 400 μm	10 μm × 115 μm
SCT	80 μm	17 μm × 580 μm
TRT	4 mm	130 μm

Table 3.1: Summary of the main characteristics of the ID subdetectors. The intrinsic resolution of the IBL, Pixel, and SCT is reported along $R - \phi$ and z, while for TRT is only along $R - \phi$. The z-resolution of SCT arises from the 40 mrad stereo angle between back-to-back sensors on the SCT modules. For SCT and TRT the element sizes refers to the spacing of the readout strips and the diameter of the straw tubes, respectively. Data for the IBL taken from [40].

3.2.3 Calorimetry System

Calorimeters measure the energy of charged and neutral particles (including photons) and jets. The ATLAS detector uses both an electromagnetic calorimeter and a hadronic calorimeter, covering a pseudorapidity $|\eta| < 4.9$.

The calorimeters closest to the beam-line use liquid argon (LAr) as the active detector medium. They are divided into a barrel part and two end-caps. The barrel part contains an electromagnetic (EM) calorimeter with lead absorber plates. It is divided into two identical half-barrels, separated by a small gap (6 mm) at $z = 0$. The two end-cap parts contain an electromagnetic end-cap calorimeter (EMEC) with lead absorbers, a hadronic end-cap calorimeter (HEC) with copper absorbers, and a forward calorimeter (FCal) with copper-tungsten absorbers. FCal covers the region closest to the beam. The total thickness of LAr calorimeters is at least 22 radiation lengths (X_0) in the barrel and at least $24X_0$ in the end-caps.

The barrel part of the hadronic calorimeter is a tile calorimeter (TileCal) with steel absorbers and scintillator tiles as active material. It is made up of a barrel and two extended barrel sections, together covering a pseudorapidity $|\eta| < 1.7$. The radial depth of the TileCal is approximately 7.4 λ (interaction lengths). The total thickness of the detector (including EM calorimeter) is at least 8.4 λ. A schematic view and locations of all ATLAS calorimetry systems are shown in figure 3.5.

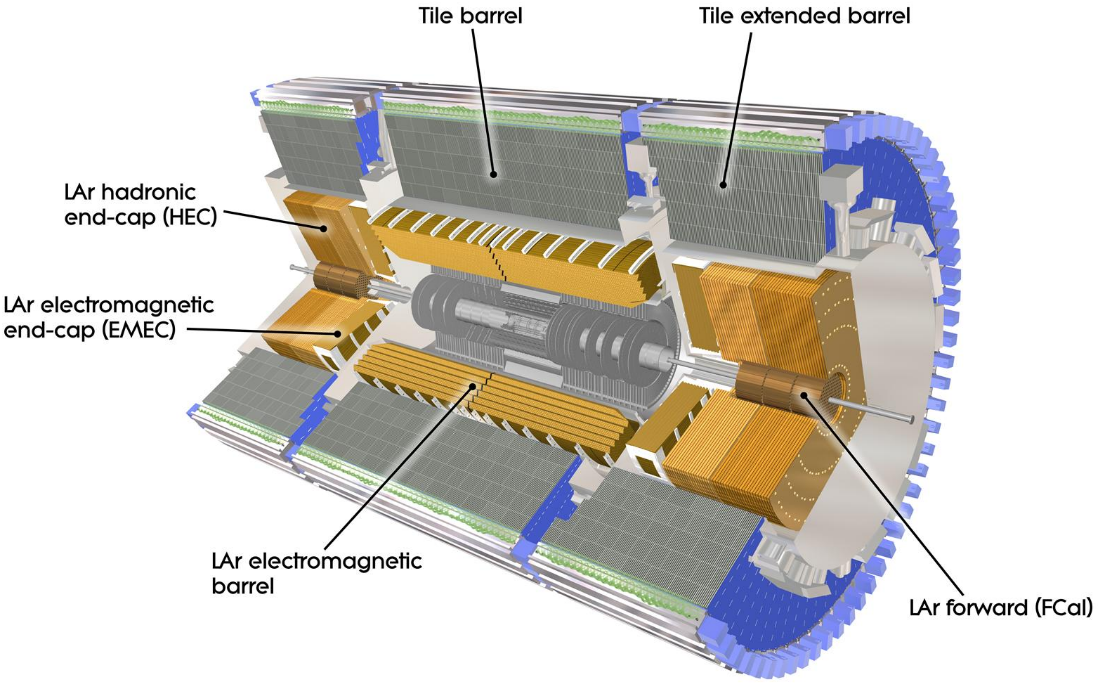

Figure 3.5: Schematic view of the ATLAS calorimetry system. Taken from [41].

3.2.4 Muon Spectrometer

Virtually only charged particles that can travel through all of the calorimeter material placed around the ID are muons. They lose energy almost entirely by the formation of electron-ion pairs along their path, and for a substance like steel, this amounts to an energy loss of about 1.57 MeV per millimetre of path. Thus muons with energy above 5 GeV will penetrate about 7.8 m of steel, whereas hadrons of almost any energy are completely absorbed in about 2 m of steel.

The Muon Spectrometer (MS) forms the outer part of the ATLAS detector, covering the pseudorapidity range $|\eta| < 2.7$. It is also designed to trigger in the region of $|\eta| < 2.4$. The MS provides momentum measurement for particles in a wide range of momenta, ranging from about a few GeV($\sim$ 3 GeV, due to energy loss in the calorimeters) up to approximately 3 TeV.

The MS consists of separate muon chambers high precision tracking and for triggering. The precision measurement is realized by Monitored Drift Tube chambers (MDT's) in the barrel region with resolution in z coordinate of about 35 μm per chamber, or about 80 μm per tube. In the end-caps Cathode-Strip Chambers (CSC's) are used. CSC's are multiwire proportional chambers with cathodes segmented into strips providing resolution of about 40 μm in the bending plane and about 5 mm in the transverse plane. For triggering Resistive Plate Chambers (RPC's) are used in the barrel and Thin Gap Chambers (TGC's) in the end-cap regions. Both chamber types deliver signals with a spread of 15-25 ns, thus providing the ability to tag the beam-crossing.

The chambers in the barrel are arranged in three concentric cylindrical shells around the beam axis at radii of approximately 5 m, 7.5 m, and 10 m. In the two end-cap regions, muon chambers form large wheels, perpendicular to the z-axis and located at distances of $|z| \approx 7.4$ m, 10.8 m, 14 m, and 21.5 m from the interaction point, as shown in figure 3.6.

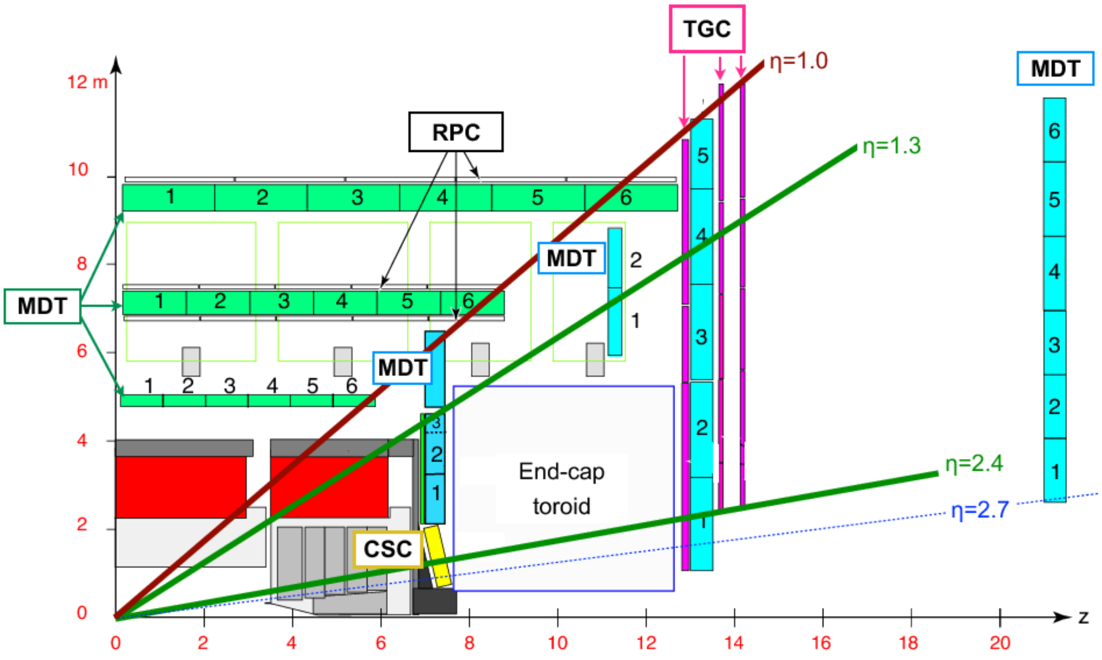

Figure 3.6: A schematic picture showing a quarter-section of the muon system in a plane containing the beam axis. Taken from [42].

3.2.5 Magnet System

To bend tracks and thus measure momentum of charged particles, ATLAS features a unique hybrid system of four large superconducting magnets: one central solenoid and three air-core toroids (see figure 3.7).

The central 2 T solenoid lies between the ID and the electromagnetic calorimeter and bends trajectories in the xy plane. The inner and outer diameters of the solenoid are 2.46 m and 2.56 m and its axial length is 5.8 m. The cold mass is 5.4 tonnes, the stored energy is 40 MJ, and the nominal current is 7.73 kA. To achieve the desired calorimeter performance, the layout was carefully optimized to keep the material thickness in front of the calorimeter as low as possible.

Barrel and two end-cap toroids generate the magnetic field for the MS. The two end-cap toroids are inserted in the barrel toroid at each end and line up with the central solenoid. Each subsystem consist of eight coils, but the end-cap toroids are rotated by 22.5° with respect to the barrel toroid. The nominal current of the system is 20.5 kA, providing a peak field of 3.9 T in barrel and 4.1 T end-cap sections. The overall size of the barrel toroid is 25.3 m in length, with inner and outer diameters of 9.4 m and 20.1 m, respectively. The cold mass is 370 tonnes and the stored energy is 1.08 GJ. Each end-cap toroid has length of 5 m and inner and outer diameters are 1.65 m and 10.7 m, respectively. The cold mass of each end-cap is 140 tonnes and the stored energy is 0.25 GJ.

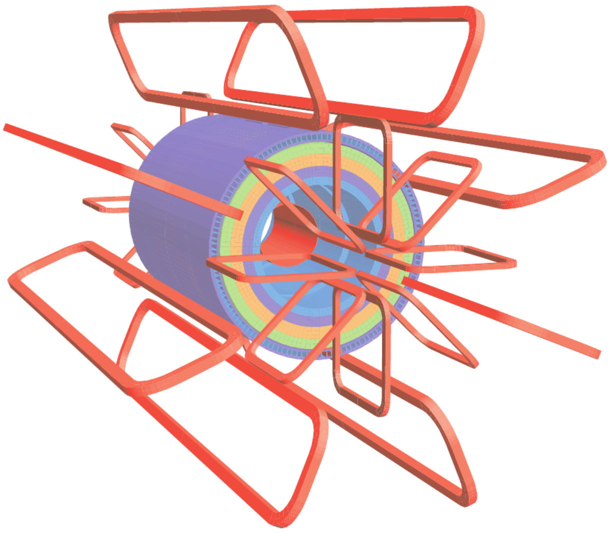

Figure 3.7: Geometry of magnet windings (red) and tile calorimeter steel (blue, purple, yellow, green). Taken from [1].

3.2.6 Trigger System

With the bunch separation of 25 ns, the pp interaction rate at the design luminosity is approximately 1 GHz. Technology and resource limitations allow the event data recording about 200 Hz. This requires an overall rejection factor of 5×10^6 against minimum-bias processes while maintaining maximum efficiency for the new physics.

The trigger system used in Run1 has a three level structure, as shown in figure 3.8. The first step, *Level 1* (L1) trigger, is implemented as a hardware trigger, the second and third steps, *Level 2* (L2) trigger and *Event Filter* (EF), are software triggers and are usually referred to as the ATLAS *High Level Trigger* (HLT).

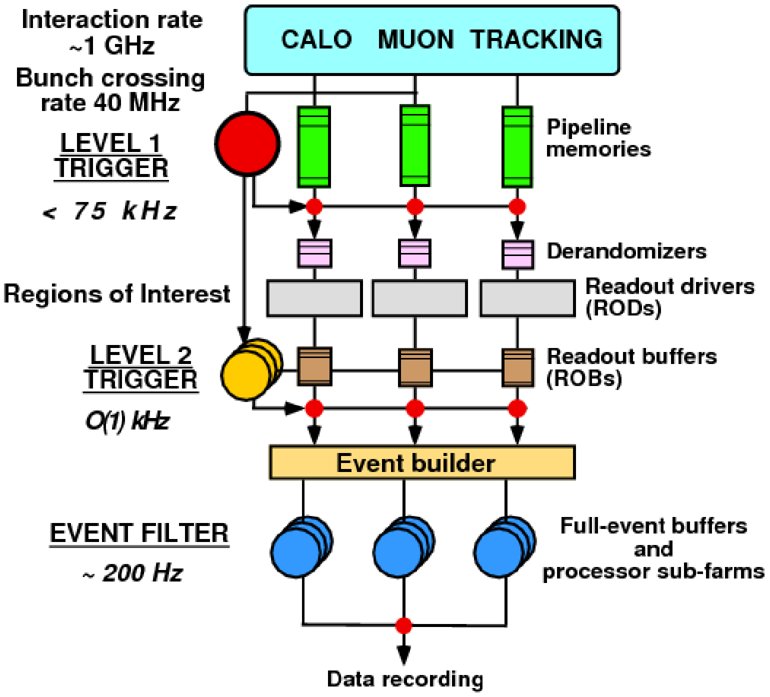

Figure 3.8: Schematic view of the ATLAS trigger system. Taken from [43].

L1 trigger reduces the initial 40 MHz to less than 75 kHz in less than 2.5 μs. It looks for regions of potentially interesting activity in the calorimeters and the MS that may correspond to candidates for high p_T leptons, hadrons, and jets, as well as large missing and total transverse energy. This is known as *Region of Interest* (RoI) concept. Each RoI contains information about the coordinates (η, ϕ) of interesting physics features combined with the selection criteria that were passed. Meanwhile the data are kept in pipeline memories.

The L2 selection is largely based on RoI information of the L1 trigger and uses fine-grained data from the full detector for a local analysis of the L1 candidate. The L2 trigger reduces the event rate to below 3.5 kHz, with an average event processing time of approximately 40 ms.

The Event Filter further reduces the rate to frequency of about 200 Hz, with an average event processing time of order four seconds. The RAW data of the full event are passed to the Event Builder, which collects the pieces of information connected to this event and put them into a single memory. The size of each event saved at the permanent data storage is about 1.5 MB.

The HLT menu contains more than 700 different algorithms and configurations (called L1-L2-EF trigger chains). Since the data storage rate is limited, the total bandwidth is divided into the various ATLAS physics groups. The trigger chains are constantly monitored and adapted to the increasing luminosity during data-taking. In some cases it is necessary to apply so-called prescaling, which means that only every n-th positive decision is taken into account, others are ignored as if the particular chains was not running at all.

3.2.7 B-physics Triggers

The $b\bar{b}$ events are of relatively low-p_{T} scale compared to the ATLAS sub-detectors genuine thresholds and to other processes studied in ATLAS. That means the calorimetry information would be dominated by background. ATLAS B-physics triggers are thus based mostly on processes with muons in the final states. The most common signatures are listed below:

Single-muon or two-muons triggers with various p_{T} thresholds. These events have high rate and they need to be prescaled. They are mostly used for control, calibration, and efficiency measurements.

Di-muon vertex triggers (topological di-muon triggers) are the main ATLAS B-physics triggers. They require two muons originating from the common vertex and thus eliminate much of the background.

Multi-muon vertex triggers are used for b-quarks correlations studies (μ+J/ψ) and multi-J/ψ events.

Triggers using $B \rightarrow \mu^+\mu^- X$ are used for semileptonic rare B-hadron decays $B \rightarrow \mu^+\mu^- X$ or for events where the di-muon vertex is combined with particles like K^{*0} or ϕ.

The basic algorithm for the nominal LHC luminosity is a topological di-muon trigger. It requires two muon RoI at L1, confirmed by the MS precision chambers at L2. At this stage, tracks are reconstructed in the MS using *muFast* algorithm and in the ID (within L1 RoIs) using *IDScan* or *L2StarB* (starting in 2012) algorithms. Then these collections are combined using *muComb* algorithm and passed onto the fast vertex fitter. If the vertex is of good quality and the di-muon invariant mass is in a preselected mass window, event is passed to EF. It repeats the L2 analysis, but using similar tools used in offline analysis for greater precision.

Each di-muon trigger exists in several configurations, based on the p_T threshold of the muon tracks connected with the L1 decision (`EF_mu4mu6` denotes two muon triggers at L1, confirmed at the HLT, with one muon passing a threshold of 4 and the other 6 GeV). The additional configuration is the di-muon invariant mass window:

- (2.5 - 4.3) GeV, denoted `_Jpsimumu`, used for triggering J/ψ events,
- (4.0 - 8.5) GeV, denoted `_Bmumu`, for rare $B^0_{d,s} \to \mu^+\mu^-$ decays,
- (8.0 - 12.0) GeV, denoted `_Upsimumu`, for Υ events,
- (1.5 - 14.0) GeV, denoted `_DiMu`, is a wider mass window covering all regions listed above; it is used, e.g., for non-resonant semileptonic rare B-decays $B \to \mu^+\mu^- X$.

The di-muon invariant mass windows for B-physics triggers in 2011 data are shown in figure 3.9.

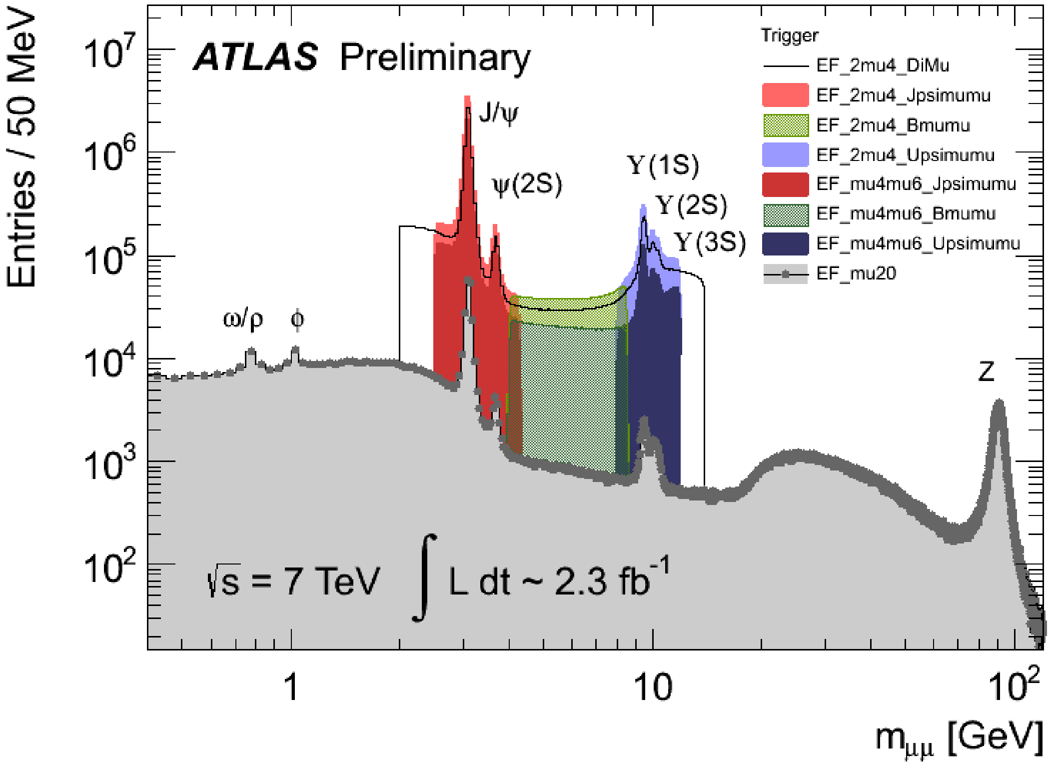

Figure 3.9: Invariant mass of oppositely charged muon candidate pairs selected by a variety of triggers. Different colours denote different di-muon invariant mass window. Naming convention is described in the text. If an event fires several triggers it appears in several samples, thus different trigger samples can overlap. Taken from [45].

3.2.8 The ATLAS Offline Software

Analysis presented in this thesis was performed using a set of common ATLAS software tools and High Energy Physics (HEP) libraries.

Athena [46] is the ATLAS common analysis framework. It manages almost all ATLAS production workflows: event generation, simulation, reconstruction, and derivation production. Athena is also used online in the ATLAS HLT (see section 3.2.6). The framework is based on C++ and Python and it is an enhanced version of the *Gaudi* framework that was originally developed by the LHCb experiment, but now it is a common ATLAS-LHCb project. Athena and Gaudi are concrete realizations of a component-based architecture (also called Gaudi) designed for a wide range of physics data-processing applications. All Athena packages can be managed using the Configuration Management Tool (CMT). There are common packages containing tools for, e.g., tracking and vertexing or detector geometry, managed and developed by tracking/software groups, but also group-specific packages, e.g., `JpsiFinder` or `Bd2JpsiKstar`, which are used for B-decays and are developed by the B-physics group.

ROOT [47] is an object-oriented framework written in C++. Both frameworks, ROOT and Athena, are well connected, but in general, they are absolutely independent. ROOT provides all the functionalities needed to deal with big data processing, statistical analysis, visualization and storage, and is very popular in the HEP community.

RooFit [48] is a library providing a toolkit for modelling the expected distribution of events in a physics analysis, originally developed for the BaBar[5] collaboration. Models can be used to perform unbinned maximum likelihood fits, and/or generate "toy" Monte Carlo (ToyMC)[6] samples for various studies. The natural modelling language are *Probability Density Functions* (PDFs). The RooFit library contains basic PDFs, such as Gaussian or Landau distributions, but also functions specific for the B-physics. PDFs can be easily joined together, allowing construction of higher dimensional PDFs out of lower dimensional building block. Users can also easily write their own PDFs. The RooFit library is part of the standard ROOT distribution.

---

[5] BaBar is the B-physics experiment at the PEP-II collider at the SLAC National Accelerator Laboratory, see `http://www-public.slac.stanford.edu/babar/`.

[6] In this thesis, (general) Monte Carlo (MC) refers to the fully generated physics data, which can be then used for the simulation of the detector "output". ToyMC refers to the generation of the final data distribution, based on the given model.

Following packages are used within the Athena framework to generate physics events and simulate the response of the detector.

Pythia [49] and Herwig [50] are physics event generators commonly used in ALTAS to simulate the initial partonic collision described by perturbative QCD. Older versions of the packages, written in Fortran 77, are now superseded by the C++ based versions.

PythiaB [51] provides an interface to Pythia, allowing to speed up B-physics events simulations and also simulate only wanted decay channel, while leaving all other B-hadrons in the event to decay freely. Due to the large amount of background processes in the pp collisions, the fraction of $b\bar{b}$ pairs is only $\sim 1\%$ and even smaller fraction become B_s^0 mesons. It is possible to change the branching ratios in Pythia to boost the production of B_s^0 mesons, but this would have large side effects on the resulting cross-section and p_{T} spectra. To avoid this the *repeated hadronization* method is used. PythiaB clones the Pythia generated parton-level event n-times (defined by user) and hadronizes each one as if an independent event. To not bias the generated sample, the control algorithm checks if the average number of events passing the final-state filtering is close to unity.

EvtGen [52] is an external package dedicated to decays of B-hadrons written initially by BaBar. ATLAS use a version adopted for the LHC. EvtGen uses spin algebra and complex amplitudes to describe decays, allow interference effects, CP-violation due interference between mixing and decay and other B-physics phenomena. The EvtGen is just a “decayer”, not a generator, and thus it needs to be run after Pythia (or similar tool).

Geant4 [53] is a toolkit for the simulation of the passage of particles through matter and magnetic fields, creating new events from interactions with the materials and for simulating the reactions of active detector components to the particles. Besides HEP, its areas of application include nuclear physics in general, as well as studies in medical and space science.

3.2.9 ATLAS Data Reconstruction Flow

The ATLAS offline analysis starts when the event is passed by the EF (section 3.2.6) and saved to the data storage. At each reconstruction step the different data type is used, containing specific information – at the final step, only physics objects are delivered to end-users:

RAW data are complete events coming from the EF. These data contain all information from the detector in a compressed byte-stream format. Typical event size is 1-2 MB and events are arriving at rate of 200 Hz.

ESD (**E**vent **S**ummary **D**ata) are produced from the RAW data and contains also the detailed output of the detector physics object reconstruction.

AOD (**A**nalysis **O**bject **D**ata) is a reduced event representation, derived from ESD, suitable for analysis. It contains physics objects, but no detector hits. Typical event size is 100-200 kB.

DAOD (**D**erived **A**nalysis **O**bject **D**ata) are derived from AODs using a reduction of unnecessary events and data stores. They can also have additional object stores not written in a standard AOD.

DPD (**D**erived **P**hysics **D**ata), sometimes referred simply as **ntuples**, are ROOT n-tuple-style representation of event data for end-user analysis.

Chapter 4

Data Selection

Study of the $B_s^0 \to J/\psi(\mu^+\mu^-)\phi(K^+K^-)$ decay channel is a CP-violation evergreen. At the beginning of the LHC operation, there was large room for improvement. Author of this thesis has contributed to all three published ATLAS papers on this topic: untagged analysis of 7 TeV pp data from 2011 [7], tagged (improved) analysis of the same 7 TeV data [8], and tagged analysis of 8 TeV pp data from 2012, combined with the previous analysis into the final Run1[7] result [9]. Now, after successful Run1 and with ATLAS improvements from LS1, the measurement of the CP-violation in $B_s^0 \to J/\psi(\mu^+\mu^-)\phi(K^+K^-)$ decay is ongoing using the first part of Run2 13 TeV data.

4.1 Real Data

Data used in the analysis were collected in the years 2011 and 2012, during the Run1 pp campaign. The LHC stable beam flag is required to be set as well as the ID and the MS both operating correctly. Figure 4.1 shows the integrated luminosity delivered by the LHC and collected by the ATLAS experiment in Run1.

Triggers used to select events were searching for either a $J/\psi \to \mu^+\mu^-$ signature or a single high-p_{T} muon, both with various muon(s) p_{T} threshold. Triggers are summarized in table 4.1, together with the overview of used data.

---

[7] ATLAS data are collected in *runs* (usually the entire LHC fill) and they are subdivided into *lumiblocks* approximately 1 minute long. In this period of time, data conditions (detector status, trigger settings) should be the same. Similar runs are then grouped into *periods*. Data-taking before LS1 is called Run1, similarly data taken between LS1 and LS2 are called Run2 etc.

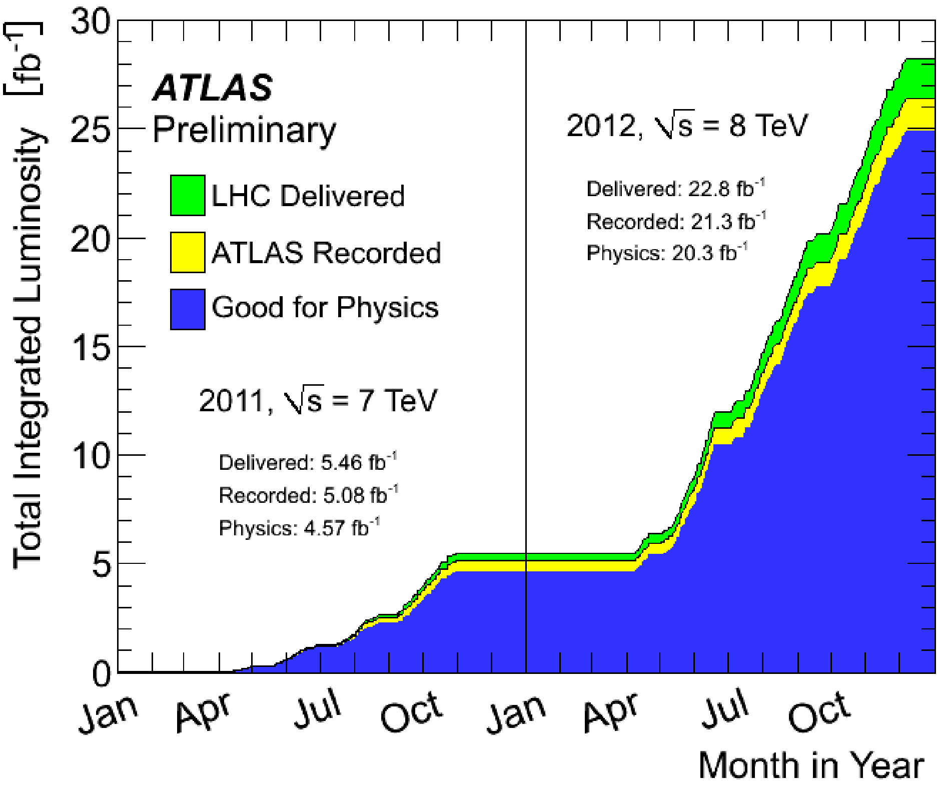

Figure 4.1: Cumulative luminosity versus time delivered to (green), recorded by ATLAS (yellow), and certified to be good quality data (blue) during stable beams and for *pp* collisions at 7 and 8 TeV centre-of-mass energy in 2011 and 2012. Taken from [54].

4.2 Monte Carlo

To determine detector effects, estimate backgrounds and model systematic effects, several Monte Carlo (MC) samples were simulated using Pythia 6 (for 7 TeV analysis) and Pythia 8 (for 8 TeV analysis):

- 12 millions $B_s^0 \to J/\psi(\mu^+\mu^-)\phi(K^+K^-)$ signal events with flat angular distributions, tuned with recent ATLAS data [55]. No p_{T} cuts were applied at the generator level. In order to take into account the varying number of *pp* interactions per bunch crossing (so-called "pile-up") and trigger configurations during data-taking, the MC events were weighted to reproduce the same pile-up and trigger conditions in data.

- 100 thousand $B_s^0 \to J/\psi(\mu^+\mu^-)\phi(K^+K^-)$ signal events with realistic angular distributions. This MC sample was used to determine effects of the ID misalignment, validation of the signal model in the fit, and for the determination of a bias induced by the muon triggers (see section 5.2.5).

Year	
2011	2012
Centre-of-Mass Energy	
7 TeV	8 TeV
Integrated Luminosity	
4.9 fb^{-1}	14.3 fb^{-1}
Data Periods	
B2, D, E, F2, F3, G, H, I, J, K1, K2, K3, K4, L, M2, M4, M5, M6, M8, M10	C6-C9, D, E, G, H, I, J, L
Triggers	
`EF_mu4_Jpsimumu`, `EF_mu6_Jpsimumu`, `EF_mu6_Jpsimumu_tight`, `EF_mu10_Jpsimumu`, `EF_2mu4_Jpsimumu`, `EF_2mu4T_Jpsimumu`, `EF_mu4mu6_Jpsimumu`, `EF_mu4Tmu6_Jpsimumu`, `EF_2mu4_DiMu`, `EF_mu4mu6_DiMu`, `EF_mu4Tmu6_DiMu`, `EF_2mu4_Bmumux`, `EF_2mu4T_Bmumux`, `EF_mu4mu6_Bmumux`, `EF_mu4Tmu6_Bmumux`, `EF_2mu6_Bmumux`	`EF_2mu4T_Jpsimumu_L2StarB`, `EF_2mu4T_Jpsimumu_Barrel_L2StarB`, `EF_2mu4T_Jpsimumu_BarrelOnly_L2StarB`, `EF_mu4Tmu6_Jpsimumu_L2StarB`, `EF_mu4Tmu6_Jpsimumu_Barrel_L2StarB`, `EF_2mu6_Jpsimumu_L2StarB`

Table 4.1: Summary of data used in the analysis, together with the trigger selection used. Data collected at the beginning of the 8 TeV data-taking period are not included in the analysis due to a problem with the trigger tracking algorithm. The trigger was subsequently changed to use a different algorithm that did not have this problem.

- $B_d^0 \to J/\psi K^{0*}$, $B_d^0 \to J/\psi K^{\pm}\pi^{\mp}$, $b\bar{b} \to J/\psi X$, and $pp \to J/\psi X$ samples to study the background contributions and to determine the fractions of mis-reconstructed $B_d^0 \to J/\psi(\mu^+\mu^-)K^{\pm}\pi^{\mp}$ (both resonant and non-resonant) events.

All simulated MC samples are shown in figure 4.2. Background samples are scaled relative to the signal sample using the branching fractions taken from [56]. $pp \to J/\psi X$ sample represents prompt J/ψ (i.e. J/ψ produced directly in the pp collision) combined with two random tracks from the same primary vertex (PV). These B_s^0 candidates have effectively zero lifetime (see "prompt" peak in section 5.2.2). Specific backgrounds $B_d^0 \to J/\psi(\mu^+\mu^-)K^{0*}(K^{\pm}\pi^{\mp})$ and non-resonant $B_d^0 \to J/\psi(\mu^+\mu^-)K^{\pm}\pi^{\mp}$ are used to study events, where the $K^{\pm}$ mass was wrongly assigned to a final state $\pi^{\pm}$, forming a candidate in a good mass range, but with shifted mass and lifetime.

Background sample containing $b\bar{b} \to J/\psi X$ are all b-hadron decays into J/ψ and two tracks (apart from the signal and background described above). These event have non-zero lifetime.

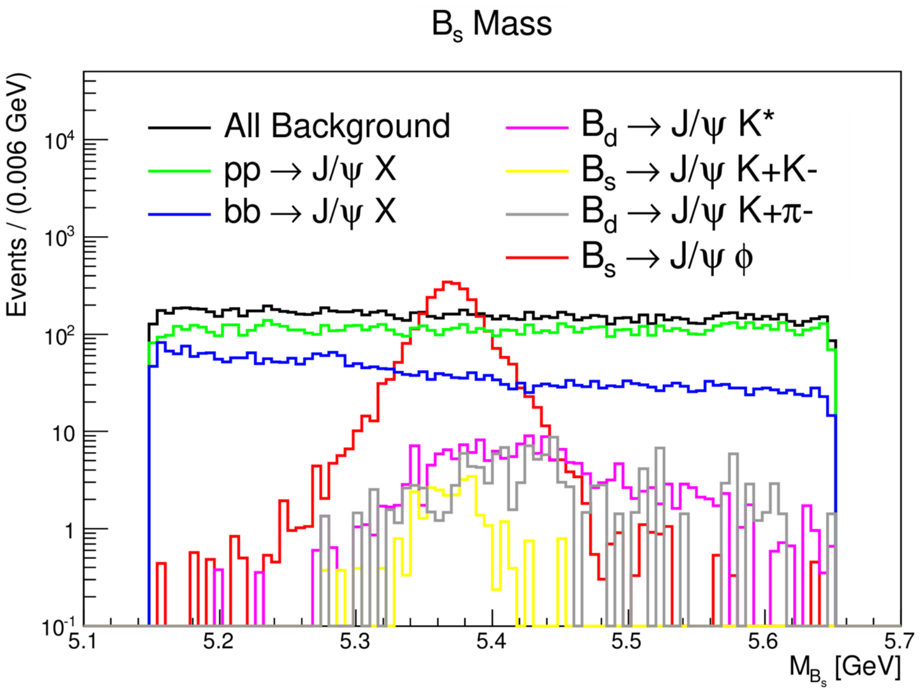

Figure 4.2: Plot of the mass of the B_s^0 candidates reconstructed from signal and background MC samples. The background contributions are scaled relative to the signal using the branching fractions taken from [56].

4.3 Candidate Selection and Reconstruction

After passing the trigger and the data quality selections, event has to fulfil following criteria to be selected for further analysis.

- The event must contain at least one reconstructed primary vertex with at least four associated ID tracks.
- These tracks are required to have at least one hit in the Pixel detector and at least four hits in the SCT.
- The event must contain at least one pair of oppositely charged muon candidates. Only *combined*[8] and *segment-tagged*[9] muons are allowed. No cuts on the

---

[8] *Combined muons* are found by matching a MS track to nearby ID tracks and then combining the measurements from the two systems.

[9] *Segment-tagged muons* are found by extrapolating ID tracks to the MS and searching for nearby hits.

p_{T} of the muons are applied.

Although both the ID and the MS are used for muon identification, the muon track parameters are determined from the ID measurement alone, because the precision of the measured track parameters for muons in the low-p_{T} region is dominated by the ID track reconstruction. Muon pair tracks are then refitted to a common vertex and the pair is accepted if the quality of the fit is $\chi^2/\mathrm{d.o.f.} < 10$. The invariant mass of the di-muon (J/ψ) candidate is then calculated from the refitted track parameters.

Since the mass resolution varies in the different part of the detector, three J/ψ signal regions are defined according to the pseudo-rapidity of the muons:

- If both muons have $|\eta| < 1.05$ (both muons in the barrel region), the J/ψ signal region is defined as (2.959 - 3.229) GeV.
- If one muon has $|\eta| < 1.05$ and the other muon $1.05 < |\eta| < 2.5$ (the end-cap region), the corresponding signal region is (2.913 - 3.273) GeV.
- If both muons have $1.05 < |\eta| < 2.5$, the signal region is (2.852 - 3.332) GeV.

The signal region in each case is obtained as the range containing 99.8 % of the J/ψ candidates identified in the maximum-likelihood fit to the di-muon invariant mass.

Candidates for the $\phi \to K^+K^-$ are reconstructed from all pairs of oppositely charged particles with $p_{\mathrm{T}} > 1$ GeV and $|\eta| < 2.5$ that are not identified as muons. Each combination of J/ψ and ϕ candidates are then fitted to a common vertex, using a mass constraint for the di-muon invariant mass to the World average J/ψ mass [57]. A quadruplet of tracks is accepted if the following criteria are fulfilled:

- The vertex fit has a $\chi^2/\mathrm{d.o.f.} < 3$.
- Fitted p_{T} of each hadron track is $p_{\mathrm{T}} > 1$ GeV.
- The invariant mass of the hadron track pairs (assuming a kaon hypothesis) is $1.0085\ \mathrm{GeV} < m(K^+K^-) < 1.0305\ \mathrm{GeV}$.
- B_s^0 candidate invariant mass falls within the range (5.15 - 5.65) GeV.

If there is more than one accepted B_s^0 candidate in the event, the one with the lowest $\chi^2/\mathrm{d.o.f.}$ is selected.

For each B_s^0 candidate the proper decay time t is calculated as follows

$$t = \frac{L_{xy}\, m_{\mathrm{PDG}}(B_s^0)}{p_{\mathrm{T}}(B_s^0)}, \tag{4.1}$$

where $m_{\mathrm{PDG}}(B_s^0)$ is the mass of the B_s^0 meson taken from [57], $p_{\mathrm{T}}(B_s^0)$ is the reconstructed transverse momentum of the B_s^0 candidate, and L_{xy} is the transverse distance of the B_s^0 decay vertex from the primary interaction vertex. Used primary vertex is refitted following the removal of the tracks used to construct the B_s^0 candidate. For each proper decay time an associated uncertainty is calculated using the covariance matrix of the tracks quadruplet vertex fit.

Due to the high luminosity at the LHC there are more primary vertices in each event ($\sim$ 6 PV/event in 2011 data and $\sim$ 12 PV/event in 2012 data, see table 4.2 for details). Thus it is necessary to choose the correct primary vertex to calculate the B_s^0 lifetime. At the beginning of the data-taking, the primary vertex with the highest $\sum p_{\mathrm{T}}^2$ of the constituent tracks in the event was used. However, with the increasing pile-up, the method of the best impact parameter a_0 was chosen (the primary vertex with smallest 3D distance to the B_s^0 momentum vector is used). A study [58] has shown that these two methods overlap in 97 % of 2011 data and (using a MC sample) that the smallest a_0 method choose the correct primary vertex in more than 99 % of events.

A fit stability was tested through the 2011 and 2012 data periods as the luminosity was increasing. An unbinned simultaneous mass-lifetime maximum likelihood fit[10] with per-candidate errors was performed for each period separately, as well as for all data in given year. A simple-lifetime signal model was used. A summary of the fit results is shown in table 4.2. It is clear that the mass and lifetime determination is stable over all periods, except the period B of 2012, which was then found to have a problem with the trigger tracking algorithm and thus excluded from the analysis.

---

[10] Principles of the unbinned maximum likelihood fitting are described in section 5.1.

2011					
Period	$\mathscr{L}_{\text{Int}}$ [pb^{-1}]	#PV/ev.	Sig./pb^{-1}	m [MeV]	τ [ps]
B - F	401	4.6	6.7	5366.4 ± 0.5	1.43 ± 0.03
G	558	4.6	6.2	5367.7 ± 0.5	1.50 ± 0.03
H	278	4.1	6.2	5367.4 ± 0.7	1.44 ± 0.04
I - J	634	4.8	5.8	5366.9 ± 0.5	1.42 ± 0.03
K	595	5.3	5.1	5367.4 ± 0.6	1.48 ± 0.03
L	1438	7.3	4.4	5367.7 ± 0.4	1.45 ± 0.02
M	1036	7.9	4.7	5367.6 ± 0.4	1.45 ± 0.03
Total	4940	6.0	5.2	5367.4 ± 0.2	1.45 ± 0.01

2012					
Period	$\mathscr{L}_{\text{Int}}$ [pb^{-1}]	#PV/ev.	Sig./pb^{-1}	m [MeV]	τ [ps]
B	5057	11.0	4.1	5367.0 ± 0.2	1.39 ± 0.01
C	1400	10.6	5.2	5366.5 ± 0.4	1.43 ± 0.02
D	3283	11.2	5.2	5367.1 ± 0.2	1.48 ± 0.01
E	2531	11.9	5.2	5367.4 ± 0.3	1.47 ± 0.02
G	1280	11.9	5.3	5366.9 ± 0.4	1.46 ± 0.02
H	1455	12.2	4.9	5366.9 ± 0.4	1.49 ± 0.02
I	1025	12.7	5.1	5367.3 ± 0.4	1.49 ± 0.02
J	2617	12.1	5.1	5367.0 ± 0.3	1.48 ± 0.02
L	849	12.2	5.1	5367.4 ± 0.5	1.50 ± 0.03
Total	19497	11.6	4.8	5367.1 ± 0.1	1.459 ± 0.006

Table 4.2: A summary of the fit stability tests through the 2011 and 2012 data periods. $\mathscr{L}_{\text{Int}}$ is an integrated luminosity, #PV/ev. is an average number of PVs in the events, and Sig./pb^{-1} stands for the signal yield. An unbinned simultaneous mass-lifetime maximum likelihood fit with per-candidate errors was performed for each period separately, as well as for all data in given year. A simple-lifetime signal model was used. It is clear that the mass and lifetime determination is stable over all periods, except the 2012 period B, which was then excluded from the analysis due to a problem with the trigger tracking algorithm.

Chapter 5

Fitting Procedure

To obtain physical parameters describing the CP-violation in the $B_s^0 \to J/\psi\phi$ decay, the observed data have to be statistically processed. The relevant models that describe the expected distributions of the observable quantities must be formulated. Then, model parameters that describe the data most likely have to be found. A standard technique is to use *maximum likelihood estimators*, because they are unbiased and efficient asymptotically, under quite general conditions.

In this chapter, first the unbinned maximum likelihood fitting method is briefly described (following formalism in [18]). Next, the detailed description of all constituent models of the main fit used for $B_s^0 \to J/\psi\phi$ data is given. In the last section, the treatment of a time-dependent bias caused by the muon triggers is discussed.

5.1 Unbinned Maximum Likelihood Method

For the observable quantities $\vec{x}$ and for a given set of physics parameters of interest $\vec{p}$, the models of observable distributions are described with a Probability Density Function (PDF)

$$\mathcal{P}(\vec{x};\vec{p}), \tag{5.1}$$

which is positive definite, and normalized to unity over the allowed range of the observable $\vec{x}$ for any value of $\vec{p}$.

Realistic models also often incorporate a set of additional "nuisance parameters" $\vec{q}$ that represent quantities that affect the relation between $\vec{p}$ and $\vec{x}$ that are not a priori known and must be simultaneously inferred from the data. The model is thus defined as

$$\mathcal{P}(\vec{x};\vec{p},\vec{q}). \tag{5.2}$$

Likelihood is a function of the parameters $\vec{p}$ and $\vec{x}$ and it is defined as the PDF evaluated at the measured data point $\vec{x}_0$

$$\mathcal{L}(\vec{p}, \vec{q}) = \mathcal{P}(\vec{x}_0; \vec{p}, \vec{q}). \tag{5.3}$$

If measured data consist of *independent* and *identically distributed* values, i.e. a set of n statistically independent quantities $(\vec{x}_1, ..., \vec{x}_n)$, where each component follows the same PDF $\mathcal{P}(\vec{x}; \vec{p}, \vec{q})$, the joint PDF of the data sample factorizes and the (unbinned) likelihood function is simply the product of the likelihood of each observation

$$\mathcal{L}(\vec{p}, \vec{q}) = \prod_{i=0}^{n} \mathcal{P}(\vec{x}_i; \vec{p}, \vec{q}). \tag{5.4}$$

Usually, the negative log-likelihood is used, because it is numerically easier to calculate:

$$-\ln \mathcal{L}(\vec{p}, \vec{q}) = -\sum_{i=0}^{n} \ln \mathcal{P}(\vec{x}_i; \vec{p}, \vec{q}). \tag{5.5}$$

The maximum likelihood estimator $\widehat{p}$ for a parameter $\vec{p}$ is defined as the value of $\vec{p}$ for which the likelihood is maxinal (or equivalently, the negative log-likelihood is minimal).

The statistical uncertainty $\sigma(\widehat{p})$ of the parameter estimate $\widehat{p}$ can be calculated as the square-root of the variance $V(\widehat{p})$, which can be estimated as

$$\widehat{V}(p, p') = \left(\frac{\partial^2 \ln \mathcal{L}(p, p')}{\partial p \partial p'} \right)^{-1}_{p=\widehat{p}, p'=\widehat{p}'} \tag{5.6}$$

For completeness, *binned* negative log-likelihood is defined as

$$-\ln \mathcal{L}(\vec{p}, \vec{q}) = -\sum_{j=0}^{m} n_j \cdot \ln \mathcal{P}(\vec{x}_j; \vec{p}, \vec{q}), \tag{5.7}$$

where $\vec{x}_j$ and n_j represent the bin centre and event count of bin j of a histogram with m bins. A binned likelihood is a priori less precise, since for the same data sample it contains less data points.

5.2 Likelihood of the $B_s^0 \to J/\psi\phi$ Analysis

The simultaneous unbinned maximum likelihood fit to the B_s^0 candidates uses information about the reconstructed mass m, proper decay time t, mass and proper decay time uncertainties σ_m and σ_t, and three transversity angles $\Omega = (\theta_T, \psi_T, \phi_T)$, as defined in section 2.2.4. Likelihood function is composed of several PDFs:

$$\begin{aligned}\ln \mathcal{L} = \sum_{i=1}^{N} \Big\{ w_i \cdot \ln \Big(& f_{\text{sig}} \cdot \mathcal{F}_{\text{sig}}(m_i, t_i, \Omega_i) + f_{\text{sig}} \cdot f_{B_d^0} \cdot \mathcal{F}_{B_d^0}(m_i, t_i, \Omega_i) \\ & + (1 - f_{\text{sig}}(1 + f_{B_d^0})) \cdot \mathcal{F}_{\text{bck}}(m_i, t_i, \Omega_i) \Big) \Big\}, \end{aligned} \tag{5.8}$$

where N is the number of B_s^0 candidates, w_i is a weighting factor to account for the trigger efficiency (see section 5.2.5), f_{sig} is the signal fraction, and $f_{B_d^0}$ is the relative fraction of B_d^0 background (mentioned in section 4.2), which is fixed in the fit. PDFs $\mathcal{F}_{\text{sig}}(m_i, t_i, \Omega_i)$, $\mathcal{F}_{B_d^0}(m_i, t_i, \Omega_i)$, and $\mathcal{F}_{\text{bck}}(m_i, t_i, \Omega_i)$ are described in following sections. The mass m_i, the proper decay time t_i and angles Ω_i are observables measured from the data for each event i.

It should be noted, that the likelihood function defined in equation (5.8) is a general form used in the analysis. Additional terms have to be introduced for the tagged analysis of 7 TeV data (as described in chapter 7) and for the analysis of much larger sample of 8 TeV data (chapter 8).

5.2.1 Signal Model

The signal PDF $\mathcal{F}_{\text{sig}}$ is a product of PDFs for each observable:

$$\begin{aligned}\mathcal{F}_{\text{sig}}(m_i, t_i, \Omega_i) = & \mathcal{P}_{\text{sig}}(m_i|\sigma_{m_i}) \cdot \mathcal{P}_{\text{sig}}(\sigma_{m_i}) \cdot \mathcal{P}_{\text{sig}}(\Omega_i, t_i|\sigma_{t_i}) \\ & \cdot \mathcal{P}_{\text{sig}}(\sigma_{t_i}) \cdot \mathcal{A}_{\text{sig}}(\Omega_i, p_{\text{T}i}) \cdot \mathcal{P}_{\text{sig}}(p_{\text{T}i}). \end{aligned} \tag{5.9}$$

The signal mass model $\mathcal{P}_{\text{sig}}(m_i|\sigma_{m_i})$ is a single Gaussian function smeared with an event-by-event mass resolution σ_{m_i}, which is scaled using a single scale factor s_m to account for a general mis-estimation of the mass errors:

$$\mathcal{P}_{\text{sig}}(m_i|\sigma_{m_i}) = \frac{1}{\sqrt{2\pi}\,\sigma_{m_i} s_m} e^{-\left(\frac{m_i - M}{\sqrt{2}\,\sigma_{m_i} s_m}\right)^2}. \tag{5.10}$$

The PDF is normalized over the mass range (5.15 - 5.65) GeV.

Since the mass model $\mathcal{P}_{\text{sig}}(m_i|\sigma_{m_i})$ is in fact a conditional PDF (and not a simple PDF of two observables), it has to be multiplied by model $\mathcal{P}_{\text{sig}}(\sigma_{m_i})$ describing the distribution of the mass uncertainty σ_m, as proved in [59]. This kind of term has to be included in the likelihood for every conditional PDF, except the rare cases, where the signal and background distributions are the same – then these terms can be factorized out. Moreover, the mass uncertainty is highly correlated with p_{T} of the B_s^0 candidate (as shown in figure 5.1) and thus the term $\mathcal{P}_{\text{sig}}(\sigma_{m_i})$ has to be multiplied by a similar PDF for $p_{\mathrm{T}}(B_s^0)$, in equation (5.9) denoted as $\mathcal{P}_{\mathrm{sig}}(p_{\mathrm{T}i})$. All these PDFs are described in section 5.2.4.

The signal time-angular model $\mathcal{P}_{\mathrm{sig}}(\Omega_i, t_i|\sigma_{t_i})$ is derived from the differential decay rate given in equation (2.37). Because of the the limited detector resolution, each time dependent term in the differential decay rate has to be smeared with the uncertainty of the decay time σ_{t_i}. This is done on event-by-event basis by a numerical convolution of the time-dependent term with a Gaussian with a zero mean and a width given by the proper decay time uncertainty σ_{t_i}, multiplied by an overall scale factor s_t to account for any mis-measurements:

$$\mathcal{R}(t_i|\sigma_{t_i}) = \frac{1}{\sqrt{2\pi}\,\sigma_{t_i} s_t} e^{-\left(\frac{t_i}{\sqrt{2}\,\sigma_{t_i} s_t}\right)^2}. \tag{5.11}$$

This PDF has to be also multiplied by a model $\mathcal{P}_{\mathrm{sig}}(\sigma_{t_i})$ describing the distribution of the uncertainty and by the $\mathcal{P}_{\mathrm{sig}}(p_{\mathrm{T}i})$ model for the p_{T}-dependence.

The angular sculpting of the detector, the kinematic cuts on the angular distributions, and the trigger and reconstruction efficiencies are included in the likelihood function through the $\mathcal{A}_{\mathrm{sig}}(\Omega_i, p_{\mathrm{T}i})$ term. The model is represented by a 4D binned map of the transversity angles $(\theta_T, \psi_T, \phi_T)$ and the p_{T} of the B_s^0 candidates. The map is created using the 12 millions "flat" MC sample (see section 4.2). Generated MC data are passed through the detector simulation, trigger chains, offline reconstruction, and selection cuts and the resulting data are compared with the generated sample – the acceptance in each bin of the map is calculated as the number of remaining B_s^0 candidates over the number of generated B_s^0 mesons.

Since the acceptance $\mathcal{A}_{\mathrm{sig}}(\Omega_i, p_{\mathrm{T}i})$ and time-angular PDF $\mathcal{P}_{\mathrm{sig}}(\Omega_i, t_i|\sigma_{t_i})$ are multiplied in the likelihood function and since they both depend on the transversity angles, the complete angular function must be normalized as a whole. This normalization is performed numerically in the likelihood fit.

5.2.2 Background Model

The background component $\mathcal{F}_{\mathrm{bck}}$ is constructed similarly to the signal PDF:

$$\begin{aligned}\mathcal{F}_{\mathrm{bck}}(m_i, t_i, \Omega_i) = {} & \mathcal{P}_{\mathrm{bck}}(m_i) \cdot \mathcal{P}_{\mathrm{bck}}(\sigma_{m_i}) \cdot \mathcal{P}_{\mathrm{bck}}(t_i|\sigma_{t_i}) \cdot \mathcal{P}_{\mathrm{bck}}(\theta_T) \\ & \cdot \mathcal{P}_{\mathrm{bck}}(\psi_T) \cdot \mathcal{P}_{\mathrm{bck}}(\phi_T) \cdot \mathcal{P}_{\mathrm{bck}}(\sigma_{t_i}) \cdot \mathcal{P}_{\mathrm{bck}}(p_{\mathrm{T}i}).\end{aligned} \tag{5.12}$$

The background mass model $\mathcal{P}_{\mathrm{bck}}(m_i)$ is a linear function, normalized over the range (5.15 - 5.65) GeV.

The background proper decay time model $\mathcal{P}_{\mathrm{bck}}(t_i|\sigma_{t_i})$ is composed from

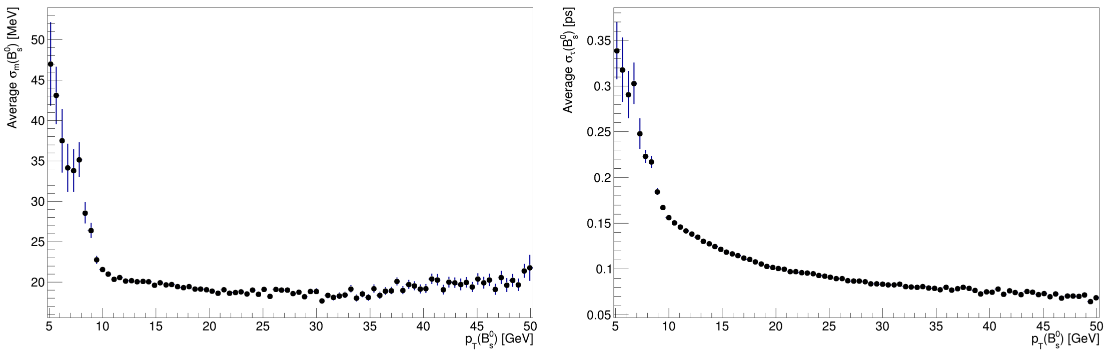

Figure 5.1: Average mass (left) and proper decay time (right) uncertainties in 2011 data plotted against p_{T} of the B_s^0 candidates.

- a prompt peak (J/ψ produced directly in the pp collision combined with two random tracks from the same primary vertex; this background has effectively zero lifetime),
- one negative exponential $e^{\frac{t_i}{\tau_{\text{neg}}}}$ for events with poor vertex resolution causing a "negative" lifetime, and
- two positive exponentials, $e^{-\frac{t_i}{\tau_{\text{pos1}}}}$ and $e^{-\frac{t_i}{\tau_{\text{pos2}}}}$, for longer-lived backgrounds (non-prompt J/ψ, combined with hadrons from the primary vertex or other B hadron in the same event),

all convoluted with the detector resolution function $\mathcal{R}(t_i|\sigma_{t_i})$, defined in equation (5.11). Using relative fractions f_{prompt}, f_{neg}, and f_{pos} for the prompt peak, negative exponential, and positive exponential respectively, the PDF can be written as

$$\begin{aligned}\mathcal{P}_{\text{bck}}(t_i|\sigma_{t_i}) = \Bigg\{ & f_{\text{prompt}} + (1-f_{\text{prompt}}) \cdot \Bigg[f_{\text{neg}} \cdot e^{\frac{t_i}{\tau_{\text{neg}}}} + (1-f_{\text{neg}}) \\ & \cdot \left(f_{\text{pos}} \cdot e^{-\frac{t_i}{\tau_{\text{pos1}}}} + (1-f_{\text{pos}}) \cdot e^{-\frac{t_i}{\tau_{\text{pos2}}}} \right) \Bigg] \Bigg\} * \mathcal{R}(t_i|\sigma_{t_i}),\end{aligned} \tag{5.13}$$

The $\mathcal{P}_{\text{bck}}(\theta_T)$, $\mathcal{P}_{\text{bck}}(\psi_T)$, and $\mathcal{P}_{\text{bck}}(\phi_T)$ functions are empirically chosen to fit the transversity background angular distributions

$$\begin{aligned}\mathcal{P}_{\text{bck}}(\theta_T) &= \frac{a_0 - a_1\cos^2(\theta_T) + a_2\cos^4(\theta_T)}{2a_0 - \frac{2}{3}a_1 + \frac{2}{5}a_2}, \\ \mathcal{P}_{\text{bck}}(\phi_T) &= \frac{1 + b_1\cos(2\phi_T + b_0)}{2\pi}, \\ \mathcal{P}_{\text{bck}}(\psi_T) &= \frac{c_0 + c_1\cos^2(\psi_T)}{2c_0 + \frac{2}{3}c_1}.\end{aligned} \tag{5.14}$$

To find reasonable starting values for $a_{0,1,2}$, $b_{0,1}$, and $c_{0,1}$ parameters, functions (5.14) are initially fitted to the angular data from the B_s^0 mass sidebands, (5.150 - 5.317) GeV and (5.417 - 5.650) GeV. However, then they are allowed to float freely in the full likelihood fit. Functions (5.14) are normalized over the ranges $-1 \leq \cos\theta_T \leq 1$, $-1 \leq \cos\psi_T \leq 1$, and $-\pi \leq \phi_T \leq \pi$, respectively.

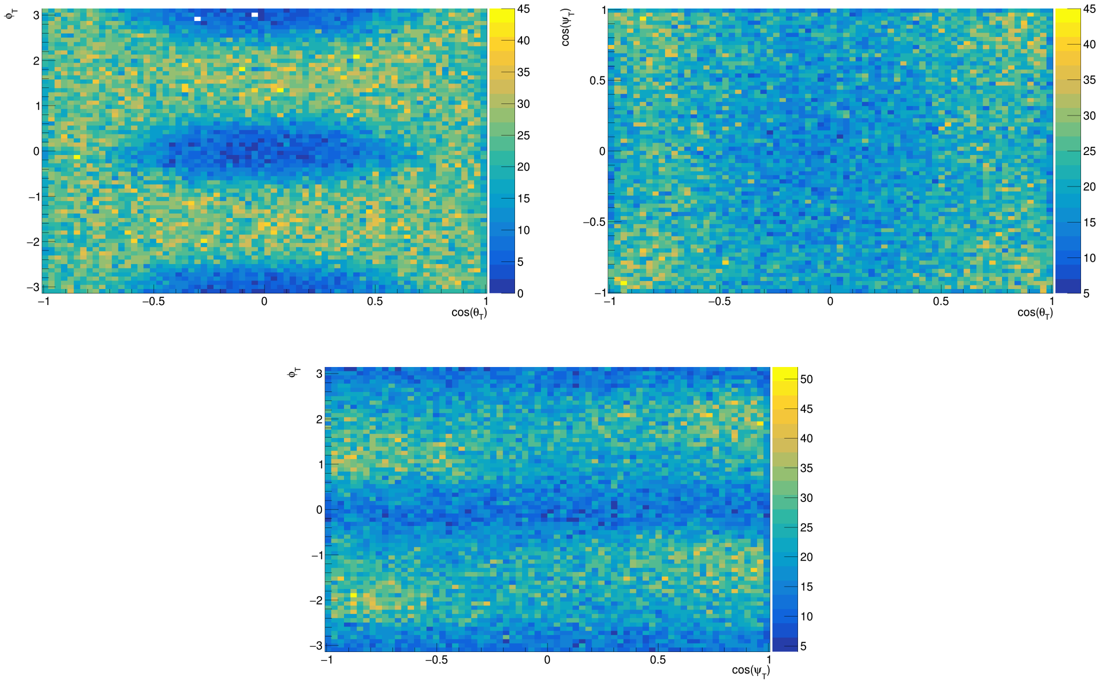

Figure 5.2: 2D histograms showing correlations between background transversity angles $(\theta_T, \psi_T, \phi_T)$ in 2011 data. Distributions are taken from B_s^0 mass sidebands (5.150 - 5.317) GeV and (5.417 - 5.650) GeV. Correlation between ϕ_T and θ_T is clearly visible (top left), while the correlation between ψ_T and the other two angles is small and can be neglected.

Correlations between the background angles are neglected in the fit and thus the angular background can be modelled with a product of three independent functions. However, as shown in figure 5.2 (top left), there is a visible correlation between ϕ_T and θ_T. A systematic error arising from the simplification thus has to be evaluated.

PDFs modelling the background mass and decay time uncertainties and the p_{T} of the background are described in section 5.2.4.

5.2.3 Specific B_d^0 Background

As mentioned in section 4.2, the data sample contains significant amount of mis-reconstructed B_d^0 events from $B_d^0 \to J/\psi(\mu^+\mu^-)K^{0*}(K^\pm\pi^\mp)$ and non-resonant $B_d^0 \to J/\psi(\mu^+\mu^-)K^\pm\pi^\mp$ decays. In these events, the $K^\pm$ mass is wrongly assigned to a final state $\pi^\pm$, forming a candidate in the B_s^0 mass range, but with shifted mass and lifetime. In the likelihood function (5.8) this background is represented by the term $\mathcal{F}_{B_d^0}(m_i, t_i, \Omega_i)$, defined as

$$\begin{aligned}\mathcal{F}_{B_d^0}(m_i, t_i, \Omega_i) = {} & \mathcal{P}_{B_d^0}(m_i) \cdot \mathcal{P}_{\text{sig}}(\sigma_{m_i}) \cdot \mathcal{P}_{B_d^0}(t_i|\sigma_{t_i}) \cdot \mathcal{P}_{B_d^0}(\theta_T) \\ & \cdot \mathcal{P}_{B_d^0}(\psi_T) \cdot \mathcal{P}_{B_d^0}(\phi_T) \cdot \mathcal{P}_{\text{sig}}(\sigma_{t_i}) \cdot \mathcal{P}_{\text{sig}}(p_{\text{T}i}). \end{aligned} \tag{5.15}$$

The mass model $\mathcal{P}_{B_d^0}(m_i)$ is described with a Landau function, because the usual Gaussian shape is distorted by the incorrect mass assignment.

The decay time model $\mathcal{P}_{B_d^0}(t_i|\sigma_{t_i})$ is described with an exponential convoluted with the same detector resolution function $\mathcal{R}(t_i|\sigma_{t_i})$, as defined in equation (5.11).

The $\mathcal{P}_{B_d^0}(\theta_T)$, $\mathcal{P}_{B_d^0}(\psi_T)$, and $\mathcal{P}_{B_d^0}(\phi_T)$ angular PDFs are described using the same functions as the other backgrounds (equations (5.14)), but with different parameters, which are obtained from the fit to MC data.

PDFs modelling the mass and decay time uncertainties and the p_{T} of the B_d^0 background are assumed to be the same as for the signal and are described in section 5.2.4.

All PDFs describing B_d^0 background components are fixed to the shapes determined from the MC studies. The fractions of these backgrounds are also fixed in the likelihood fit to values $(6.5 \pm 2.4)\%$ and $(4.5 \pm 2.8)\%$ respectively, which are calculated from the relative production fractions of the B_s^0 and B_d^0 mesons, their decay probabilities taken from [56], and from their selection efficiencies determined from MC events.

5.2.4 Time and Mass Uncertainties and p_{T} Dependence

If an event-by-event error is used in the fit and the distributions of this error differ significantly for signal and background, additional PDFs have to be used to avoid bias in the fit result [59]. As explained in previous sections, these PDFs have to be introduced for the signal and background distributions of mass and time uncertainties, and for the p_{T} distribution of B_s^0 candidates. Functions $\mathcal{P}_{\text{sig,bck}}(\sigma_{m_i,t_i})$ and $\mathcal{P}_{\text{sig,bck}}(p_{\text{T}i})$ are also found empirically. The best description is achieved using a Gamma function

$$\mathcal{P}_x(\sigma_y) = \frac{(\sigma_y - c_{x,y})^a_{x,y} \cdot \exp\left(-\frac{\sigma_y - c_{x,y}}{b_{x,y}}\right)}{b_{x,y}^{a_{x,y}+1} \cdot \Gamma(a_{x,y}+1)}, \tag{5.16}$$

where x stands for **sig** or **bck** and y stands for m_i, t_i, or $p_{\mathrm{T}i}$. Coefficients $a_{\mathrm{bck},y}$, $b_{\mathrm{bck},y}$, and $c_{\mathrm{bck},y}$ are fitted from sidebands and $a_{\mathrm{sig},y}$, $b_{\mathrm{sig},y}$, and $c_{\mathrm{sig},y}$ from sideband-subtracted signal and then fixed in the likelihood fit. Since $\mathcal{P}_{\mathrm{sig,bck}}(\sigma_{m_i,t_i})$ depend on transverse momentum of the B_s^0 (see figure 5.1), they were determined in six $p_{\mathrm{T}}(B_s^0)$ bins (see table 5.1), to reflect the natural p_{T} dependence of the detector resolution.

$p_{\mathrm{T}}(B_s^0)$ [GeV]	< 14.5	14.5-17.0	17.0-21.0	21.0-35.0	35.0-45.0	> 45.0

Table 5.1: $p_{\mathrm{T}}(B_s^0)$ bins used for determination of the $\mathcal{P}_{\mathrm{sig,bck}}(\sigma_{m_i,t_i})$ coefficients.

5.2.5 Muon Trigger Time-Dependent Efficiency

It was observed that the muon trigger biases the transverse impact parameter d_0 of muons toward smaller values. The impact parameter is used in the determination of the B_s^0 decay vertex and thus it affect the measured B_s^0 lifetime. To correct the bias, the weighting factor w_i is used in the likelihood function (5.8). To find a form of the weighting factor, the tag-and-probe method is applied to J/ψ decays to determine the trigger selection efficiency in data as a function of d_0. This function is then used to reweight the MC sample. Both initial and reweighted MC samples are fitted by a single exponential function. Comparison of these two fits leads to the weighting factor

$$w_i = \frac{\exp\left(-\frac{|t_i|}{\tau_{\mathrm{single}}+\epsilon}\right)}{\exp\left(-\frac{|t_i|}{\tau_{\mathrm{single}}}\right)}, \tag{5.17}$$

where τ_{single} is a single B_s^0 lifetime measured before the correction, using unbinned mass-lifetime maximum likelihood fit. Correction parameter $\epsilon = 0.013 \pm 0.004$ ps is obtained from the MC fits.

Chapter 6

Untagged Analysis of the 7 TeV Data

If the initial B_s^0 flavour is not known, each B_s^0 candidate has an equal chance to be a particle or an anti-particle and thus all terms containing the mass difference Δm_s cancel out in the differential decay rate (see equation (2.37) and table 2.4 in section 2.2.5). This simplified analysis (called "untagged") was a starting point for the study of the CP-violation in the $B_s^0 \to J/\psi\phi$ decay on the ATLAS experiment and it has been published in [7].

The simplification described above leads to the fact that the only remaining time-dependent amplitudes depending on $\delta_\perp$ (terms $\mathcal{O}^{(5,6)}(t)$ in table 2.4) are multiplied by $\sin\phi_s$. Previous measurement by the LHCb experiment (table 2.6) showed that ϕ_s is close to zero. The untagged fit is not sensitive to $\delta_\perp$ for such a small value of ϕ_s. Thus a Gaussian constraint to the best measured value, $\delta_\perp = (2.95 \pm 0.39)$ rad [29] is applied by adding a Gaussian function term $\mathcal{P}(\delta_\perp)$ into the likelihood function (5.8), which then turns into

$$\begin{aligned}\ln\mathcal{L} = &\sum_{i=1}^{N}\Big\{w_i\cdot\ln\Big(f_{\mathrm{sig}}\cdot\mathcal{F}_{\mathrm{sig}}(m_i,t_i,\Omega_i)+f_{\mathrm{sig}}\cdot f_{B_d^0}\cdot\mathcal{F}_{B_d^0}(m_i,t_i,\Omega_i)\\ &+(1-f_{\mathrm{sig}}(1+f_{B_d^0}))\cdot\mathcal{F}_{\mathrm{bck}}(m_i,t_i,\Omega_i)\Big)\Big\}+\ln\big(P(\delta_\perp)\big).\end{aligned} \qquad (6.1)$$

The differential decay rate defined in equation (2.37) is normalized such that the squares of the amplitudes sum to unity. Three of the four amplitudes are fit parameters and $|A_\perp(0)|^2$ is determined according to this constraint as

$$|A_\perp(0)|^2 = 1 - |A_0(0)|^2 - |A_\parallel(0)|^2 - |A_S(0)|^2. \qquad (6.2)$$

6.1 Results of the Fit

Unfortunately, the differential decay rate given in equation (2.37) is invariant under the following simultaneous transformations:

$$\{\phi_s, \Delta\Gamma_s, \delta_\perp, \delta_\parallel, \delta_S\} \rightarrow \{\pi - \phi_s, -\Delta\Gamma_s, \pi - \delta_\perp, -\delta_\parallel, -\delta_S\}. \tag{6.3}$$

In addition, for the untagged analysis, it is also invariant under the transformation

$$\{\phi_s, \Delta\Gamma_s, \delta_\perp, \delta_\parallel, \delta_S\} \rightarrow \{-\phi_s, \Delta\Gamma_s, \pi - \delta_\perp, -\delta_\parallel, -\delta_S\}, \tag{6.4}$$

which leads to a fourfold ambiguity.

Since the LHC*b* measurement [29] used for the Gaussian constraint on $\delta_\perp$ is tagged, only the two minima of the likelihood function with positive ϕ_s are considered. Another measurement performed by LHC*b* [61] determined the parameter $\Delta\Gamma_s$ to be also positive and thus only one answer remains.

In total, the unbinned maximum likelihood fit of the untagged measurement contains 26 free parameters, including the eight physics parameters ϕ_s, Γ_s, $\Delta\Gamma_s$, $|A_0(0)|^2$, $|A_\parallel(0)|^2$, $|A_S(0)|^2$, $\delta_\parallel$, and δ_S. Other parameters describe the B_s^0 mass distribution, B_s^0 signal fraction, background events, and the two scale factors for mass and decay time uncertainties.

Results of the untagged fit to 4.9 fb^{-1} of 7 TeV *pp* data recorded by the ATLAS experiment in 2011 are shown in table 6.1. The $\delta_\parallel$ parameter is fitted very close to its symmetry point at π and the pull studies (discussed in the following section) show a non-Gaussian distribution for this parameter. Thus the result for the strong phase $\delta_\parallel$ is given in the form of a 1σ confidence interval (3.04 - 3.24) rad. The S-wave amplitude $|A_S(0)|^2$ is found to be consistent with zero and the strong phase is fitted relative to $\delta_\perp$, as $\delta_\perp - \delta_S = (0.03 \pm 0.13)$ rad. The number of signal B_s^0 meson candidates extracted from the fit is 22690 ± 160.

Fit projections of the mass and the proper decay time, mass and proper decay time uncertainties, and angles (in the mass signal region) are shown in figures 6.1, 6.2, and 6.3 respectively. Table 6.2 shows the correlations between the physics parameters. Large correlation between the Γ_s and $\Delta\Gamma_s$ parameters is expected because of the definition of these parameters. The systematic uncertainties and comparison with other experiments and the SM are discussed in the next sections.

Parameter	Value	Stat. uncertainty
ϕ_s [rad]	0.22	0.41
$\Delta\Gamma_s$ [ps^{-1}]	0.053	0.021
Γ_s [ps^{-1}]	0.677	0.007
$\|A_0(0)\|^2$	0.528	0.006
$\|A_\parallel(0)\|^2$	0.220	0.008
$\|A_S(0)\|^2$	0.02	0.02
$\delta_\perp$ [rad]	Gauss constraint (2.95 ± 0.39)	
$\delta_\perp - \delta_S$ [rad]	0.03	0.13
$\delta_\parallel$ [rad]	3.04 - 3.24	

Table 6.1: Values for the physics parameters along with their statistical uncertainties, obtained from the untagged fit to the 7 TeV data. The S-wave strong phase is fitted relative to $\delta_\perp$, as $\delta_\perp - \delta_S$. The result for the strong phase $\delta_\parallel$ is given in the form of a 1σ confidence interval.

	ϕ_s	$\Delta\Gamma_s$	Γ_s	$\|A_0(0)\|^2$	$\|A_\parallel(0)\|^2$	$\|A_S(0)\|^2$
ϕ_s	1.00	-0.13	0.38	-0.03	-0.04	0.02
$\Delta\Gamma_s$		1.00	-0.60	0.12	0.11	0.10
Γ_s			1.00	-0.06	-0.10	0.04
$\|A_0(0)\|^2$				1.00	-0.30	0.35
$\|A_\parallel(0)\|^2$					1.00	0.09
$\|A_S(0)\|^2$						1.00

Table 6.2: Correlations between the physics parameters obtained from the untagged fit to the 7 TeV data.

6.2 Systematic Uncertainties

Detector effects and the fit model assumptions that are not accounted for in the likelihood fit are evaluated as systematic uncertainties. These are described in following sections. Calculated errors are then added in quadratures resulting in a total systematic uncertainty for each physics variable as shown in table 6.3.

6.2.1 Muon Trigger Time-Dependent Efficiency

As discussed in section 5.2.5, the events are re-weighted using equation (5.17) to account for the lifetime bias caused by the muon triggers. To obtain systematic uncertainties for this model, the likelihood fit is performed using the both values

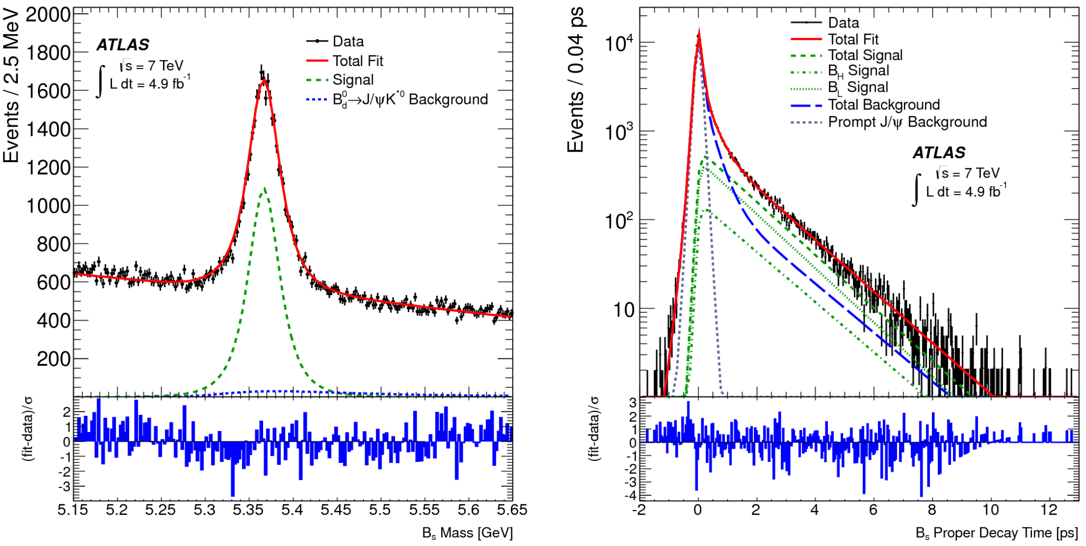

Figure 6.1: Mass (left) and proper decay time (right) fit projections for the background component (dotted blue), the signal component (dashed green), and the total fit (red line) to the untagged 7 TeV data. In the proper decay time plot also the heavy and light components of the signal (dotted and alternating dotted green) are shown, as well as the prompt J/ψ background component (dashed purple). Data are shown as black points. The pull distribution at the bottom shows the difference between the data and the fit value normalized to the data uncertainty.

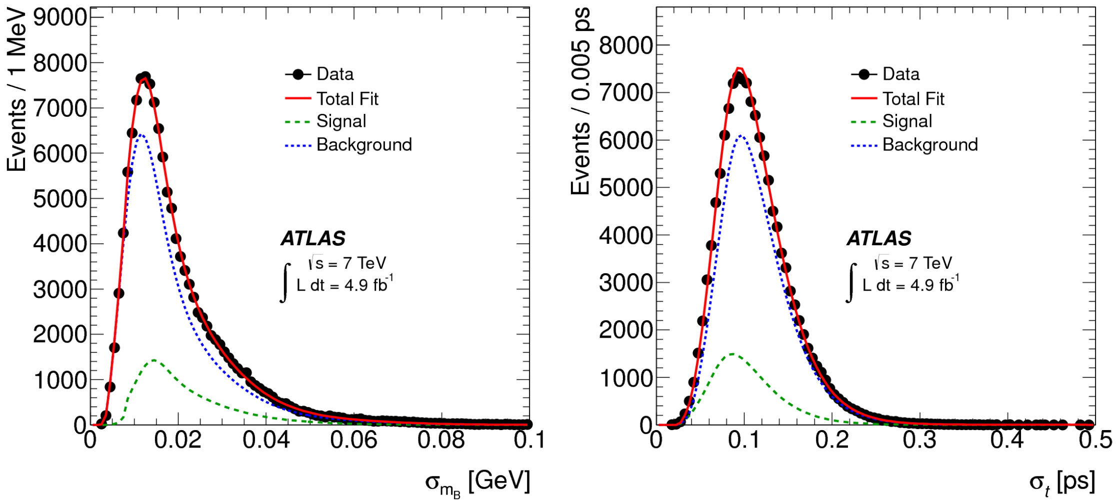

Figure 6.2: Mass (left) and proper decay time (right) uncertainty distributions for the 7 TeV data (black points) together with the fit projections for the background fraction (dotted blue), the signal fraction (dashed green), and the sum of the two fits (red line).

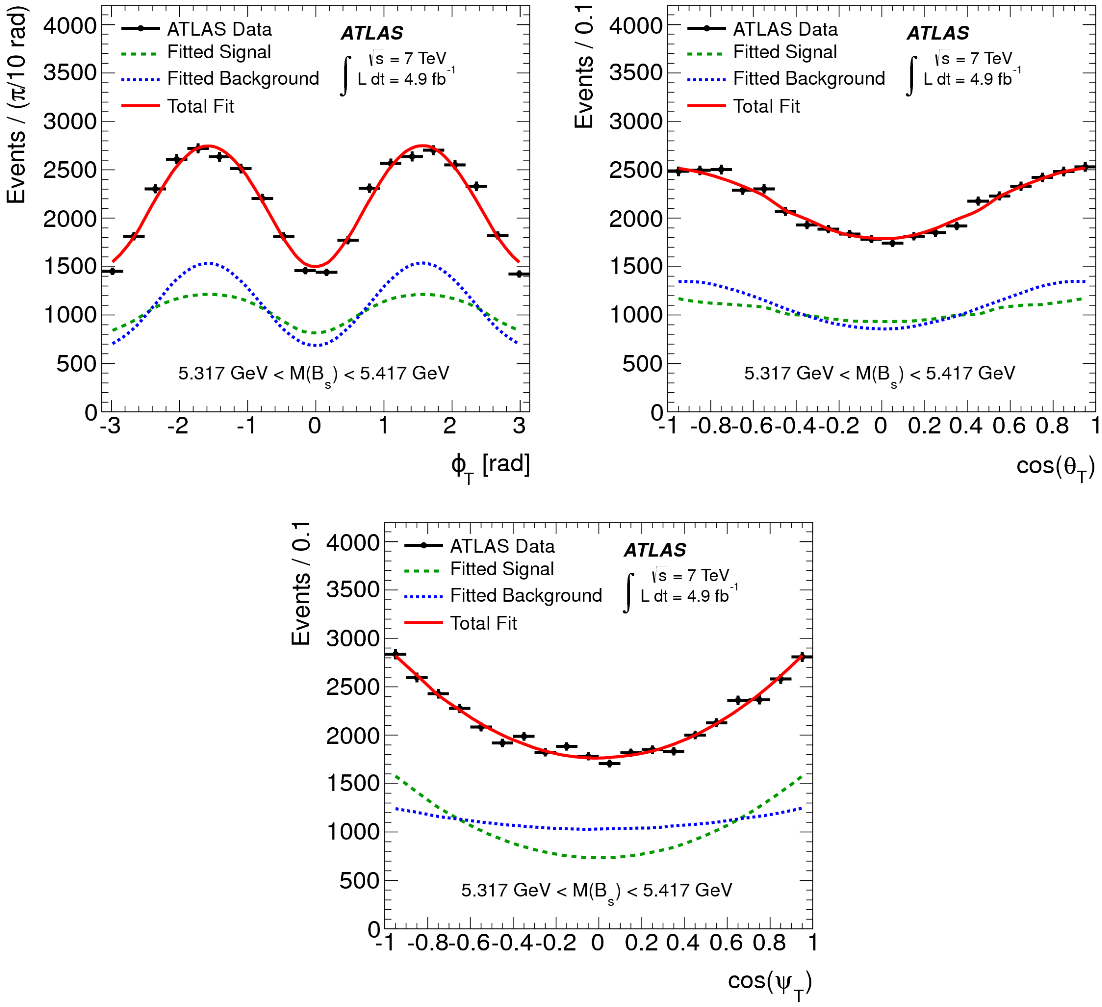

Figure 6.3: Fit projections for transversity angles ϕ_T (left top), $\cos\theta_T$ (top right), and $\cos\psi_T$ (bottom) for events with B_s^0 mass from signal region (5.317-5.417) GeV.

$\epsilon^{\pm} = 0.013 \pm 0.004$ ps . The larger deviation to the default fit result for each parameter is taken as systematic uncertainty.

6.2.2 B_d^0 Contribution to the Background

The data sample contains significant amount of mis-reconstructed B_d^0 events from $B_d^0 \to J/\psi(\mu^+\mu^-)K^{0*}(K^{\pm}\pi^{\mp})$ and non-resonant $B_d^0 \to J/\psi(\mu^+\mu^-)K^{\pm}\pi^{\mp}$ decays. The fractions of these backgrounds are fixed in the likelihood fit to values $(6.5 \pm 2.4)\%$ and $(4.5 \pm 2.8)\%$ respectively. To estimate the systematic uncertainty arising from the precision of the fraction estimates, the data are fitted with these fractions increased and decreased by their errors. Again, the larger deviation to the default fit result for each parameter is taken as systematic uncertainty.

6.2.3 Inner Detector Alignment

The knowledge of the exact position of the sensitive detector elements is crucial for this analysis, since the misalignments of the ID affect the impact parameter d_0 with respect to the primary vertex. The effect of misalignment is estimated using events simulated with perfect and distorted ID geometries, where the distorted geometry is produced by moving detector components to match the observed small shifts in data.

The impact parameter distribution with respect to the primary vertex as a function of η and ϕ in 25×25 grid is measured using the real data. For each bin the d_0 distribution is then fitted by a Gaussian function and the mean value is stored in a histogram, as shown in figure 6.4 (left).

To produce the distorted MC sample, the simulated tracks from the original sample are distorted using the information from the histogram discussed above. The d_0 parameter of each input track as a function of η and ϕ is forced to the value measured in data. Tracks are then passed to the track based alignment algorithm [62], used for the alignment of the ATLAS ID. The alignment algorithm automatically changes the detector geometry in order to minimize the residuals obtained from the distorted track. Since the Pixel detector dominates the d_0 measurement, only this subdetector geometry is changed. The distorted ID geometry is stored in a file. The 2D $\eta - \phi$ histogram of the distorted d_0 distribution is shown in figure 6.4 (right) and reproduces nicely the shape and size of the d_0 offset as observed in data 6.4 (left).

The geometry file is used to reconstruct simulated B_s^0 events. The difference between the parameters determined with the unbinned maximum likelihood fit obtained with simulated events reconstructed with and without misaligned geometry is used to determine the systematic uncertainty for the ID alignment.

6.2.4 Angular Acceptance Method

The angular acceptance is calculated from a binned fit to MC data and the statistical error is smaller than 1 % in any bin. However, two simplifications are made in the construction of the acceptance map – it is expected and observed that the transversity angles are symmetrical about zero and thus only absolute values are used. It is also observed that $\cos\psi_T$ is flat so this has only one bin assigned to it. The second bin in plots shown in figure 6.5 is comparing the symmetrized angular acceptances with those where the symmetry is not used.

As described in section 5.2.1, the angular acceptance corrections are p_{T} dependent and thus constructed in several $p_{\mathrm{T}}(B_s^0)$ bins. Possible dependences of the results

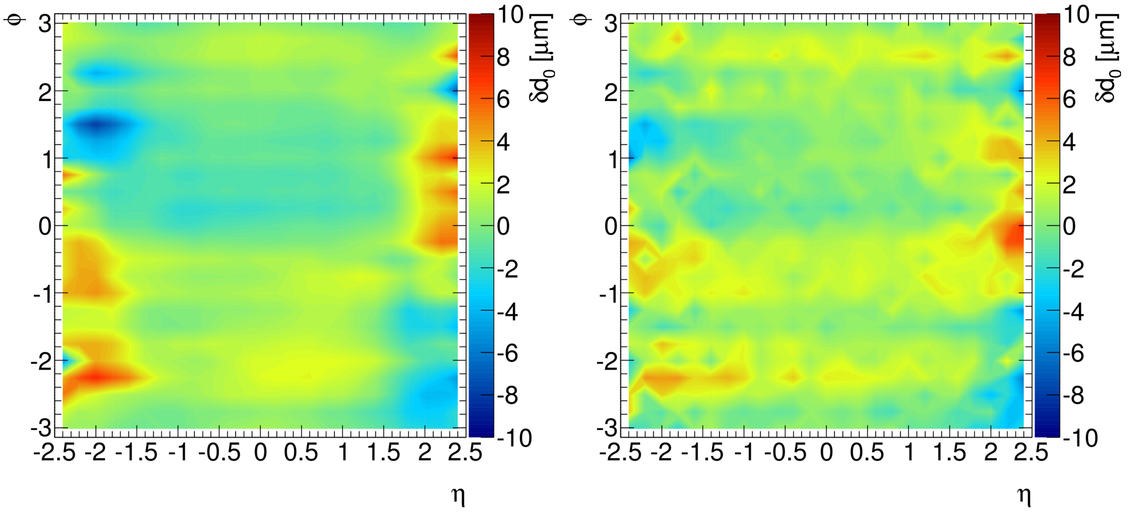

Figure 6.4: The impact parameter d_0 distribution with respect to the primary vertex as a function of η and ϕ measured with data (left) and simulated events using the ID geometry distorted with the information obtained from data (right).

on the choice of the binning are tested by varying bin widths and central values, as shown in figure 6.5.

In addition to the prior normalization of acceptances in p_{T} bins, the precise likelihood fit requires normalization of the product $\mathcal{A}_{\mathrm{sig}}(\Omega_i, p_{\mathrm{T}i}) \cdot \mathcal{P}_{\mathrm{sig}}(\Omega_i, t_i|\sigma_{t_i})$ over the angular part (see section 5.2.1). Several numerical integration methods are tested: using simple 3D histogram method with various binning or using ROOT 3D function (TF3) integration. Results of this comparison is shown on figure 6.6. For completeness, the last bin shows the test, where the $\mathcal{A}_{\mathrm{sig}}(\Omega_i, p_{\mathrm{T}i})$ and $\mathcal{P}_{\mathrm{sig}}(\Omega_i, t_i|\sigma_{t_i})$ PDFs are normalized separately, which cause the large bias of the fit result.

Taking all these results into consideration, the systematic uncertainties due to detector acceptance are found to be negligible.

6.2.5 Default Fit Model

To determine whether the likelihood fit is unbiased, the default model is tested in Toy Monte Carlo (ToyMC) pseudo-experiments. First, real data are fitted with the default model and the result is then used as an input for the ToyMC generator. Set of 1000 pseudo-experiments (each containing distributions for 121761 B_s^0 candidates, i.e. the same number as in the real data) is generated and each sample is then fitted with the default model. The pull for the given parameter and the given sample is

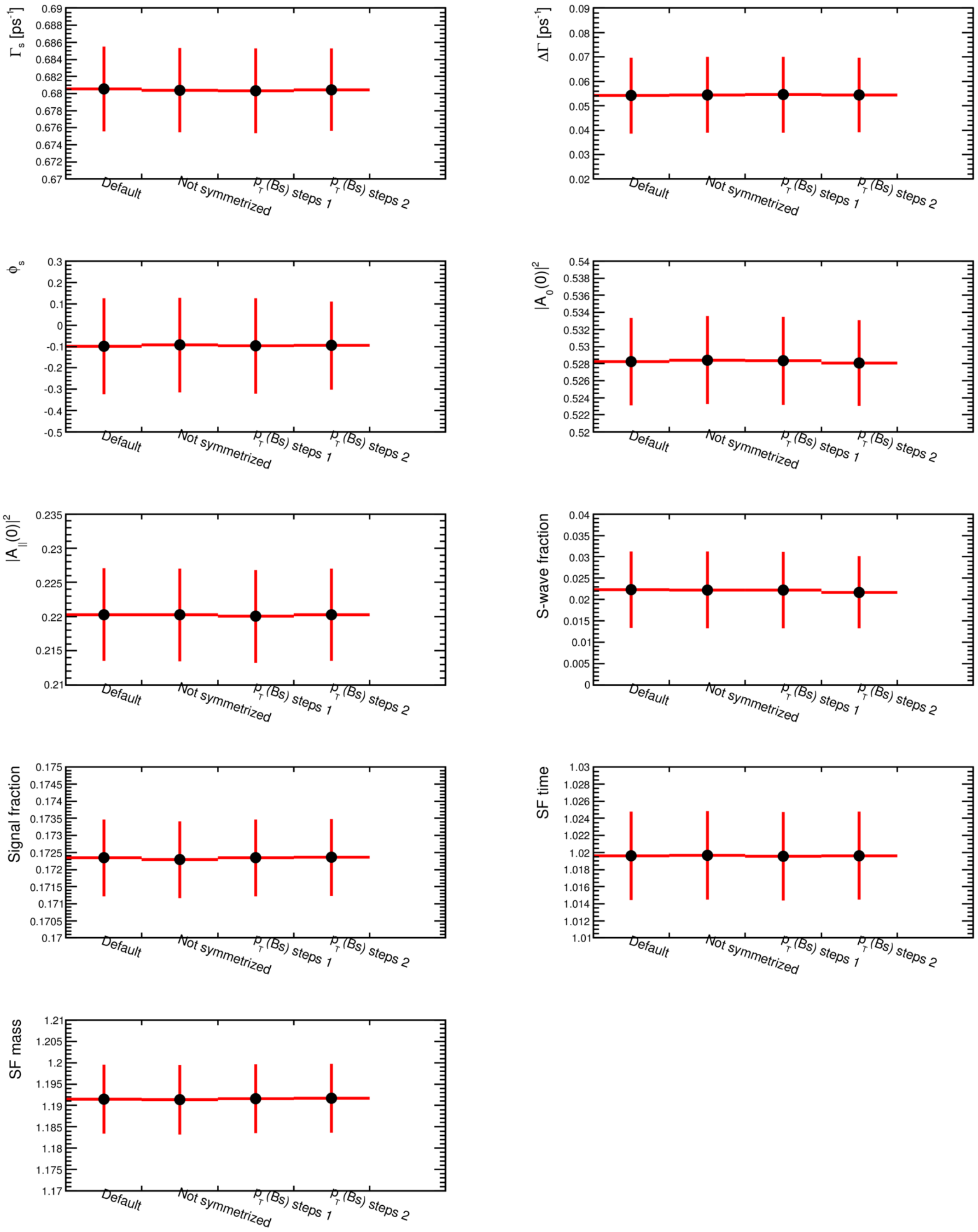

Figure 6.5: Fit results using various p_{T} binning used to construct the acceptance maps and the test comparing the symmetrized angular acceptances with those where the symmetry is not used (the second bin in the plots).

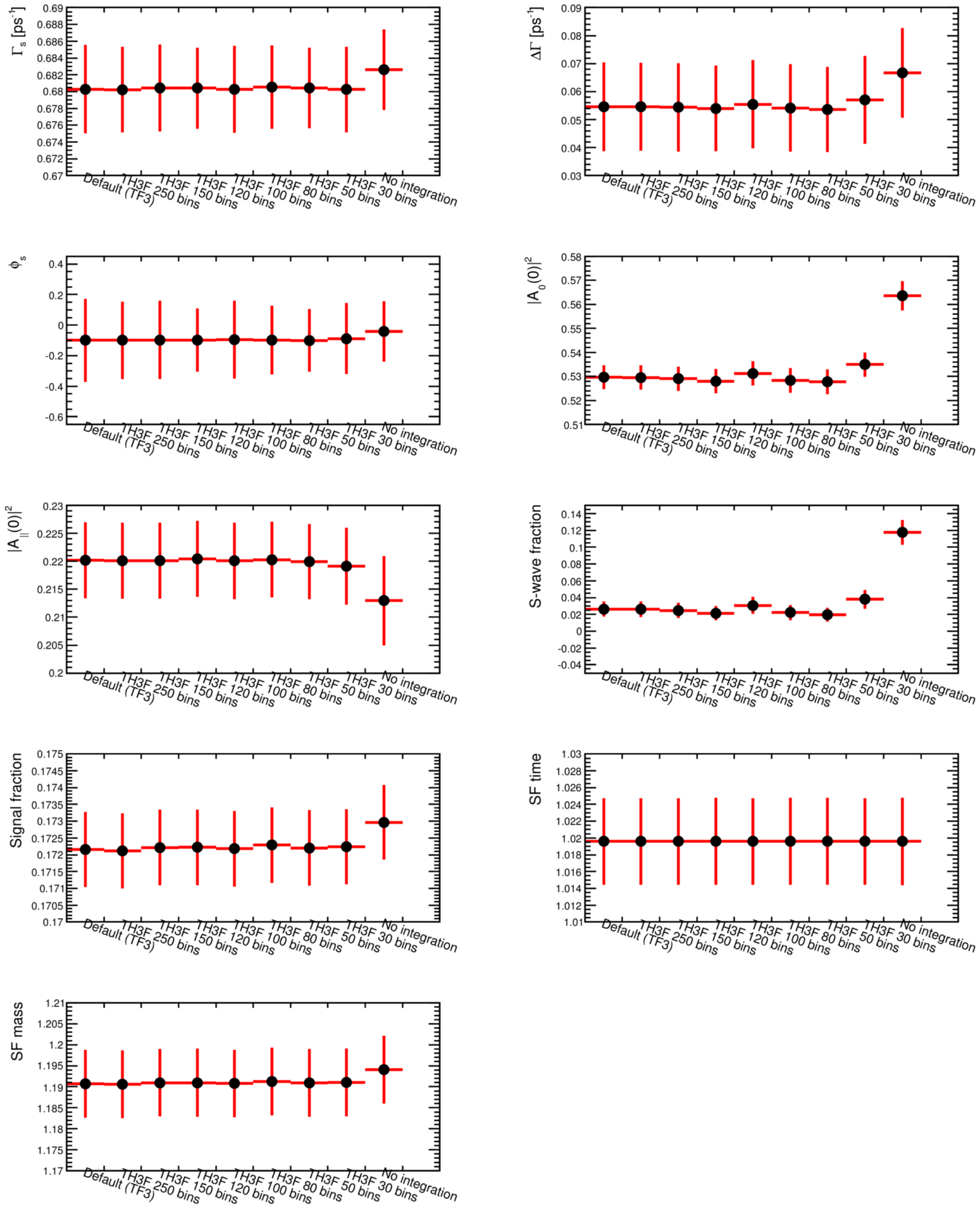

Figure 6.6: Fit results using various integration techniques to normalize the acceptance maps. The last point shows bias of the fit results in case the $\mathcal{A}_{\mathrm{sig}}(\Omega_i, p_{\mathrm{T}i})$ and $\mathcal{P}_{\mathrm{sig}}(\Omega_i, t_i|\sigma_{t_i})$ terms are normalized separately.

then calculated as

$$\text{pull} = \frac{\text{fitted value - generated value}}{\text{fitted error}}. \tag{6.5}$$

Pulls are filled into a histogram and fitted with a Gaussian function. An unbiased fit procedure would show a Gaussian distributed parameters around 0 with a sigma of 1. The systematic error quoted for the default model is then calculated using the bias of the pull distribution, multiplied by the statistical uncertainty of each parameter.

Figure 6.7 shows the pull distribution for the strong phase $\delta_{||}$. This parameter is fitted very close to its symmetry point at π and the pull distribution has a non-Gaussian behaviour. Thus the result for the strong phase $\delta_{||}$ is given in the form of a 1σ confidence interval (3.04 - 3.24) rad.

Other pull distributions for the default model is shown in figure 6.8. The $\Delta\Gamma_s$ and δ_S distributions show deviations from the perfect scenario (0.32 and -0.26, respectively) and thus introduce larger systematics uncertainties into the analysis results. The plots for all other parameters are in agreement with an unbiased fit.

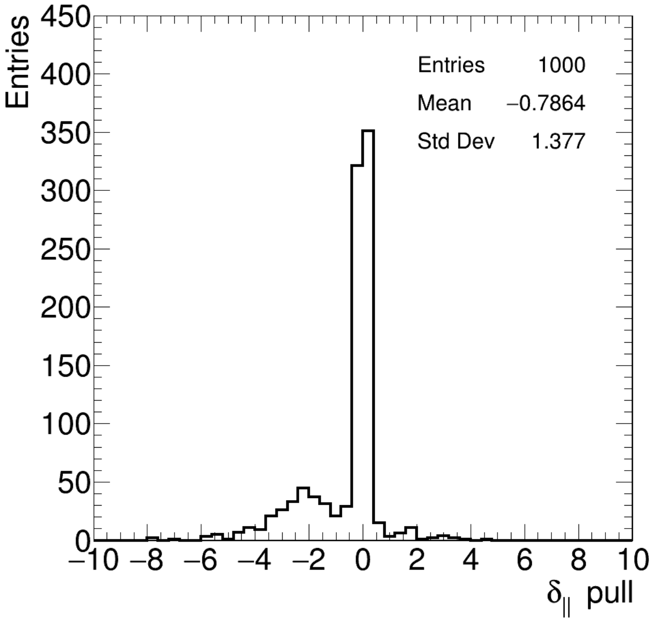

Figure 6.7: Pull distribution for the strong phase $\delta_{||}$ from 1000 pseudo-experiments showing a non-Gaussian behaviour.

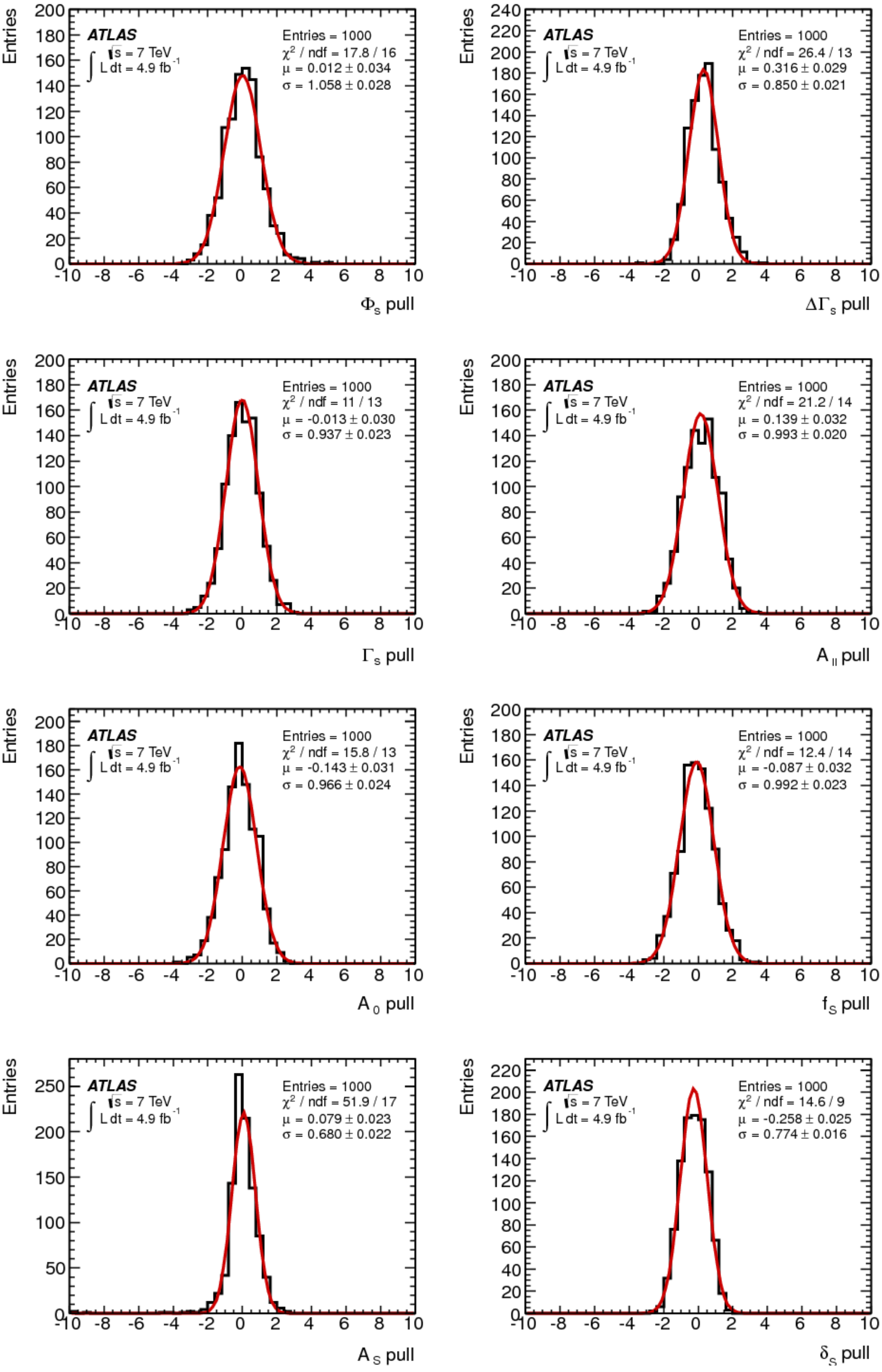

Figure 6.8: Pull distributions of the measured parameters from 1000 pseudo-experiments fitted with a Gaussian function. The results from the real data fit are taken as input values for the generation of pseudo-events.

6.2.6 Alternative Fit Models

In order to estimate the size of systematic uncertainties caused by the assumptions made in the fit model, alternative models are tested using the same pull technique as described above. Tested fit variations make use of either a complicated function to describe the model or an alternative way to obtain a ToyMC distribution (sampling from the real data). For each model variation 1000 pseudo-experiments are generated and then fitted using the default fit model. The considered alternative models are described below.

Signal Mass Model The default model fit uses a single mass scale factor s_m for the B_s^0 mass (see section 5.2.1). As an alternative model, a double Gaussian function with a common mean M and widths $\sigma_{m,1}$ and $\sigma_{m,2}$ is used to fit the data and to generate ToyMC pseudo-experiments:

$$\begin{aligned}\mathcal{P}'_{\text{sig}}(m_i) = f_{\sigma_m} \cdot \frac{1}{\sqrt{2\pi}\,\sigma_{m,1}} e^{-\left(\frac{m_i - M}{\sqrt{2}\,\sigma_{m,1}}\right)^2} \\ + (1 - f_{\sigma_m}) \cdot \frac{1}{\sqrt{2\pi}\,\sigma_{m,2}} e^{-\left(\frac{m_i - M}{\sqrt{2}\,\sigma_{m,2}}\right)^2},\end{aligned} \tag{6.6}$$

where f_{σ_m} is a fraction of the two Gaussian functions with the same mean. Values used for the generation are found to be $f_{\sigma_m} = 0.67$, $\sigma_{m,1} = 17.3$ MeV, and $\sigma_{m,2} = 45.1$ MeV.

Background Mass Model Instead of using a linear function for the background mass model, an exponential function is used as an alternative PDF:

$$\mathcal{P}'_{\text{bck}}(m_i) = \frac{1}{N'_{m,\text{bck}}} \left(1 + p_0 \cdot e^{-\frac{m_i - p_1}{p_2}}\right), \tag{6.7}$$

where parameters are found to be $p_0 = 5.445$, $p_1 = 5375$ MeV, $p_2 = 988$ MeV, and $N'_{m,\text{bck}}$ is given by the normalization over the range (5.15 - 5.65) GeV.

Signal Resolution Model The time resolution for signal events $\mathcal{R}(t_i|\sigma_{t_i})$ is modelled by a single Gaussian distribution, making use of event-by-event errors scaled by a single scale factor s_t (see equation (5.11)). Pseudo-experiments make use of an alternative model with a double Gaussian function with two different scale factors $s_{t,1}$ and $s_{t,2}$ as follows

$$\begin{aligned}\mathcal{R}'(t_i|\sigma_{t_i}) = f_{s_t} \cdot \frac{1}{\sqrt{2\pi}\,\sigma_{t_i} s_{t,1}} e^{-\left(\frac{t_i}{\sqrt{2}\,\sigma_{t_i} s_{t,1}}\right)^2} \\ + (1 - f_{s_t}) \cdot \frac{1}{\sqrt{2\pi}\,\sigma_{t_i} s_{t,2}} e^{-\left(\frac{t_i}{\sqrt{2}\,\sigma_{t_i} s_{t,2}}\right)^2},\end{aligned} \tag{6.8}$$

where f_{s_t} is a fraction of the two Gaussian functions with the same zero mean. Values of the parameters are found to be $f_{s_t} = 0.8$, $s_{t,1} = 0.96$, and $s_{t,2} = 1.10$.

Background Lifetime Model Parametrization of the background lifetime uses a prompt peak, one negative exponential, and two positive exponentials, as defined in equation (5.13). An alternative model generates the background lifetime by sampling data from the B_s^0 mass sidebands.

Background Angles Model ToyMC samples are generated with background angles taken randomly from the histograms from B_s^0 mass sidebands data. To account for untreated correlations in the background angles, first the angle θ_T is generated, then based on this value, ψ_T is selected from one of four sidebands ψ_T histograms binned in θ_T.

Pull distributions of the variations described above show similar behaviour as the default model pulls (figure 6.8). Systematic uncertainties for the default model and for all considered variations are summarized in table 6.3.

Systematics	ϕ_s [rad]	$\Delta\Gamma_s$ [ps^{-1}]	Γ_s [ps^{-1}]	$\lvert A_\parallel(0)\rvert^2$	$\lvert A_0(0)\rvert^2$	$\lvert A_S(0)\rvert^2$
ID Alignment	0.04	< 0.001	0.001	< 0.001	< 0.001	< 0.01
Trigger Efficiency	< 0.01	< 0.001	0.002	< 0.001	< 0.001	< 0.01
Default Fit Model	< 0.001	0.006	< 0.001	< 0.001	0.001	< 0.01
Sig. Mass Model	0.02	0.002	< 0.001	< 0.001	< 0.001	< 0.01
Bck. Mass Model	0.03	0.001	< 0.001	0.001	< 0.001	< 0.01
Resolution Model	0.05	< 0.001	0.001	< 0.001	< 0.001	< 0.01
Bck. Lifetime Model	0.02	0.002	< 0.001	< 0.001	< 0.001	< 0.01
Bck. Angles Model	0.05	0.007	0.003	0.007	0.008	0.02
B_d^0 Contribution	0.05	< 0.001	< 0.001	< 0.001	0.005	< 0.01
Total	0.10	0.010	0.004	0.007	0.009	0.02

Table 6.3: Summary of systematic uncertainties assigned to parameters of interest. The total uncertainties are calculated as $\sqrt{\sum_i \sigma_i^2}$.

6.3 Summary and Comparison of the Results

Physical parameters describing the CP-violation in the $B_s^0 \to J/\psi\phi$ decay channel obtained in the untagged analysis of the 7 TeV pp data delivered to the ATLAS experiment in 2011 are summarized in table 6.4, together with their statistical and systematic uncertainties. Measured values are consistent with theoretical expectations, in particular ϕ_s is within 1σ of the Standard Model prediction. This is also presented in figure 6.9, where a likelihood contours in the $\phi_s - \Delta\Gamma_s$ plane for the 68%, 90%, and 95% confidence intervals are shown.

Parameter	Value	Stat. Uncertainty	Syst. Uncertainty
ϕ_s [rad]	0.22	0.41	0.10
$\Delta\Gamma_s$ [ps^{-1}]	0.053	0.021	0.010
Γ_s [ps^{-1}]	0.677	0.007	0.004
$\|A_0(0)\|^2$	0.528	0.006	0.009
$\|A_\parallel(0)\|^2$	0.220	0.008	0.007
$\|A_S(0)\|^2$	0.02	0.02	0.02

Table 6.4: Fitted values for the physics parameters along with their statistical and systematic uncertainties for the 7 TeV data untagged analysis.

	ϕ_s [rad]	$\Delta\Gamma_s$[ps^{-1}]	Ref.
D0	$-0.55^{+0.38}_{-0.36}$	$0.163^{+0.065}_{-0.064}$	[27]
CDF	$[-0.60, 0.12]$, 68 % CL	$0.068 \pm 0.026 \pm 0.009$	[28]
LHC*b*	$-0.001 \pm 0.101 \pm 0.027$	$0.116 \pm 0.018 \pm 0.006$	[29], update [30]
ATLAS	$0.22 \pm 0.41 \pm 0.10$	$0.053 \pm 0.021 \pm 0.010$	[7]
HFLAG	$-0.013^{+0.083}_{-0.090}$	$0.089^{+0.011}_{-0.013}$	[63]
SM	$-0.0363^{+0.0016}_{-0.0015}$	0.087 ± 0.021	[24], [64], resp.

Table 6.5: Summarized results of $B_s^0 \to J/\psi\phi$ CPV measurements from D0, CDF, LHC*b*, and ATLAS (untagged analysis) experiments. The first error is due to statistics, the second one to systematics. HFLAG combined result is based also on the LHC*b* $B_s^0 \to J/\psi\pi\pi$ measurement. SM stands for the Standard Model prediction.

Table 6.5 summarizes results of $B_s^0 \to J/\psi\phi$ CPV measurements from D0, CDF, LHC*b*, and ATLAS experiments, their combined result calculated by Heavy Flavor Averaging Group (HFLAG) and the SM prediction. All measurements, as well as the combined result, are consistent with the SM expectation. 68 % CL contours in the $\phi_s - \Delta\Gamma_s$ plane obtained from individual and combined D0, CDF, LHC*b*, and ATLAS measurements are shown in figure 6.10.

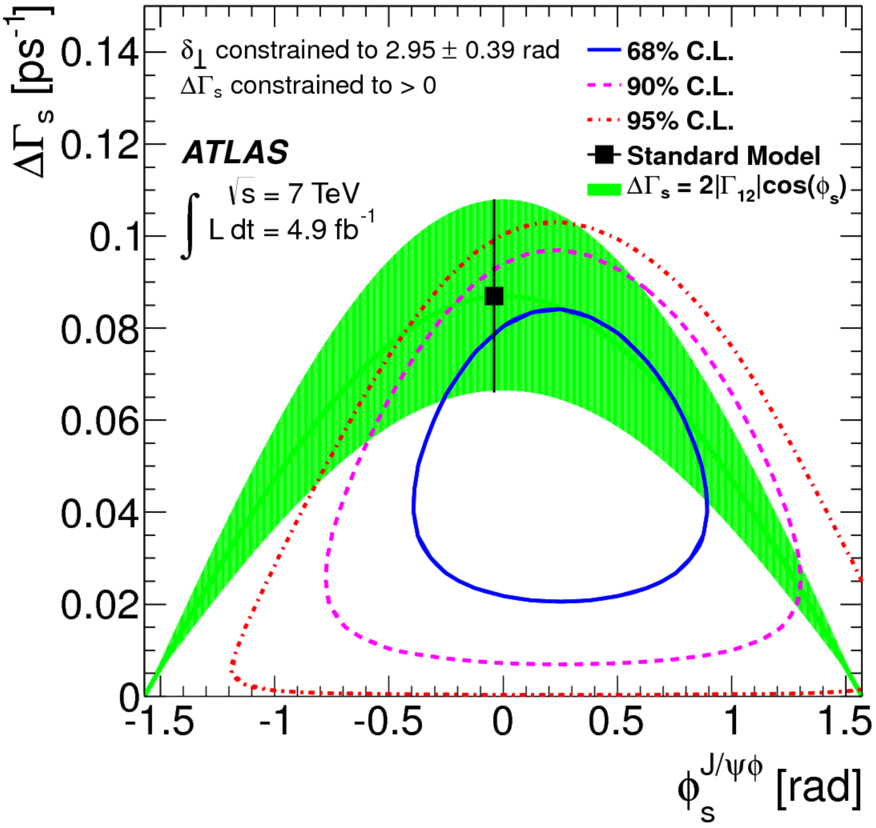

Figure 6.9: Likelihood contours in the $\phi_s - \Delta\Gamma_s$ plane, showing the 68%, 90%, and 95% confidence intervals (using statistical errors only). The green band is the theoretical prediction of mixing-induced *CP*-violation.

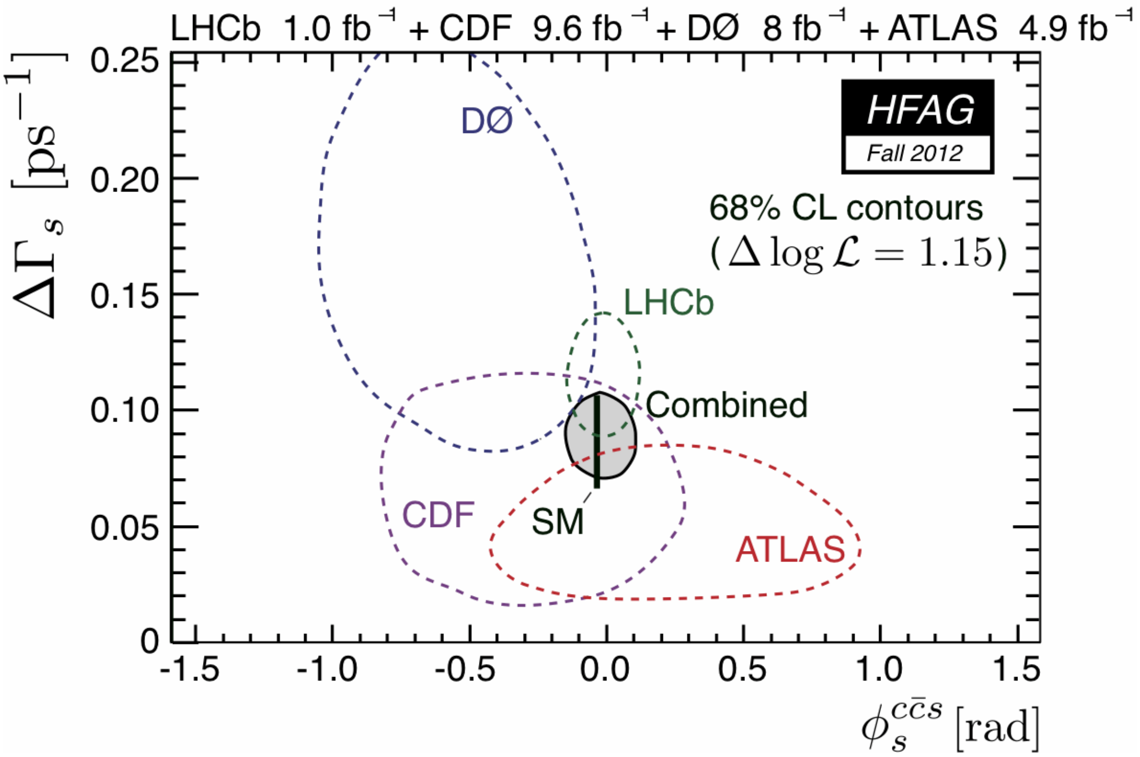

Figure 6.10: 68 % CL regions in B_s^0 width difference $\Delta\Gamma_s$ and weak phase ϕ_s obtained from individual and combined D0, CDF, LHC*b*, and ATLAS measurements (update of figure 2.6). The SM expectation is shown as the black rectangle. Taken from [63].

Chapter 7

Tagged Analysis of the 7 TeV Data

The determination of the initial flavour of neutral mesons, so called *flavour tagging*, can improve any CP-violation measurement. To update the previous analysis to use the tagging is thus a logical step. Flavour tagging can significantly reduce the uncertainty of the weak phase ϕ_s and also the strong phase $\delta_\perp$ can be extracted using the likelihood fit. Results of the tagged analysis have been published in [8].

At the LHC B-mesons are produced in the hadronization of $b\bar{b}$ pairs. The majority of these pairs are produced either both in the forward or both in the backward direction of the detector. Tagging algorithms are usually divided into two group: **Same-Side Taggers** exploit the correlation with particles produced in the hadronization process of the signal B-meson, while **Opposite-Side Taggers** (OST) infer the flavour of a given B-meson from the identification of the flavour of the other B-meson typically produced in the same event. The second mentioned method is used in the presented analysis and is described in the following section.

7.1 Flavour Tagging

Several methods are available to infer the flavour of the opposite-side b-quark, with varying efficiencies and discriminating powers. The quality and power of a given tagger can be quantified by the tag efficiency ϵ_{tag}, the tag dilution $\mathcal{D}_{\text{tag}}$, and the tagging power P_{tag}. The tag efficiency is simply a fraction of tagged candidates

$$\epsilon_{\text{tag}} = \frac{N_{\text{tagged}}}{N_{\text{total}}}, \tag{7.1}$$

where N_{tagged} is the number of tagged B_s^0 candidates and N_{total} is the total number of B_s^0 candidates. The tag dilution is defined as

$$\mathcal{D}_{\text{tag}} = 1 - \frac{2\,N_{\text{wrong}}}{N_{\text{tagged}}}, \tag{7.2}$$

where N_{wrong} is the number of wrongly tagged B_s^0 candidates. Dilution is the factor by which measured CP and mixing asymmetries are reduced from their physical values due to incorrectly assigned flavour tags. The tagging power can be then calculated as

$$P_{\text{tag}} = \epsilon_{\text{tag}} \cdot \mathcal{D}^2_{\text{tag}}. \tag{7.3}$$

This definition is motivated by the fact that the statistical uncertainties on CP asymmetry measurements generally scale approximately as $1/\sqrt{P_{\text{tag}}}$ (for more details see [18]).

7.1.1 Tagging Methods

Measuring charge of the muon from the semileptonic decay of the opposite-side B-meson can provide strong separation power, but the method has several disadvantages. At the first place, it is the lower efficiency, because only 10 % of B-mesons decay into leptons [11]. In the case of neutral B-mesons the $b \to \mu$ transition can be diluted through the meson oscillation. And the sign of the muon can be also altered by the cascade decay $b \to c \to \mu$. However, this method can be improved using a weighted sum of the charge of the tracks in a cone around the muon

$$Q_\mu = \frac{\sum_i^{N_{\text{tracks}}} q_i\, p_{\text{T}i}^{\kappa}}{\sum_i^{N_{\text{tracks}}} p_{\text{T}i}^{\kappa}}, \tag{7.4}$$

where N_{tracks} is number of tracks in the cone size $\Delta R = \sqrt{(\Delta\eta)^2 + (\Delta\phi)^2} < 0.5$ around the leading muon, and q_i and $p_{\text{T}i}$ are charge and p_{T} of the track, respectively. The constant $\kappa = 1.1$ is found empirically to achieve the best tagging performance. The *muon cone charge* defined in equation (7.4) is used when an **additional** muon is present in the event, with $p_{\text{T}} > 2.5$ GeV, $|\eta| < 2.5$, and with $|\Delta z| < 5$ mm from the primary vertex associated with the signal B_s^0. Muon is required to be either combined or segment tagged (see section 4.3) and in case of more than one muon, the muon with the highest transverse momentum is selected. Used tracks are required to have an impact parameter with $|\Delta z| < 5$ mm from same PV, with $p_{\text{T}} > 500$ MeV and $|\eta| < 2.5$, passing the hit quality selection criteria (at least one hit in the Pixel detector and at least four hits in the SCT). Tracks from the signal decay are explicitly excluded from the sum (7.4).

If no additional muon is present, a weighted sum of the charge of tracks associated with the opposite-side B-meson decay can provide some separation. The method takes a b-tagged jet [65], if present in the event, that is composed of tracks originating from the same PV as the signal decay (excluding those from the signal B_s^0 candidate). The jets are seeded from calorimeter clusters, with minimum energy threshold of 10 GeV. Also those within a cone of $\Delta R < 0.5$ of the B_s^0 signal momentum axis are excluded. The jets are reconstructed using the anti-k_t jet clustering algorithm [66] with a cone size of 0.6. In the case there is more than one jet in the event, the jet with the highest value of the b-tag weight[11] is used. Similarly to the muon cone charge, a *jet charge* is calculated from the tracks associated to the selected jet

$$Q_{\text{jet}} = \frac{\sum_i^{N_{\text{tracks}}} q_i \, p_{\text{T}i}^{\kappa}}{\sum_i^{N_{\text{tracks}}} p_{\text{T}i}^{\kappa}}, \tag{7.5}$$

where N_{tracks} is number of tracks associated to the jet, and q_i and $p_{\text{T}i}$ are charge and p_{T} of the track, respectively. Again, the constant $\kappa = 1.1$ is used to optimize the tagging performance.

7.2 Calibration of the Tagging Methods

Tagging methods using the muon cone charge or the jet charge (equations (7.4) or (7.5) respectively) do not work out of the box. First, they have to be calibrated and "translated" into the probability using the real data. To study and calibrate the OST methods, the self-tagging decays $B^{\pm} \to J/\psi K^{\pm}$ can be used. There the flavour of the B-meson at production is provided by the kaon charge in the final state. Events for calibration are taken from the ATLAS 2011 dataset and they fulfil the same data quality criteria as B_s^0 candidates (see section 4.3). Trigger condition requiring two oppositely charged muons within an invariant mass range around the nominal J/ψ mass is applied. The following criteria have to be fulfilled:

- Event contains a pair of oppositely charged combined muons with $p_{\text{T}} > 4$ GeV and $|\eta| < 2.5$, forming a good vertex (χ^2 probability of the fit is at least 0.001) using information provided by the ID.
- Di-muon invariant mass is within the range (2.8 - 3.4) GeV.
- There is an additional hadronic track with $p_{\text{T}} > 1$ GeV and $|\eta| < 2.5$.

---

[11] b-tag weight is the probability that the jet originates from a b quark.

- A triplet of tracks is fitted to a common vertex under the charged kaon mass hypothesis and with di-muon mass constrained to the World average J/ψ mass [57]. χ^2 probability of the $B^\pm$ vertex fit has to be at least 0.001.

The cut $L_{xy} > 0.1$ mm is finally applied to the $B^\pm$ candidates to reduce the prompt component of the combinatorial background. The PV used for the L_{xy} calculation is chosen using the same procedure as for the B_s^0 candidates.

To remove the background component and study only the signal contribution, a sideband subtraction method is used. This method assumes the parameter distributions of the background in the mass signal region can be approximated by the corresponding distributions from the mass sideband regions. The background component is then removed using a mass fit.

Since the momentum resolution of the ID varies depending on pseudo-rapidity, events are separated into five equal regions of $B^\pm$ candidate rapidity[12] within the range (0.0 - 2.5). Then an individual binned extended maximum likelihood fit to the invariant mass is performed in each region. The mass background is modelled by an exponential function to describe combinatorial background and a hyperbolic tangent function to parametrize the low-mass contribution from incorrectly or partially reconstructed B decays. The mass signal is modelled using a Gaussian function. For each rapidity region, the signal mass region is defined as $\mu \pm 2\sigma$, and the sidebands as $(\mu - 5\sigma; \mu - 3\sigma)$ and $(\mu + 3\sigma; \mu + 5\sigma)$, here μ and σ are the mean and width of the Gaussian function, respectively. The $B^\pm$ mass distribution and the fit projection for all rapidity regions are shown in figure 7.1.

Distributions of the muon cone charge and the jet charge for $B^\pm$ signal candidates are shown in figure 7.2.

To find a relation between the charges defined in equations (7.4) and (7.5), and the probability $P(B|Q)$ that a specific event has a signal decay containing a $\bar{b}$-quark, the probabilities $P(Q|B^+)$ and $P(Q|B^-)$ are defined for each of the B^+ and B^- calibration sample, respectively. Probability $P(B|Q)$ to be tagged as containing a $\bar{b}$-quark is then

$$P(B|Q) = \frac{P(Q|B^+)}{P(Q|B^+) + P(Q|B^-)}, \tag{7.6}$$

and containing a b-quark

$$P(\bar{B}|Q) = 1 - P(B|Q). \tag{7.7}$$

---

[12] Rapidity of the particle is defined as $y = \frac{1}{2} \ln \left(\frac{E+p_z}{E-p_z} \right)$, where E is the energy and p_z the longitudinal momentum of the particle.

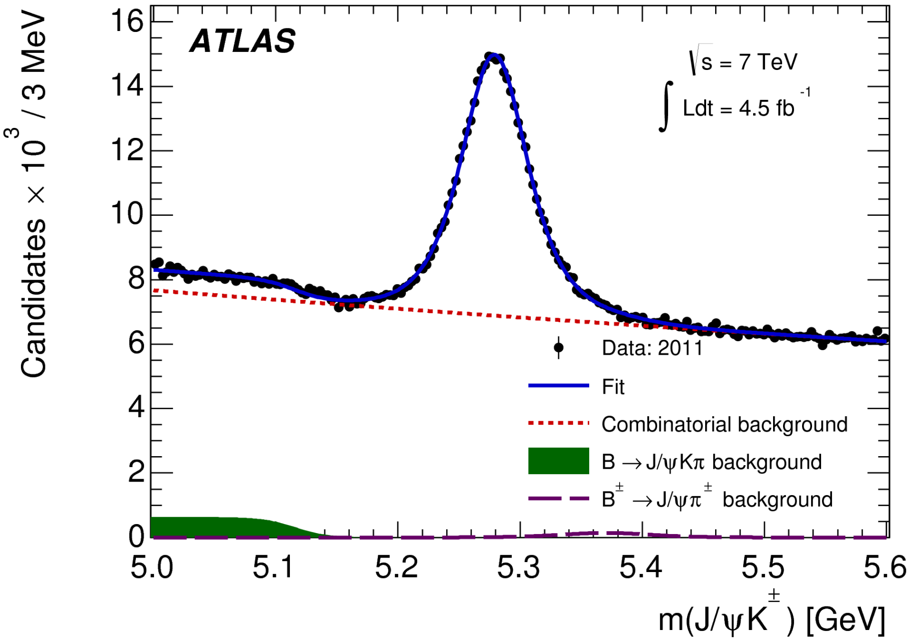

Figure 7.1: The invariant mass distribution for $B^\pm$ candidates used in the calibration of the tagging methods. The data are shown as black points, and the overall result of the fit is given by the blue curve. The combinatorial background component is represented by the red dotted line, partially reconstructed B decays by the green shaded area, and decays of $B^\pm \to J/\psi\pi^\pm$, where a kaon mass was wrongly assigned to the pion, by a purple dashed line.

Using these probabilities, the tagging power (7.3) for the each method can be calculated as $P_{\text{tag}} = \sum_i \epsilon^i_{\text{tag}} \cdot (2\mathcal{P}^i(B|Q_i) - 1)^2$, where the sum is over the bins of the probability distribution as a function of the charge variable and ϵ_i is the tag efficiency calculated in the each bin.

The combination of the tagging methods is applied according to the hierarchy of performance, which is summarized in table 7.1. Based on the tag dilution $\mathcal{D}_{\text{tag}}$, the order is *combined* muon cone charge, *segment tagged* muon cone charge, and jet charge. If it is not possible to tag an event, a probability of 0.5 is assigned.

7.3 Changes in the Likelihood Function

In the tagged analysis, the full version of the differential decay rate is used (equation (2.37) and table 2.4 in section 2.2.5). The Gaussian constraint $\mathcal{P}(\delta_\perp)$ (see equation (6.1)) is no longer needed in the the likelihood function and all strong phases $\delta_\parallel$, $\delta_\perp$, and δ_S are allowed to float freely in the fit. Since the parts with Δm_s are no more cancelled, there are more terms in the fit that contain ϕ_s. However, the $B^0_s - \overline{B^0_s}$ oscillation frequency Δm_s in equation (2.37) cannot be extracted by

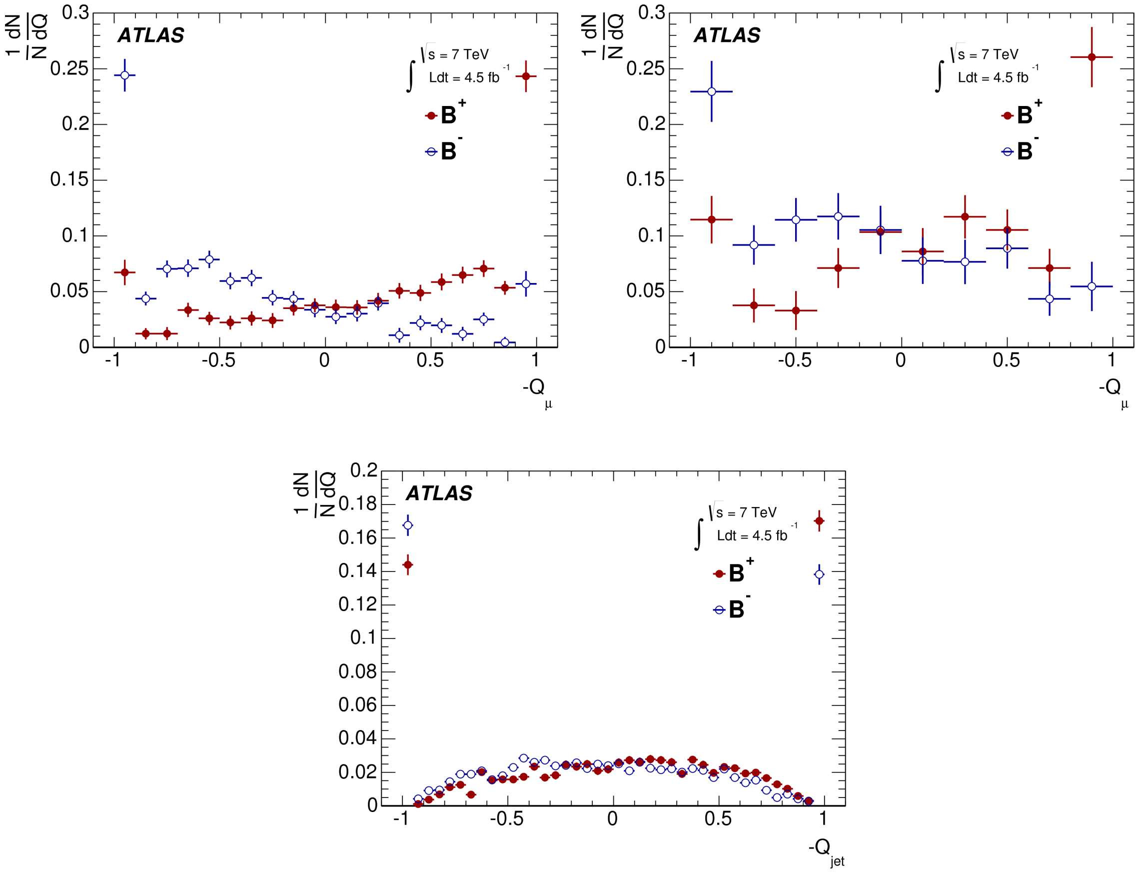

Figure 7.2: The opposite-side muon cone charge distribution Q_μ for combined muons (top left), segment tagged muons (top right), and the jet charge Q_{jet} (bottom) for $B^\pm$ signal candidates.

Tagger	ϵ_{tag} [%]	$\mathcal{D}_{\text{tag}}$ [%]	$\mathcal{P}_{\text{tag}}$ [%]
Combined μ	3.37 ± 0.04	50.6 ± 0.5	0.86 ± 0.04
Segment Tagged μ	1.08 ± 0.02	36.7 ± 0.7	0.15 ± 0.02
Jet Charge	27.7 ± 0.1	12.68 ± 0.06	0.45 ± 0.03
Total	32.1 ± 0.1	21.3 ± 0.08	1.45 ± 0.05

Table 7.1: Summary of tagging performance of used methods together with statistical uncertainties. These are determined by combining the appropriate uncertainties on the individual bins of each charge distribution.

the time-angular fit and thus it has to be fixed to a value measured through other methods. At the start of the analysis, the most precise measurement was done by the CDF experiment $\Delta m_s = 17.77 \pm 0.10$ (stat.) $\pm\, 0.07$ (syst.) ps^{-1} [60].

The tagging enters the fit in a form of probabilities $P(B|Q)$ and $P(\bar{B}|Q)$, as defined in the previous section. They serve as a multiplication factor to the differential decay rate of B_s^0 and $\overline{B_s^0}$, respectively:

$$\mathcal{P}_{\text{sig}}(\Omega_i, P(B|Q), t_i|\sigma_{t_i}) = P(B|Q)\frac{\mathrm{d}^4\Gamma}{\mathrm{d}t\ \mathrm{d}\Omega} + (1 - P(B|Q))\frac{\mathrm{d}^4\bar{\Gamma}}{\mathrm{d}t\ \mathrm{d}\Omega}. \tag{7.8}$$

Since the tag probability is used as a conditional variable, the normalization of $\mathcal{P}_{\text{sig}}(\Omega_i, P(B|Q), t_i|\sigma_{t_i}) \cdot \mathcal{A}_{\text{sig}}(\Omega_i, p_{\text{T}i})$ over the time and transversity angles is performed for each event with respect to the tag probability. Also additional fixed PDFs $\mathcal{P}_{\text{sig}}(P(B|Q))$ and $\mathcal{P}_{\text{bck}}(P(B|Q))$ are included for the tag probability distributions for the signal and background respectively, similarly to section 5.2.4. These functions are describing continuous parts, as well as the discrete parts (spikes), shown in figure 7.3. The spikes have their origin in tagging objects formed from a single track, providing a tag charge of exactly +1 or −1. The fractions f_{+1} and f_{-1} of events tagged with charges of +1 and −1 are derived separately for signal and background. The remaining $(1 - f_{+1} - f_{-1})$ is the fraction of events in the continuous region. These are described by empirically chosen functions: a fourth-order Chebychev polynomial is used for the combined muons and the jet charge, and a third-order polynomial for the segment tagged muons. Both fractions $f_{\pm 1}$ and functions describing the continuous parts are obtained using the sideband subtraction method. Results of the fits to the continuous parts projected onto the data are shown in figure 7.4, where the spikes are removed. The relative fractions of the spikes $f_{\pm 1}$ are given in table 7.2. Table 7.3 then summarizes the relative fractions of tagged events for signal and background for each tagging method.

Tagger	Signal		Background	
	f_{+1}	f_{-1}	f_{+1}	f_{-1}
Combined μ	0.106 ± 0.019	0.187 ± 0.022	0.098 ± 0.006	0.108 ± 0.006
Segment Tag. μ	0.152 ± 0.043	0.153 ± 0.043	0.098 ± 0.009	0.095 ± 0.008
Jet Charge	0.167 ± 0.010	0.164 ± 0.010	0.176 ± 0.003	0.180 ± 0.003

Table 7.2: Relative probabilities between tag charges +1 and −1 for signal and background events for the different tagging methods. Only statistical errors are quoted.

The final signal PDF for the tagged analysis is

$$\begin{aligned}\mathcal{F}_{\text{sig}}(m_i, t_i, P(B|Q), \Omega_i) = {} & \mathcal{P}_{\text{sig}}(m_i|\sigma_{m_i}) \cdot \mathcal{P}_{\text{sig}}(\sigma_{m_i}) \cdot \mathcal{P}_{\text{sig}}(\Omega_i, P(B|Q), t_i|\sigma_{t_i}) \\ & \cdot \mathcal{P}_{\text{sig}}(\sigma_{t_i}) \cdot \mathcal{P}_{\text{sig}}(P(B|Q)) \\ & \cdot \mathcal{A}_{\text{sig}}(\Omega_i, p_{\text{T}i}) \cdot \mathcal{P}_{\text{sig}}(p_{\text{T}i}).\end{aligned} \tag{7.9}$$

The background functions remain unchanged from the untagged analysis and the

Tagger	Signal	Background
Combined μ	0.0372 ± 0.0023	0.0272 ± 0.0005
Segment Tagged μ	0.0111 ± 0.0014	0.0121 ± 0.0003
Jet Charge	0.277 ± 0.007	0.254 ± 0.002
Untagged	0.675 ± 0.011	0.707 ± 0.003

Table 7.3: Relative population of the tagging methods in the background and signal events. Only statistical errors are quoted.

only difference in the background PDF is the $\mathcal{P}_{\text{bck}}(P(B|Q))$ term:

$$\begin{aligned}\mathcal{F}_{\text{bck}}(m_i, t_i, \Omega_i) = {} & \mathcal{P}_{\text{bck}}(m_i) \cdot \mathcal{P}_{\text{bck}}(\sigma_{m_i}) \cdot \mathcal{P}_{\text{bck}}(t_i|\sigma_{t_i}) \cdot \mathcal{P}_{\text{bck}}(\theta_T) \cdot \mathcal{P}_{\text{bck}}(P(B|Q)) \\ & \cdot \mathcal{P}_{\text{bck}}(\psi_T) \cdot \mathcal{P}_{\text{bck}}(\phi_T) \cdot \mathcal{P}_{\text{bck}}(\sigma_{t_i}) \cdot \mathcal{P}_{\text{bck}}(p_{\text{T}i}). \end{aligned} \tag{7.10}$$

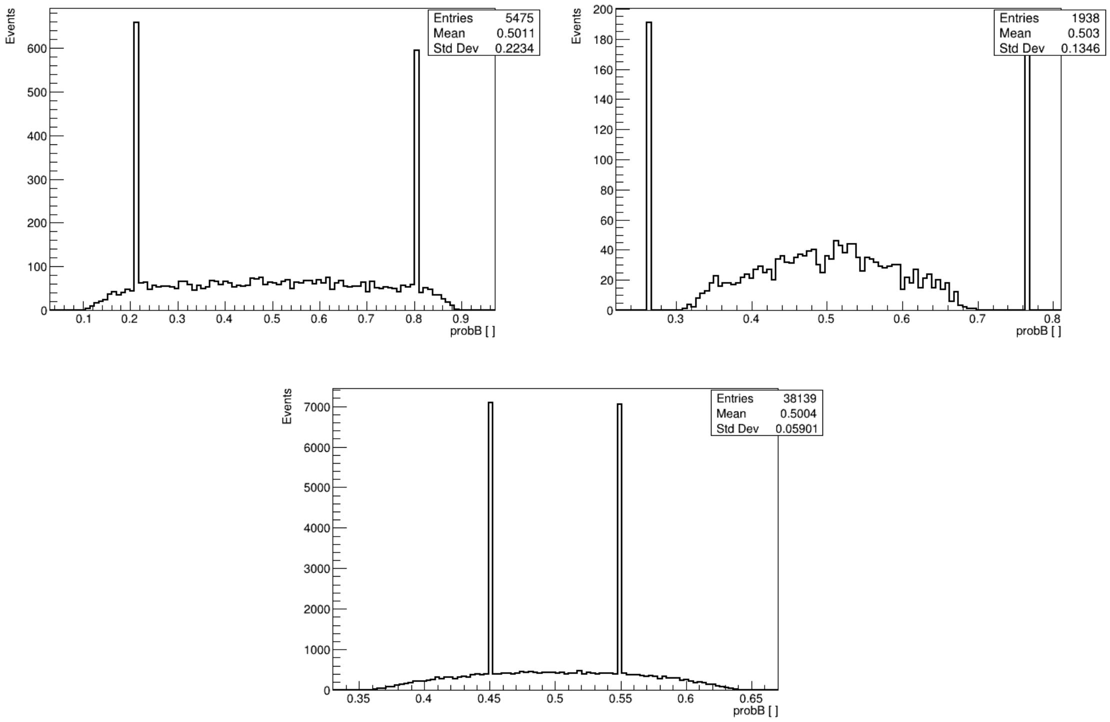

Figure 7.3: The B_s^0-tag probability distribution for the events tagged with combined muons (top left), segment tagged muons (top right), and the jet charge (bottom), before removing spikes.

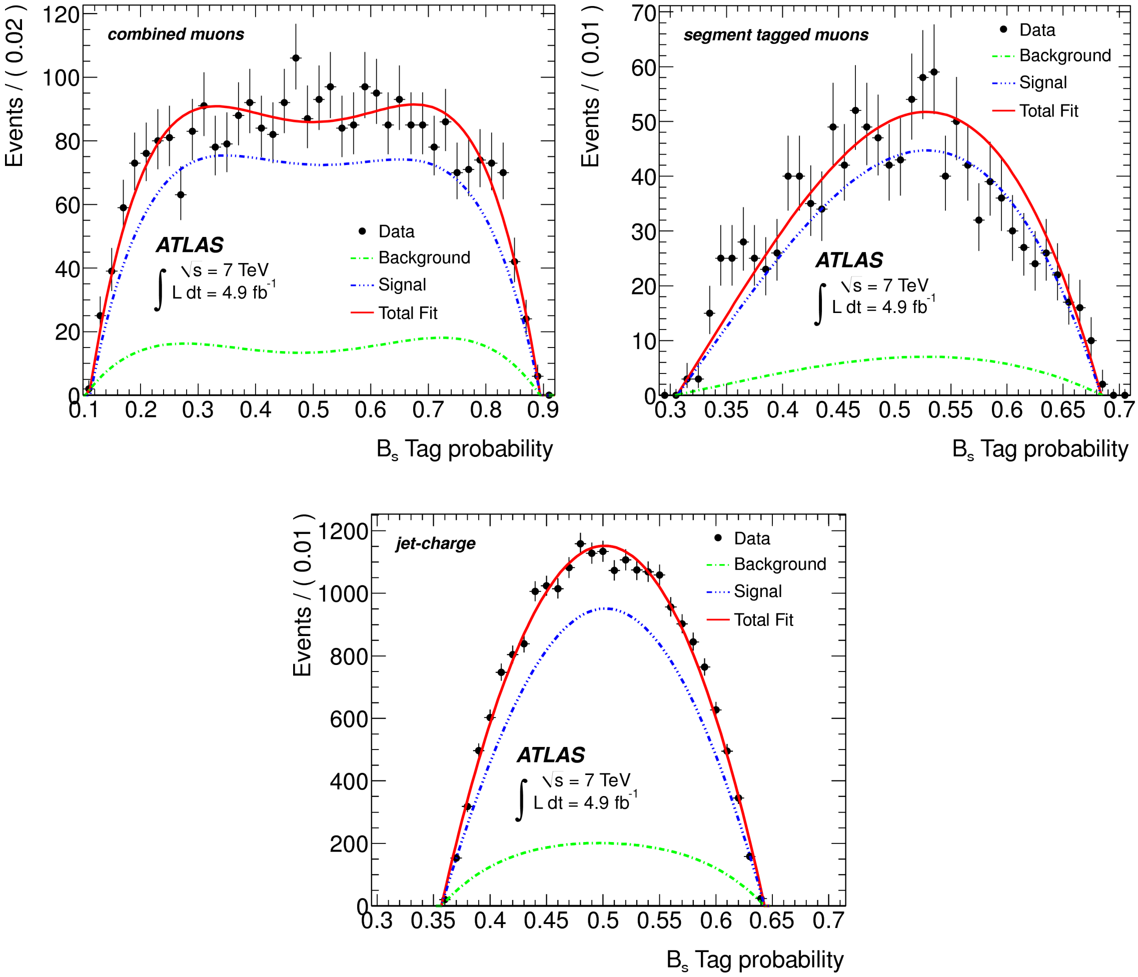

Figure 7.4: The B_s^0-tag probability distribution for the events tagged with combined muons (top left), segment tagged muons (top right), and the jet charge (bottom). Black dots are data after removing spikes, blue is the fit to the sidebands, green to the signal and red is a sum of both fits.

7.4 Results of the Tagged Fit

In the tagged analysis, the likelihood function is no longer symmetric under the transformation (6.4), but the sign of $\Delta\Gamma_s$ still needs to be constrained by the LHCb measurement [61]. Results of the tagged fit to the 7 TeV pp data are summarized in table 7.4, where the physical parameters describing the CP-violation are given together with their statistical and systematic uncertainties. Correlations between the physics parameters are shown in table 7.5. The number of signal B_s^0 meson candidates extracted from the fit is 22670 ± 150.

Despite the fact that only 32.5 % of signal events can be tagged, using the flavour tagging significantly improves the precision of the ϕ_s measurement: from $\phi_s^{\text{untagged}} = 0.22 \pm 0.41$ (stat.) ± 0.10 (syst.) rad to $\phi_s^{\text{tagged}} = 0.12 \pm 0.25$ (stat.) ± 0.05 (syst.) rad.

The updated value is still consistent with theoretical expectations of the Standard Model. This is also presented in figure 7.5, where a likelihood contours in the $\phi_s - \Delta\Gamma_s$ plane for the 68%, 90%, and 95% confidence intervals are shown.

Parameter	Value	Stat. Uncertainty	Syst. Uncertainty
ϕ_s [rad]	0.12	0.25	0.05
$\Delta\Gamma_s$ [ps^{-1}]	0.053	0.021	0.010
Γ_s [ps^{-1}]	0.677	0.007	0.004
$\lvert A_0(0)\rvert^2$	0.529	0.006	0.012
$\lvert A_{\parallel}(0)\rvert^2$	0.220	0.008	0.009
$\lvert A_S(0)\rvert^2$	0.024	0.014	0.028
$\delta_{\perp}$ [rad]	3.89	0.47	0.11
$\delta_{\parallel}$ [rad]	[3.04, 3.23]		0.09
$\delta_{\perp} - \delta_S$ [rad]	[3.02, 3.25]		0.04

Table 7.4: Fitted values for the physics parameters along with their statistical and systematic uncertainties for the 7 TeV data tagged analysis.

	ϕ_s	$\Delta\Gamma_s$	Γ_s	$\lvert A_{\parallel}(0)\rvert^2$	$\lvert A_0(0)\rvert^2$	$\lvert A_S(0)\rvert^2$	$\delta_{\parallel}$	$\delta_{\perp}$	$\delta_{\perp} - \delta_S$
ϕ_s	1.000	0.107	0.026	0.010	0.002	0.029	0.021	-0.043	-0.003
$\Delta\Gamma_s$		1.000	-0.617	0.105	0.103	0.069	0.006	-0.017	0.001
Γ_s			1.000	-0.093	-0.063	0.034	-0.003	0.001	-0.009
$\lvert A_{\parallel}(0)\rvert^2$				1.000	-0.316	0.077	0.008	0.005	-0.010
$\lvert A_0(0)\rvert^2$					1.000	0.283	- 0.003	-0.016	-0.025
$\lvert A_S(0)\rvert^2$						1.000	-0.011	-0.054	-0.098
$\delta_{\parallel}$							1.000	0.038	0.007
$\delta_{\perp}$								1.000	0.081
$\delta_{\perp} - \delta_S$									1.000

Table 7.5: Correlations between the physics parameters obtained from the tagged fit to the 7 TeV data.

Break down of the systematic uncertainties into the individual contributions is given in table 7.7. The same sources of systematic uncertainties as for the untagged analysis are considered and thus each row of table 7.7 is calculated as described in section 6.2.

The only additional uncertainty is arising from the flavour tagging. The *statistical* uncertainty given by the limited size of the $B^{\pm}$ calibration sample is already included in the overall statistical error of the parameters presented in table 7.4: the main B_s^0 fit is repeated 1000 times and each tag probability $P(B|Q)$ is randomly generated according to Gaussian function with a mean equal to the default $P(B|Q)$ extracted in calibration process and a width equal to its statistical uncertainty. The

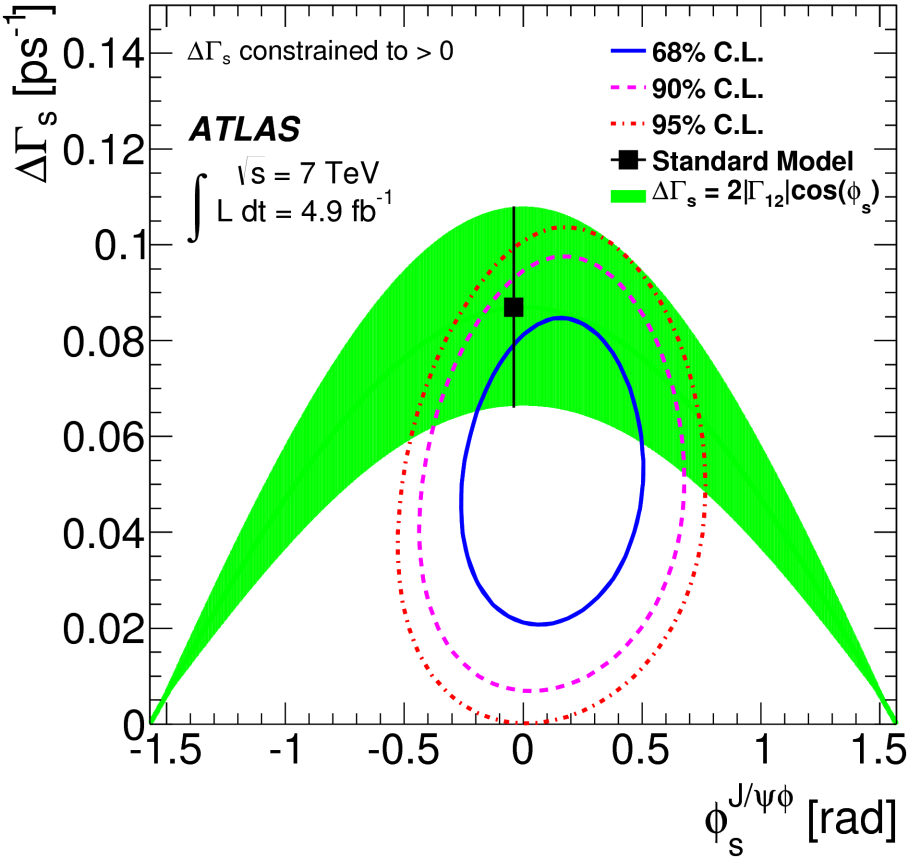

Figure 7.5: Likelihood contours in the $\phi_s - \Delta\Gamma_s$ plane, showing the 68%, 90%, and 95% confidence intervals of the tagged analysis result (using statistical errors only). The green band is the theoretical prediction of mixing-induced CP-violation.

Root Mean Square (RMS) of these distributions are taken as an estimate of the statistical errors due to tagging. These are then added to the statistical errors obtained from the likelihood fit. Except for the ϕ_s and $\delta_\perp$ parameters (given in table 7.6), all contributions are found to be negligible. To account for possible correlations, the combined errors are determined as mean of 1000 statistical errors of the performed fits.

	σ_{Fit} [rad]	σ_{Tag} [rad]	σ_{Total} [rad]
ϕ_s	0.25	0.07	0.25
$\delta_\perp$	0.46	0.13	0.47

Table 7.6: Addition of the flavour tagging uncertainties.

The contribution of flavour tagging to *systematic* uncertainties (table 7.7) is estimated by varying the model parametrizing the probability distribution $P(B|Q)$

as a function of the tag charge. Instead of using a linear function a third-order polynomial is used for the combined muon cone charge tag and the segment tagged muons. For the jet charge tag, a third- and a fifth-order polynomials are tested. The B_s^0 fit is repeated with the alternative models and the largest difference is assigned as the systematic uncertainty.

Pull distributions of the ToyMC pseudo-experiments presented in figure 7.6 show less bias in the likelihood fit for the $\Delta\Gamma_s$ and $\delta_\perp - \delta_S$ parameters compared to the untagged analysis. However, the amplitudes $A_\parallel$, A_0, and A_S are shifted about ~ 0.4 from the centre. Unfortunately the strong phase $\delta_\parallel$ still suffers from a non-Gaussian pulls behaviour. An additional test using a 1D likelihood scan[13] of this parameter does not show any unexpected shape (figure 7.7 middle left). The result is thus again given in the form of a 68% C.L. interval (2.92 - 3.35) rad.

Result for the strong phase δ_S (related to the $\delta_\perp$) is also given in a form of 1σ confidence interval (3.02 - 3.25) rad. The pulls distribution is Gaussian and only slightly shifted, but the 1D likelihood scan is insensitive at the level of 2.1σ, as shown in figure 7.7 bottom. Likelihood scans for other parameters have clear minima and expected shapes.

Systematics	ϕ_s [rad]	$\Delta\Gamma_s$ [ps^{-1}]	Γ_s [ps^{-1}]	$\lvert A_\parallel(0)\rvert^2$	$\lvert A_0(0)\rvert^2$	$\lvert A_S(0)\rvert^2$	$\delta_\perp$ [rad]	$\delta_\parallel$ [rad]	$\delta_\perp - \delta_S$ [rad]
ID Alignment	$< 10^{-2}$	$< 10^{-3}$	$< 10^{-3}$	$< 10^{-3}$	$< 10^{-3}$	-	$< 10^{-2}$	$< 10^{-2}$	-
Trigger Eff.	$< 10^{-2}$	$< 10^{-3}$	0.002	$< 10^{-3}$	$< 10^{-3}$	$< 10^{-3}$	$< 10^{-2}$	$< 10^{-2}$	$< 10^{-2}$
B_d^0 Contrib.	0.03	0.001	$< 10^{-3}$	$< 10^{-3}$	0.005	0.001	0.02	$< 10^{-2}$	$< 10^{-2}$
Tagging	0.03	$< 10^{-3}$	$< 10^{-3}$	$< 10^{-3}$	$< 10^{-3}$	$< 10^{-3}$	0.04	$< 10^{-2}$	$< 10^{-2}$
Acceptance	0.02	0.004	0.002	0.002	0.004	-	-	$< 10^{-2}$	-
Models:									
Default Fit	$< 10^{-2}$	0.003	$< 10^{-3}$	0.001	0.001	0.006	0.07	0.01	0.01
Sig. Mass	$< 10^{-2}$	0.001	$< 10^{-3}$	$< 10^{-3}$	0.001	$< 10^{-3}$	0.03	0.04	0.01
Bck. Mass	$< 10^{-2}$	0.001	0.001	$< 10^{-3}$	$< 10^{-3}$	0.002	0.06	0.02	0.02
Resolution	0.02	$< 10^{-3}$	0.001	0.001	$< 10^{-3}$	0.002	0.04	0.02	0.01
Bck. Time	0.01	0.001	$< 10^{-3}$	0.001	$< 10^{-3}$	0.002	0.01	0.02	0.02
Bck. Angles	0.02	0.008	0.002	0.008	0.009	0.027	0.06	0.07	0.03
Total	0.05	0.010	0.004	0.009	0.012	0.028	0.11	0.09	0.04

Table 7.7: Summary of the tagged analysis systematic uncertainties assigned to parameters of interest. The total uncertainties are calculated as $\sqrt{\sum_i \sigma_i^2}$.

Table 7.8 and figure 7.8 represent updates of table 6.5 and figure 6.10, respectively. Results of $B_s^0 \to J/\psi\phi$ CPV measurements from D0, CDF, LHC*b* (updated measurement), and ATLAS experiments (tagged result), as well as their combined result calculated by HFLAG are shown there. All values are consistent with the SM

---

[13] In the 1D likelihood scan the selected parameter is fixed and the fit is repeated for N equidistant steps in the given parameter range. The value shown on the vertical axis, $-2\Delta \ln \mathcal{L} \equiv -2\left(\ln \mathcal{L}^D - \ln \mathcal{L}^i\right)$, is a difference between the likelihood values of a default fit ($\mathcal{L}^D$) and of the fit in which the given parameter is fixed to a value shown on the horizontal axis ($\mathcal{L}^i$). $-2\Delta \ln \mathcal{L} = 1$ corresponds to the estimated 1σ confidence level.

expectation, but none of them can exclude the possible new physics contributions to the CP-violation in this sector.

	ϕ_s [rad]	$\Delta\Gamma_s[\mathrm{ps}^{-1}]$	Ref.
D0	$-0.55^{+0.38}_{-0.36}$	$0.163^{+0.065}_{-0.064}$	[27]
CDF	$[-0.60, 0.12]$, 68 % CL	$0.068 \pm 0.026 \pm 0.009$	[28]
LHCb	$0.07 \pm 0.09 \pm 0.01$	$0.100 \pm 0.016 \pm 0.003$	[67]
ATLAS	$0.12 \pm 0.25 \pm 0.05$	$0.053 \pm 0.021 \pm 0.010$	[8]
HFLAG	0.00 ± 0.07	0.091 ± 0.010	[68]
SM	$-0.0363^{+0.0016}_{-0.0015}$	0.087 ± 0.021	[24], [64], resp.

Table 7.8: Summarized results of $B^0_s \to J/\psi\phi$ CPV measurements from D0, CDF, LHCb (updated analysis), and ATLAS (tagged analysis) experiments. The first error is due to statistics, the second one to systematics. HFLAG combined result is based also on the LHCb $B^0_s \to J/\psi\pi\pi$ measurement. SM stands for the Standard Model prediction.

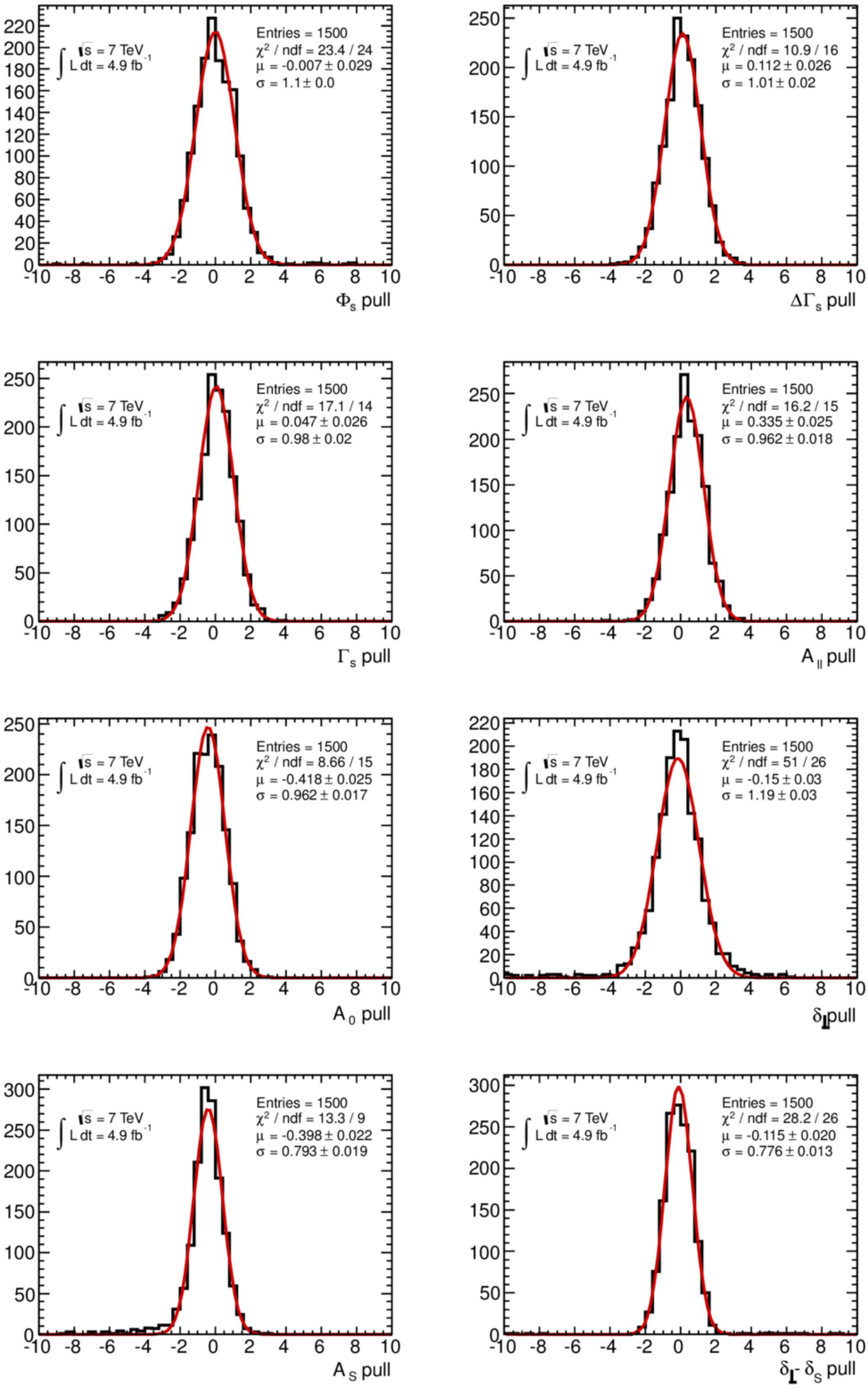

Figure 7.6: Pull distributions of the measured parameters from 1500 pseudo-experiments fitted with a Gaussian function. The results from the real data fit are taken as input values for the generation of pseudo-events.

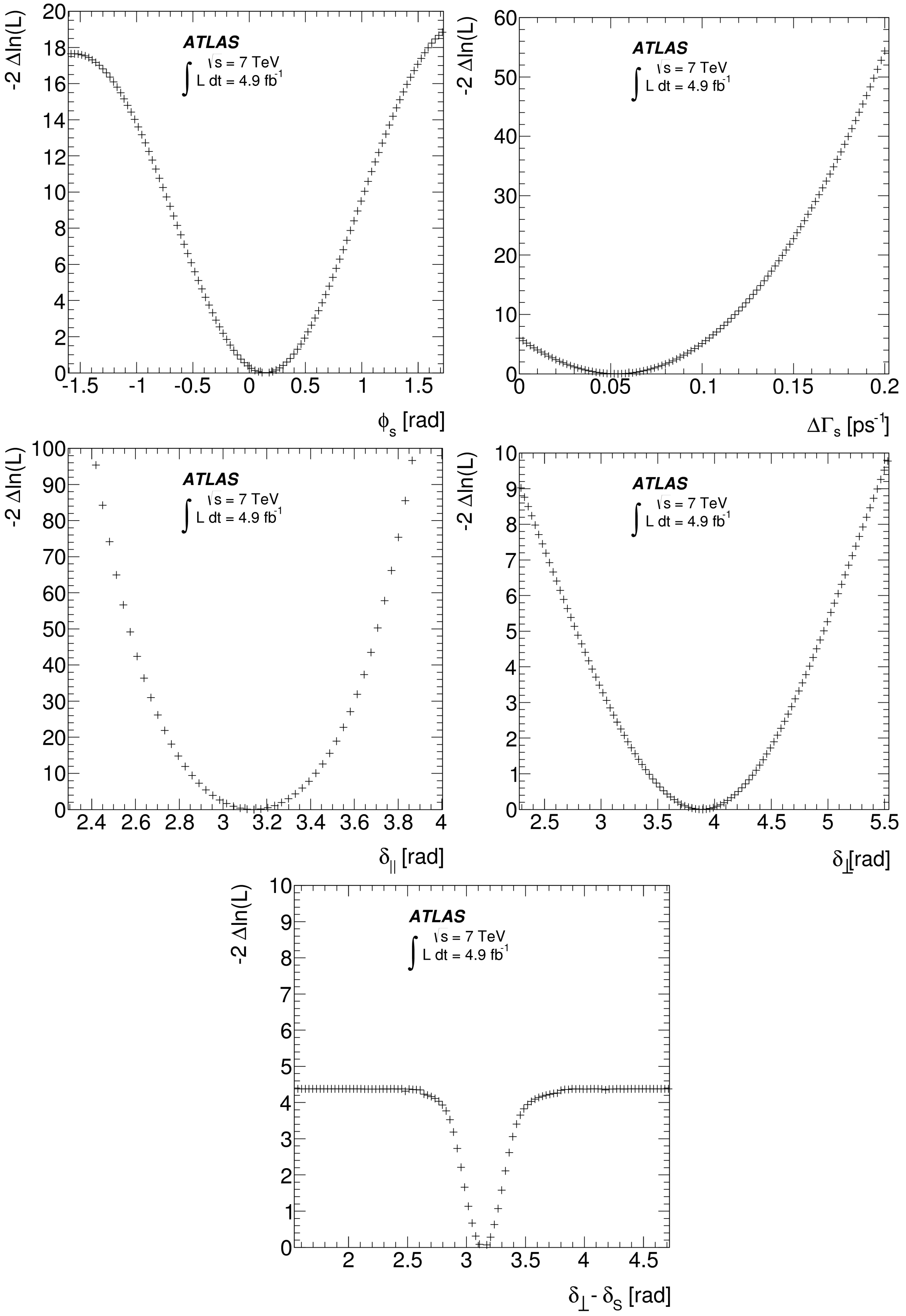

Figure 7.7: 1D likelihood scans for ϕ_s and $\Delta\Gamma_s$ parameters (top left and right, respectively) and for the strong phases $\delta_{\|}$, $\delta_{\perp}$, and $\delta_{\perp} - \delta_S$ (middle left, middle right, and bottom, respectively). The likelihood scan for the $\delta_{\perp} - \delta_S$ parameter shows the insensitivity of the fit at the level of 2.1σ.

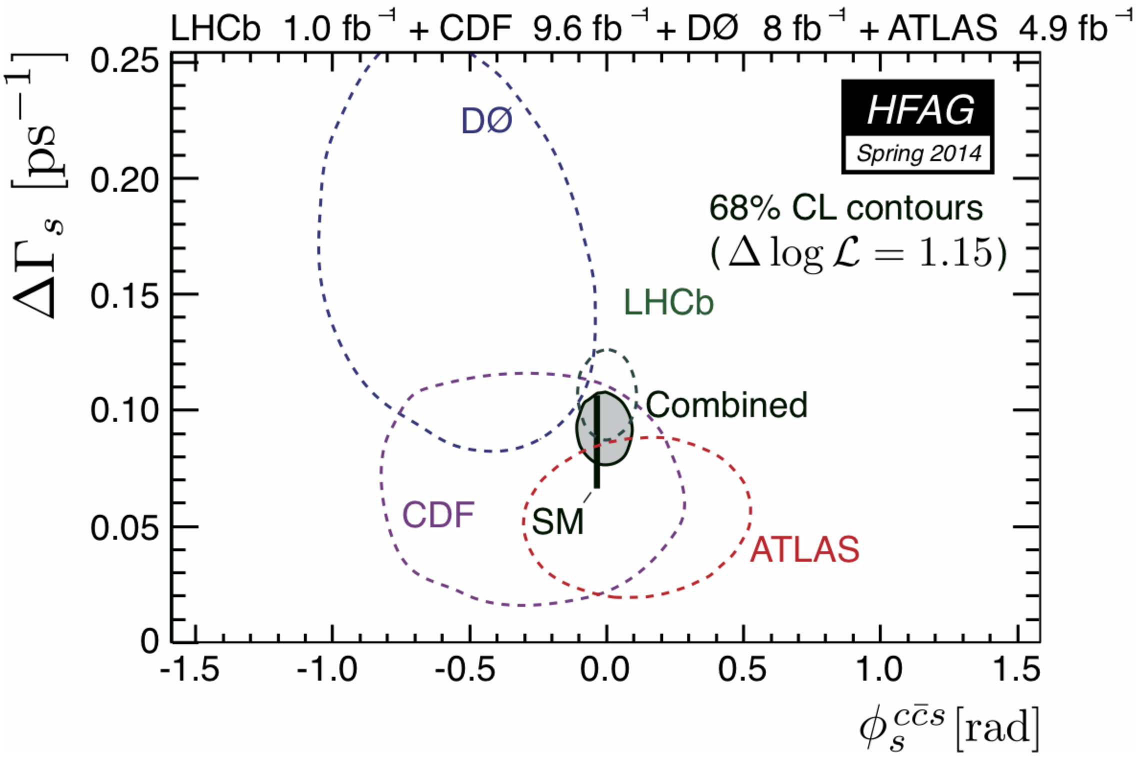

Figure 7.8: 68 % CL regions in B_s^0 width difference $\Delta\Gamma_s$ and weak phase ϕ_s obtained from individual and combined D0, CDF, LHCb, and ATLAS measurements (update of figure 6.10). The SM expectation is shown as the black rectangle. Taken from [68].

Chapter 8

Tagged Analysis of the 8 TeV Data

The results for the most interesting parameters ϕ_s and $\Delta\Gamma_s$, presented in the previous chapter, are still dominated by the statistical uncertainties. Additional 14.3 fb^{-1} from the very successful 8 TeV 2012 data-taking (see chapter 4) are treated separately, as an independent measurement of the same parameters, which is then statistically combined with the tagged analysis of the 7 TeV data into the final Run1 result (presented in chapter 9).

Due to the 3 times larger dataset used, the previous likelihood models (especially for the background) and the fitting code became insufficient. On the other hand, data-driven techniques like flavour tagging calibration are more precise. Moreover, electrons are now included, in addition to final-state muons, for the flavour tagging. Also a whole new fitting framework is written to perform better and faster likelihood parameter estimation and more efficient testing of alternative models, acceptance maps, and other systematics.

The main principles and techniques of the analysis remain unchanged and thus only differences are described in the following section. The same criteria are used for event selection and candidate reconstruction, except for the trigger selection as described in chapter 4.

8.1 Flavour Tagging

Flavour tagging methods described in section 7.1.1 are extended to use also electrons in the event. Similarly to equation (7.4) an *electron cone charge* is defined as

$$Q_e = \frac{\sum_i^{N_{\mathrm{tracks}}} q_i \, p_{\mathrm{T}i}^{\kappa}}{\sum_i^{N_{\mathrm{tracks}}} p_{\mathrm{T}i}^{\kappa}}, \tag{8.1}$$

where N_{tracks} is number of tracks in the cone size $\Delta R = \sqrt{(\Delta\eta)^2 + (\Delta\phi)^2} < 0.5$ around the leading electron, and q_i and $p_{\text{T}i}$ are charge and p_{T} of the track, respectively. The constant $\kappa = 1.0$ is found empirically to achieve the best tagging performance.

An electron is identified using information from the ID and the calorimeter. It is required to have $p_{\text{T}} > 500$ MeV, $|\eta| < 2.5$, and the impact parameter from the PV $|\Delta z| < 5$ mm. Electrons from the cone $\Delta R < 0.4$ around the B_s^0 candidate momenta are rejected as well as electrons having an opening angle ζ between their momenta and the B_s^0 candidate momenta in range of $\cos\zeta > 0.98$. In the case of more than one electron passing the selection, the electron with the highest transverse momentum is chosen.

Tagging methods for the 8 TeV data analysis are calibrated using the $B^\pm \to J/\psi K^\pm$ events from the full 2012 data sample, satisfying the criteria described in section 7.2. The trigger problem described in section 4.1 does not affect the flavour tagging calibration and thus all 19.5 fb^{-1} of 8 TeV pp data from 2012 are used. Distributions of the cone charges for combined muons, segment tagged muons, and electrons as well as the jet charge are shown in figure 8.1.

Tagger	ϵ_{tag} [%]	$\mathcal{D}_{\text{tag}}$ [%]	$\mathcal{P}_{\text{tag}}$ [%]
Combined μ	4.12 ± 0.02	47.4 ± 0.2	0.92 ± 0.02
Segment Tagged μ	1.20 ± 0.01	28.6 ± 0.2	0.10 ± 0.01
Electron	1.19 ± 0.01	49.2 ± 0.3	0.29 ± 0.01
Jet Charge	13.15 ± 0.03	11.85 ± 0.03	0.19 ± 0.01
Total	19.66 ± 0.04	27.56 ± 0.06	1.49 ± 0.02

Table 8.1: Summary of the tagging performance in the 2012 data. Only statistical uncertainties are given. These are determined by combining the appropriate uncertainties on the individual bins of each charge distribution.

Performance of the individual tagging methods is given in table 8.1. As may be seen by comparing it with table 7.1, the jet charge tagger became less efficient. However, dilutions for all methods remain nearly the same and thus, due to the newly added electron tagger, the overall tagging performance is more efficient and more precise comparing to 2011 data.

Table 8.2 gives the relative fractions “spikes” (events with tag charges +1 and −1) in the 2012 data. Fractions are similar to those in the tagged analysis of 2011 data except for the jet charge – there is a $\sim 50\%$ drop, i.e. more events are spread into the continuous parts of the jet charge probability distribution.

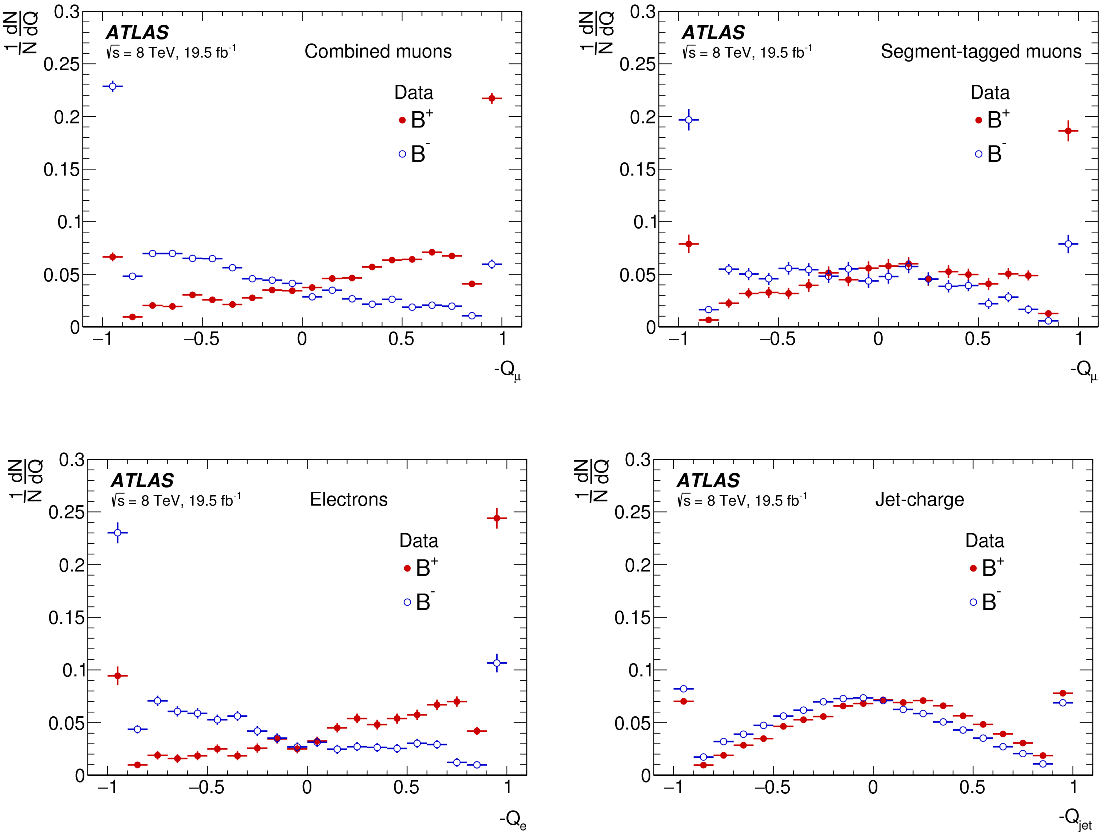

Figure 8.1: The cone charge distributions for combined muons (top left), segment tagged muons (top right), electrons (bottom left), and the jet charge (bottom right) for $B^{\pm}$ signal candidates.

Tagger	Signal		Background	
	f_{+1}	f_{-1}	f_{+1}	f_{-1}
Combined μ	0.124 ± 0.012	0.127 ± 0.012	0.093 ± 0.003	0.095 ± 0.003
Seg. Tag. μ	0.147 ± 0.024	0.118 ± 0.023	0.083 ± 0.004	0.084 ± 0.004
Electron	0.105 ± 0.020	0.139 ± 0.021	0.110 ± 0.007	0.110 ± 0.007
Jet Charge	0.071 ± 0.005	0.069 ± 0.005	0.068 ± 0.002	0.069 ± 0.002

Table 8.2: Relative probabilities between tag charges $+1$ and -1 for signal and background events for the different tagging methods in the 2012 data. Only statistical errors are quoted.

Since the continuous parts are absolutely different from the previous analysis, new function have to be found to describe the probability distributions. A sum of a fourth-order polynomial and two exponential functions is used to describe the combined muon tagging probability. A sum of three Gaussian functions is used for the segment tagged muons. A second-order polynomial together with two exponential functions are applied for the electron tagging method. For the jet charge tagging an eighth-order polynomial is used. Projections of the sideband subtraction fits for all four taggers are shown in figure 8.2.

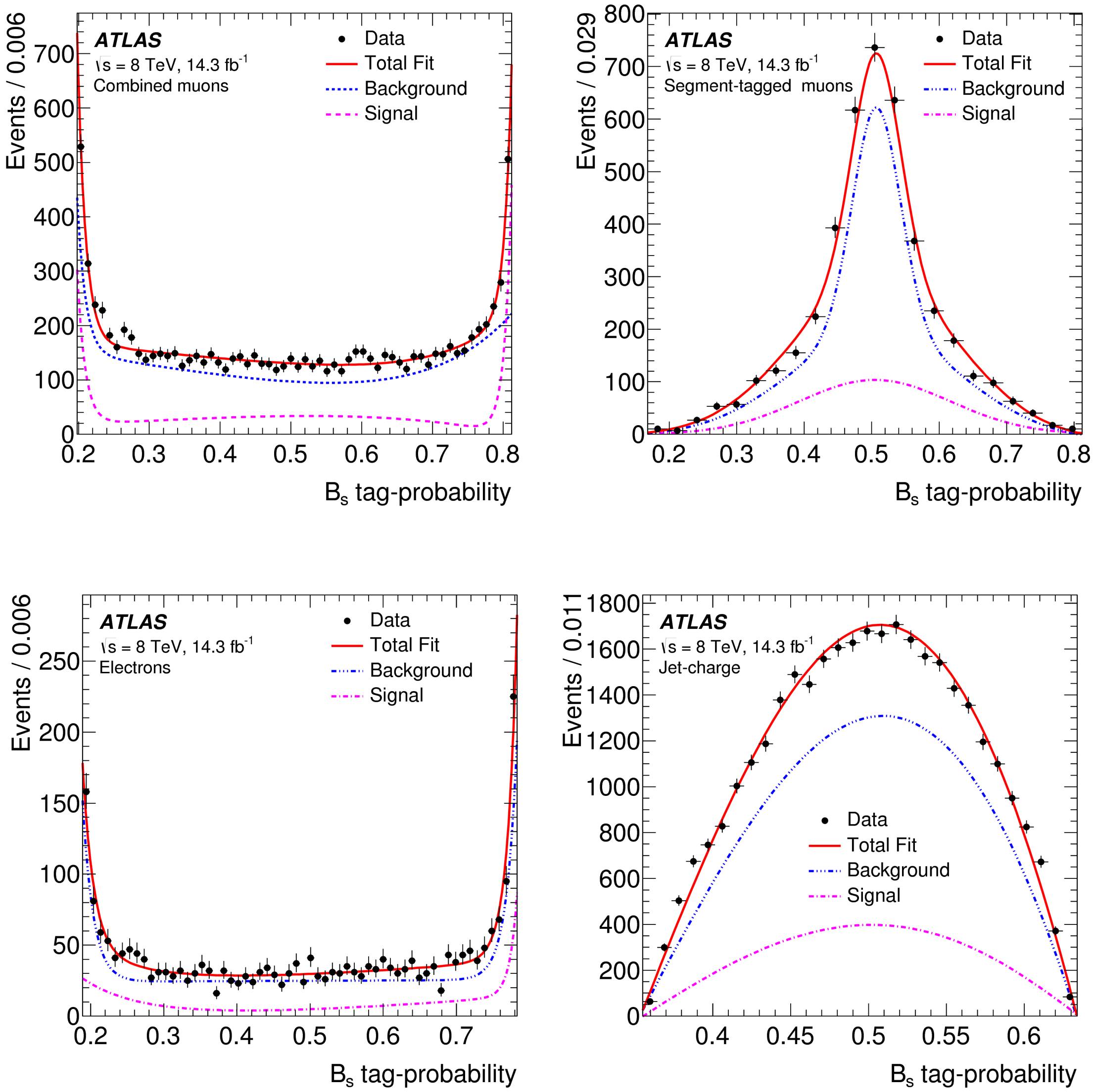

Figure 8.2: Distributions of the B_s^0-tag probability in the 2012 data for the combined muons (top left), segment tagged muons (top right), electrons (bottom left), and the jet charge (bottom right). Black dots are data after removing spikes, blue is the fit to the mass sidebands, purple to the signal and red is a sum of both fits.

As can be seen in table 8.3, the overall tagging efficiency is $\sim 21\%$, which is significant drop from $\sim 32.5\%$ in the tagged 2011 analysis. However, due to the larger data sample, the absolute value of tagged events is $\sim 2\times$ higher.

Tagger	Signal	Background
Combined μ	0.047 ± 0.003	0.038 ± 0.001
Segment Tagged μ	0.013 ± 0.001	0.015 ± 0.001
Electron	0.012 ± 0.001	0.008 ± 0.001
Jet Charge	0.135 ± 0.003	0.100 ± 0.001
Untagged	0.793 ± 0.002	0.839 ± 0.002

Table 8.3: Summary of the relative fractions of the tagging methods in the background and signal events. Only statistical errors are quoted.

8.2 Fitting Model

The general structure of the likelihood function (equations (5.8), (7.9), and (7.10)) is unchanged from the tagged analysis of 2011 data; however, during the paper reviewing process authors were asked to include also dedicated background for the mis-reconstructed $\Lambda_b \to J/\psi p K^-$ decays, similar to specific B_d^0 background, described in section 6.2.2. The likelihood function then turns into

$$\begin{aligned}\ln \mathcal{L} = &\sum_{i=1}^{N} \Big\{ w_i \cdot \ln \Big(f_{\mathrm{sig}} \cdot \mathcal{F}_{\mathrm{sig}}(m_i, t_i, \sigma_t, \Omega_i, P(B|Q), p_{\mathrm{T}i}) \\ &+ f_{\mathrm{sig}} \cdot f_{B_d^0} \cdot \mathcal{F}_{B_d^0}(m_i, t_i, \sigma_t, \Omega_i, P(B|Q), p_{\mathrm{T}i}) \\ &+ f_{\mathrm{sig}} \cdot f_{\Lambda_b} \cdot \mathcal{F}_{\Lambda_b}(m_i, t_i, \sigma_t, \Omega_i, P(B|Q), p_{\mathrm{T}i}) \\ &+ (1 - f_{\mathrm{sig}}(1 + f_{B_d^0} + f_{\Lambda_b})) \cdot \mathcal{F}_{\mathrm{bck}}(m_i, t_i, \sigma_t, \Omega_i, P(B|Q), p_{\mathrm{T}i}) \Big) \Big\}, \end{aligned} \tag{8.2}$$

where $\mathcal{F}_{\Lambda_b}(m_i, t_i, \sigma_t, \Omega_i, P(B|Q), p_{\mathrm{T}i})$ is the PDF describing the Λ_b background and f_{Λ_b} is the relevant fraction.

Also some individual models (PDFs) need to be altered to better describe the observed data. Updated PDFs used in the 2012 analysis as well as the specific Λ_b background are described in the following paragraphs.

Signal Mass Model Despite the fact that the unbinned maximum likelihood fit has nothing to do with the graphical representation of the data, the previously used single Gaussian function smeared with an event-by-event mass resolution σ_{m_i} (equation (5.10)) underestimated the signal mass peak when projected onto the plotted data. Since the problem cannot be tracked to any possible bug in the fitting/plotting code, a sum of three Gaussian function with a common mean is used instead and the effect on the result is evaluated as a systematic uncertainty.

Background Mass Model An exponential function with an added constant term is used to describe the combinatorial background, instead of the linear function used in 2011 data analysis.

Background Angular Distribution The shape of this distribution is found empirically. Equations (5.14) are replaced by Legendre polynomial functions defined as

$$\begin{aligned}
Y_l^m(\theta_T) &= \sqrt{(2l+1)/(4\pi)}\sqrt{(l-m)!/(l+m)!}P_l^{|m|}(\cos\theta_T) \\
P_k(x) &= \frac{1}{2^k k!}\frac{\mathrm{d^k}}{\mathrm{dx^k}}(x^2-1)^k \qquad (8.3)\\
\mathcal{P}_{\mathrm{bck}}(\Omega) &= \sum_{k=0}^{6}\sum_{l=0}^{6}\sum_{m=-l}^{l}\begin{cases} a_{k,l,m}\sqrt{2}Y_l^m(\theta_T)\cos(m\phi_T)P_k(\cos\psi_T), & m>0 \\ a_{k,l,m}\sqrt{2}Y_l^{-m}(\theta_T)\sin(m\phi_T)P_k(\cos\psi_T), & m<0 \\ a_{k,l,m}\sqrt{2}Y_l^0(\theta_T)P_k(\cos\psi_T), & m=0 \end{cases}
\end{aligned}$$

where $\Omega = (\theta_T, \psi_T, \phi_T)$ and the coefficients $a_{k,l,m}$ are adjusted to give the best fit to the angular distributions for events in the B_s^0 mass sidebands in four $p_{\mathrm{T}}(B_s^0)$ intervals (0 - 13) GeV, (13 - 18) GeV, (18 - 25) GeV, and > 25 GeV. Obtained parameters are then fixed in the main fit.

Specific B_d^0 Background The 3D angular distribution of the specific background $B_d^0 \to J/\psi(\mu^+\mu^-)K^{0*}(K^\pm\pi^\mp)$ has again the same form as the general background (Legendre polynomial functions (8.4)), but uses a different set of parameters and higher order of the polynomials (10 instead of 6). The fraction of the B_d^0 contamination is updated to be $f_{B_d^0} = (3.3 \pm 0.5)\%$.

Specific Λ_b Background Contamination from $\Lambda_b \to J/\psi p K^-$ events mis-reconstructed as $B_s^0 \to J/\psi\phi$ (by assigning wrongly a $K^\pm$ mass to a proton) is evaluated using the MC sample generated with the flat angular distribution, which is then sculpted for detector acceptance effects and modelled by Legendre polynomial functions (8.4), as described above. A mass model is obtained by smoothing the invariant mass histogram from MC events and lifetime is described by an exponential term. The fraction of these events $f_{\Lambda_b} = (1.8 \pm 0.6)\%$ is calculated using production and branching fractions from [69, 70]. All PDFs as well as the fraction of Λ_b events are then fixed in the main likelihood fit.

Muon Trigger Efficiency Also in the 2012 data the muon trigger biases the transverse impact parameter d_0 of muons and thus it affect the measured B_s^0 lifetime. The inefficiency is measured using MC sample, by comparing the B_s^0 proper decay time distribution of an unbiased sample with the distribution obtained using the trigger selection. The function found to describe the observed shape has a form

$$w_i = p_0 \cdot \left[1 - p_1 \cdot \left(\mathrm{Erf}\left(\frac{t_i - p_3}{p_2}\right) + 1\right)\right], \tag{8.4}$$

where p_0, p_1, p_2, and p_3 are parameters determined in the fit to MC events as shown in figure 8.3.

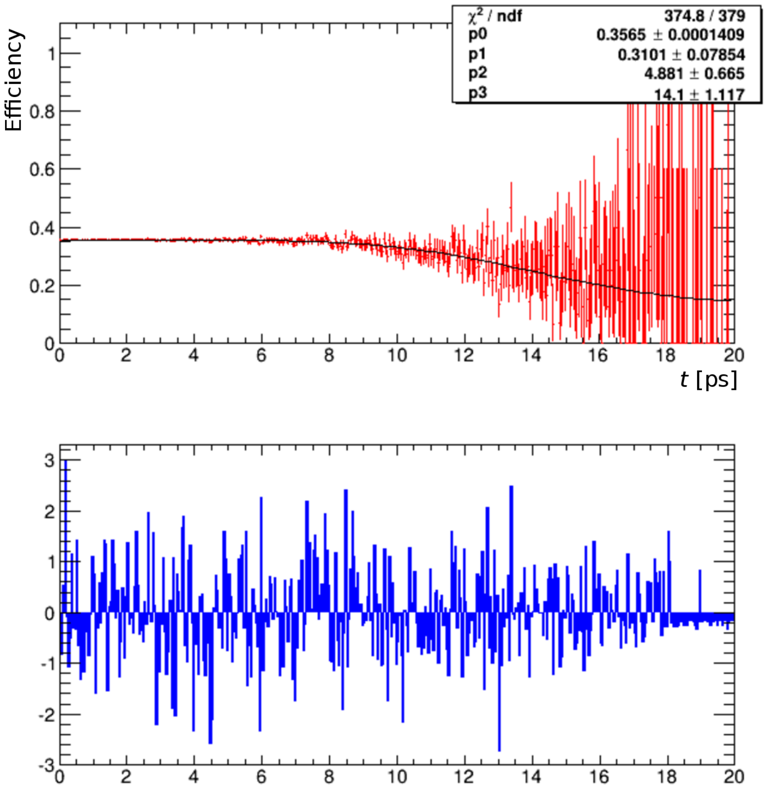

Figure 8.3: Time-dependent inefficiency caused by the muon triggers in the 2012 data-taking (fit to the MC events using the function (8.4)). Used triggers are listed in table 4.1. The pull distribution at the bottom shows the difference between the MC data and fit value normalized to the MC data uncertainty.

8.3 Results of the Fit

Physical parameters describing the CP-violation in the $B_s^0 \to J/\psi\phi$ decay obtained from the tagged fit to 14.3 fb^{-1} of 8 TeV pp data recorded by the ATLAS experiment in 2012 are shown in table 8.4. Break down of systematic uncertainties is presented in the next section. The sign of $\Delta\Gamma_s$ is constrained to be positive, as measured by the LHCb experiment [61]. The number of signal B_s^0 meson candidates extracted from the fit is 74900 ± 400.

Fit projections of the mass and proper decay time, proper decay time uncertainty, and angles (in the mass signal region) are shown in figures 8.4, 8.5, and 8.6 respectively. Table 8.5 shows the correlations between the physics parameters. Only the Γ_s and $\Delta\Gamma_s$ parameters are slightly correlated as expected.

Results and the statistical combination with the analysis of the the 2011 7 TeV data are discussed in the next chapter

Parameter	Value	Stat. Uncertainty	Syst. Uncertainty
ϕ_s [rad]	-0.110	0.082	0.042
$\Delta\Gamma_s$ [ps^{-1}]	0.101	0.013	0.007
Γ_s [ps^{-1}]	0.676	0.004	0.004
$\|A_0(0)\|^2$	0.520	0.004	0.007
$\|A_\parallel(0)\|^2$	0.230	0.005	0.006
$\|A_S(0)\|^2$	0.097	0.008	0.022
$\delta_\perp$ [rad]	4.50	0.45	0.30
$\delta_\parallel$ [rad]	3.15	0.10	0.05
$\delta_\perp - \delta_S$ [rad]	-0.08	0.03	0.01

Table 8.4: Values for the physics parameters along with their statistical and systematic uncertainties obtained from the tagged analysis of the 8 TeV data.

	ϕ_s	$\Delta\Gamma_s$	Γ_s	$\|A_\parallel(0)\|^2$	$\|A_0(0)\|^2$	$\|A_S(0)\|^2$	$\delta_\parallel$	$\delta_\perp$	$\delta_\perp - \delta_S$
ϕ_s	1.000	0.097	-0.085	0.030	0.029	0.048	0.067	0.035	-0.008
$\Delta\Gamma_s$		1.000	-0.414	0.098	0.136	0.045	0.009	0.008	-0.011
Γ_s			1.000	-0.119	-0.042	0.167	-0.027	-0.009	0.018
$\|A_\parallel(0)\|^2$				1.000	-0.330	0.072	0.105	0.025	-0.018
$\|A_0(0)\|^2$					1.000	0.234	-0.011	0.007	0.014
$\|A_S(0)\|^2$						1.000	-0.046	0.004	0.052
$\delta_\parallel$							1.000	0.158	-0.006
$\delta_\perp$								1.000	0.018
$\delta_\perp - \delta_S$									1.000

Table 8.5: Correlations between the physics parameters obtained from the tagged fit to the 8 TeV data.

8.3.1 Systematic Uncertainties

Similarly to the previous measurement, some aspects of the analysis cannot be included into the likelihood fit and have to be evaluated separately as well as the assumptions and simplifications of the models describing the $B_s^0 \to J/\psi\phi$ decay. Systematic uncertainties are calculated for each category listed below and they are

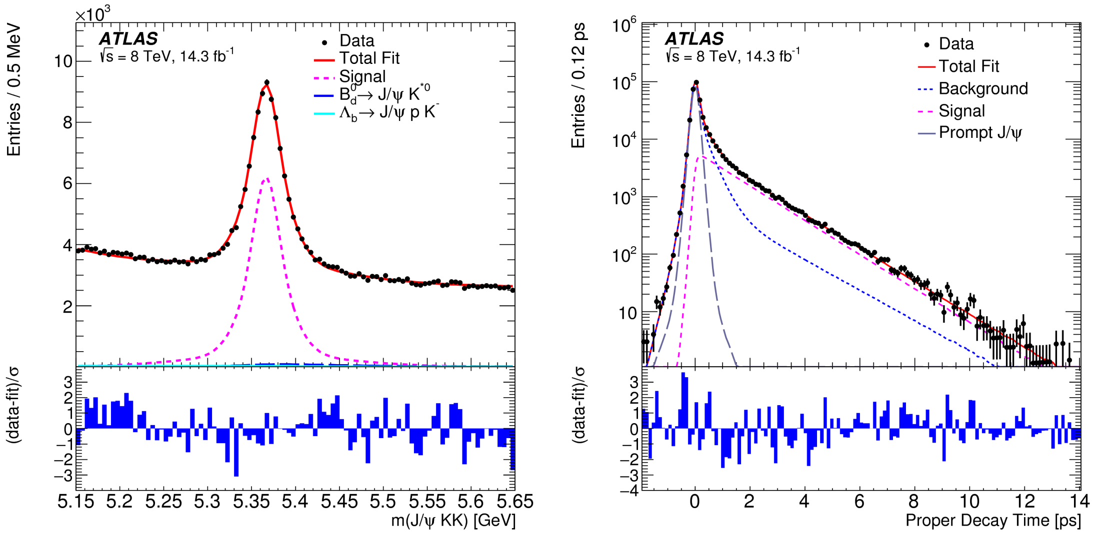

Figure 8.4: Projections of the tagged fit to the 2012 data (black points). (Left) Mass fit projection. The red line shows the total fit, the dashed purple line shows the signal component, the long-dashed dark blue line shows the $B_d^0 \to J/\psi K^{0*}$ component, while the solid light blue line shows the contribution from $\Lambda_b \to J/\psi p K^-$ events. (Right) Proper decay time fit projection. The red line shows the total fit while the purple dashed line shows the total signal. The total background is shown as a blue dashed line with a long-dashed grey line showing the prompt J/ψ background. The pull distribution at the bottom shows the difference between the data and the fit value normalized to the data uncertainty.

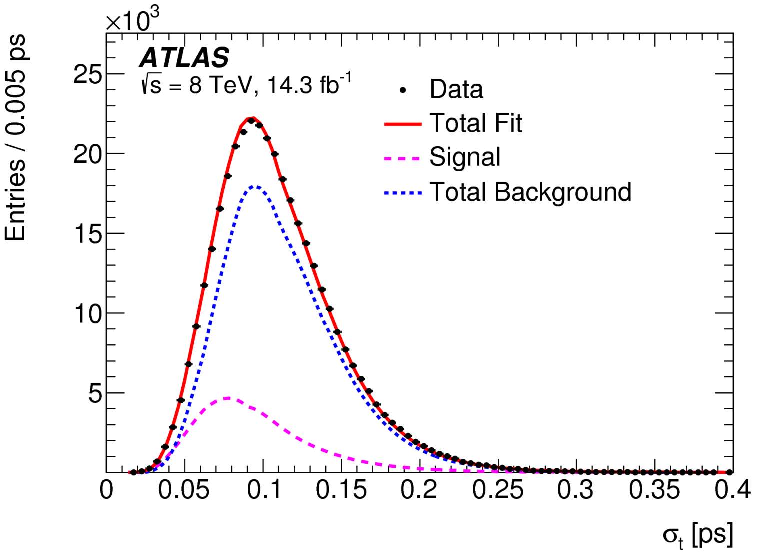

Figure 8.5: Proper decay time uncertainty distributions for the 8 TeV data (black points) together with the fit projections for the background component (dotted blue), the signal component (dashed purple), and the sum of the two fits (red line).

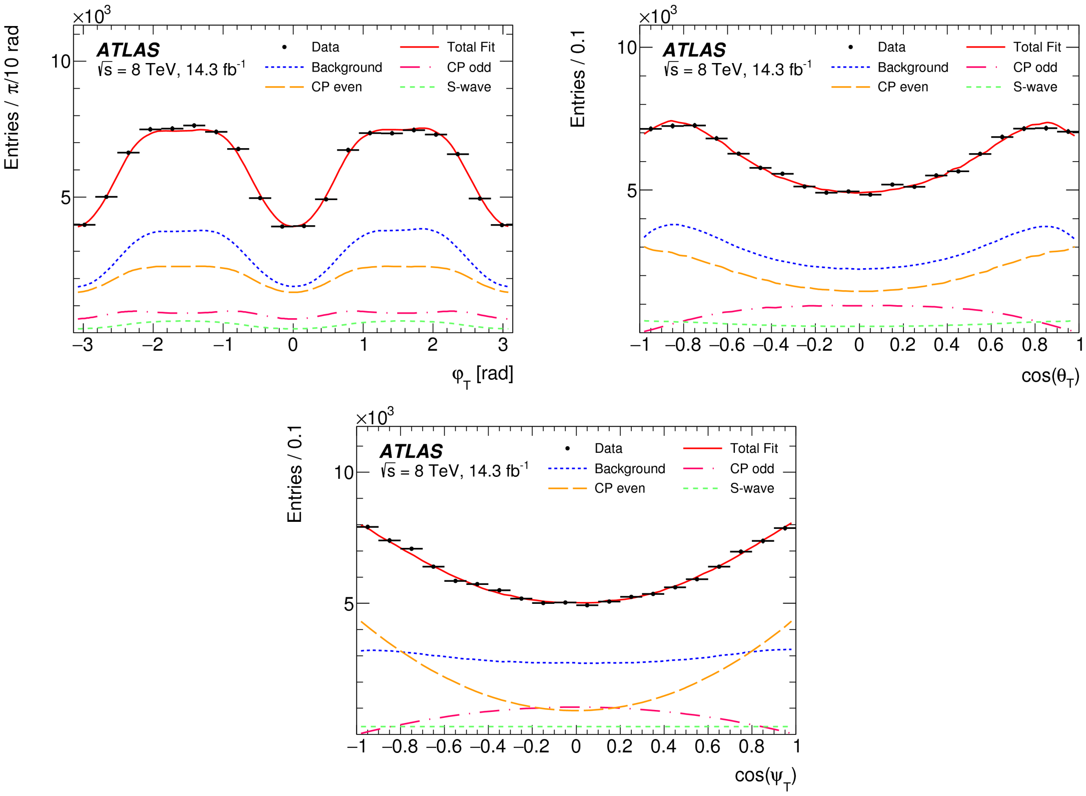

Figure 8.6: Fit projections for transversity angles ϕ_T (left top), $\cos\theta_T$ (top right), and $\cos\psi_T$ (bottom) for events with B_s^0 mass from signal region (5.317-5.417) GeV. The red solid line shows the total fit, the CP-odd and CP-even signal components are shown by the red dot-dashed and orange dashed lines respectively, the S-wave component is given by the green dashed line, and the blue dotted line shows the background contribution.

added in quadratures resulting in a total systematic uncertainty for each physics variable as shown in table 8.6.

ID Alignment Precision of the lifetime measurement depends on the quality of the track reconstruction. Residual misalignments of the ID, which can affect the impact parameter of tracks, are estimated using the real data taken in 2012. After multiple alignment corrections the remaining biases of the momentum-scale were associated with a radial deformation. The estimated radial offset is about 1.6 mm over the full radius of the ID. The radial expansion uncertainties are found to be 0.14 % in the barrel region and 0.55 % in the end-cap regions. Likelihood fit is repeated using the measured lifetime multiplied by values 1.0014 and 0.0055 respectively and compared with the default fit. The larger difference is quoted as the systematic uncertainty.

Angular Acceptance Maps The angular acceptance is calculated from a binned fit to MC events. Possible dependences of the results on the choice of the p_{T}-

binning are tested by varying bin widths and central values. Also an alternative binning in the numerical integration is tested.

Trigger Efficiency The parameters p_0, p_1, p_2, and p_3 describing the lifetime bias are shifted by their uncertainties and the fit is repeated. Fit result is consistent with a default one and thus this systematics is found to be negligible.

Default Fit Model Even if the used model perfectly describes the observed data, its complexity could potentially lead to a bias in the measured physics parameters. To test the possible bias and to estimate the systematic uncertainties a set of ~ 2500 pseudo-experiments is generated and analysed using the pulls method described in section 6.2.5. These tests show no significant bias in the fit model as can be seen in figure 8.7.

Fit Model Variations To estimate the systematic uncertainties due to the fit model, variations of the model are tested in the ToyMC pseudo-experiments. A set of ~ 2500 pseudo-experiments is generated for each variation considered and the uncertainty is estimated using the pulls method described in section 6.2.5. Considered variations are:

- The **signal mass** is generated using the fitted B_s^0 mass convolved with a Gaussian function using the measured per-candidate mass errors (i.e. the default model in the previous analysis).
- The **background mass** is generated from an exponential function with the addition of a first-degree polynomial function instead of an exponential function plus a constant term.
- The **time resolution** model is varied by using two different scale factors to generate the lifetime uncertainty, instead of the single scale factor used in the default model. Scale factors are obtained from the unbinned maximum likelihood to the MC events.

To determine the possible systematics effects of mis-modelling of the background events by the fitted **background mass** model, as seen in figure 8.4 (left) in the low mass sideband region (5.15 - 5.21) GeV, alternative mass selection cuts are used with the default fit model. The effect on the fit results is found to be negligible as shown in figure 8.8.

The alternative model for the non-prompt J/ψ **background lifetimes** using three *positive* exponential functions (instead of two positive exponentials in the default fit) over-parametrizes the fit and thus it cannot be used to obtain parameters for the ToyMC pseudo-experiments from the real data. The effect of the **time background** model is thus estimated from the several fits to the real data using the time background model with three positive exponential functions, but with one relative fraction fixed to certain value from the interval (0 - 1). The effect is also found to be negligible as shown in figure 8.9.

Flavour Tagging The *statistical* uncertainty due to the limited size of the $B^{\pm} \to J/\psi K^{\pm}$ decays is already included in the overall statistical error. Each bin in the 2D histogram of the tag probability and the tagging (μ, electron, b-jet) charge is smeared using a Gaussian function with a mean equal to the central value and a width equal to the uncertainty of the given bin. The histogram is refitted and the new parametrization is used to update the per-candidate tagging probability in the B_s^0 sample and the main fit is performed. The difference to the default fit result is assigned as the statistical uncertainty due to the tagging.

The *systematic* uncertainty arising from the precision of the tagging calibration is estimated by changing the model used to parametrize the probability distribution $P(B|Q)$ as a function of tagging charge from the third-order polynomial function used by default to one of several alternative functions (linear, fifth-order polynomial, two third-order polynomials). The main B_s^0 fit is repeated using the alternative models and the largest difference is assigned as the systematic uncertainty.

Background Angular Model – Choice of p_{T} Bins The shape of the background angular distribution $\Omega = (\theta_T, \psi_T, \phi_T)$ is sensitive to the p_{T} of the B_s^0 meson candidate. The parametrization using the Legendre polynomial functions (8.4) is thus performed in four p_{T} intervals. The systematic uncertainties are estimated by repeating the fit with the different p_{T} intervals and the larger deviation from the default fit result is taken to represent the systematic uncertainties.

Background Angular Model – Choice of Mass Sidebands The parameters of the Legendre polynomial functions (equation (8.4)) are obtained from the fit to the angular distributions in the B_s^0 mass sidebands defined as $|(m(B_s^0) - 5.366| > 0.110$ GeV. The two alternatives are tested in the fit ($|(m(B_s^0) - 5.366| > 0.085$ GeV and $|(m(B_s^0) - 5.366| > 0.160$ GeV) and the differences in the fit results are assigned as systematic uncertainties.

B_d^0 Contribution The default fit contains fixed PDFs describing the contamination from $B_d^0 \to J/\psi K^{0*}$ events mis-reconstructed as $B_s^0 \to J/\psi\phi$. To estimate uncertainties arising from these models, the main fit is repeated with the used fractions shifted about ±1σ. Also a different background angular description is tested using Legendre polynomials of 9 degree instead of 10 degree. The impact of these tests is found to have a negligible effect on the B_s^0 fit results.

The contribution of $B_d^0 \to J/\psi K^{\pm}\pi^{\mp}$ events as well as their interference with $B_d^0 \to J/\psi K^{0*}$ events is not included in the main fit and is instead assigned as a systematic uncertainty. To evaluate this, the MC background events are modelled using both the P-wave and S-wave decays and their interference, using the input parameters taken from [71]. The B_s^0 fit using this input is compared to the default fit, and differences is taken as a systematic uncertainty.

Λ_b Contribution Studies are performed to evaluate the effect of the uncertainties in the $\Lambda_b \to J/\psi p K^-$ fraction f_{Λ_b}, and the shapes of the mass, transversity angles, and lifetime distributions. MC angular distribution is modelled flat and then re-weighted. Test are performed using an alternative re-weighting and using no re-weighting at all. The default fit is also performed using the Λ_b lifetime shifted about ±1σ and using the MC generated Λ_b mass shape directly, without smoothing of the histogram.

Systematics	ϕ_s [rad]	$\Delta\Gamma_s$ [ps^{-1}]	Γ_s [ps^{-1}]	$\lvert A_\parallel(0)\rvert^2$	$\lvert A_0(0)\rvert^2$	$\lvert A_S(0)\rvert^2$	$\delta_\perp$ [rad]	$\delta_\parallel$ [rad]	$\delta_\perp - \delta_S$ [rad]
Tagging	0.025	0.003	$< 10^{-3}$	$< 10^{-3}$	$< 10^{-3}$	0.001	0.236	0.014	0.004
Acceptance	$< 10^{-3}$	$< 10^{-3}$	$< 10^{-3}$	0.003	$< 10^{-3}$	0.001	0.004	0.008	$< 10^{-3}$
ID Alignment	0.005	$< 10^{-3}$	0.002	$< 10^{-3}$	$< 10^{-3}$	$< 10^{-3}$	0.134	0.007	$< 10^{-3}$
Bck. Angles Model:									
p_T Bins	0.020	0.006	0.003	0.003	$< 10^{-3}$	0.008	0.004	0.006	0.008
Mass Interval	0.008	0.001	0.001	$< 10^{-3}$	$< 10^{-3}$	0.002	0.021	0.005	0.003
B_d^0 Contrib.	0.023	0.001	$< 10^{-3}$	0.002	0.002	0.017	0.090	0.011	0.009
Λ_b Contrib.	0.011	0.002	0.001	0.001	0.007	0.009	0.045	0.006	0.007
Models:									
Default Fit	0.001	0.002	$< 10^{-3}$	0.002	$< 10^{-3}$	0.002	0.025	0.015	0.002
Signal Mass	0.004	$< 10^{-3}$	$< 10^{-3}$	0.002	$< 10^{-3}$	0.001	0.015	0.017	$< 10^{-3}$
Background Mass	$< 10^{-3}$	0.002	$< 10^{-3}$	0.002	$< 10^{-3}$	0.002	0.027	0.038	$< 10^{-3}$
Time Resolution	0.003	$< 10^{-3}$	0.001	0.002	$< 10^{-3}$	0.002	0.057	0.011	0.001
Total	0.042	0.007	0.004	0.006	0.007	0.022	0.30	0.05	0.01

Table 8.6: Summary of the systematic uncertainties assigned to parameters of interest in the analysis of the 2012 data.

Behaviour of the default fit is tested using 1D likelihood scans for physics parameters as shown in figure 8.10. There are small asymmetries in the likelihood curves, but at the level of 1σ these are small compared to the corresponding statistical uncertainties of the physical variables, for which the scan is done.

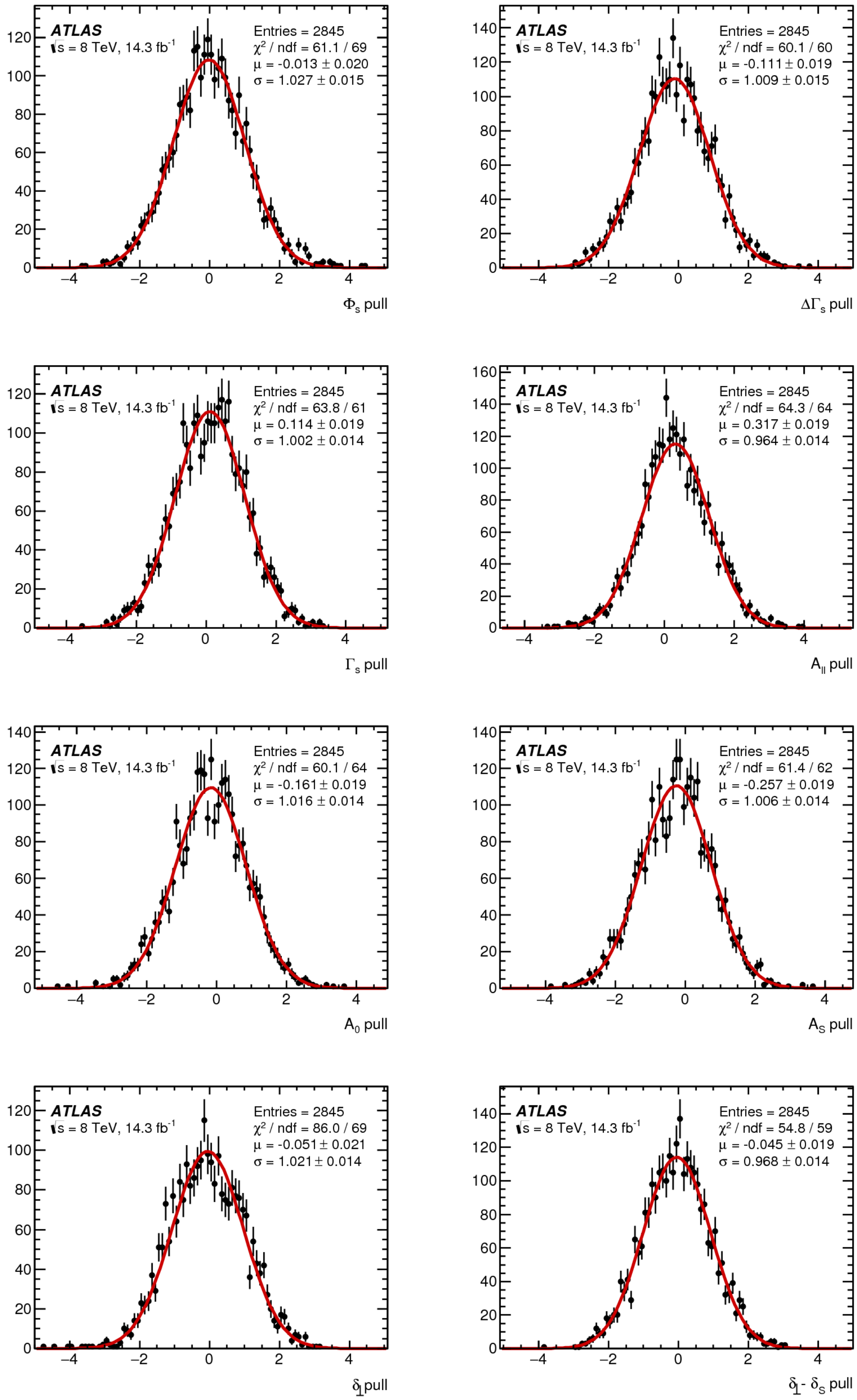

Figure 8.7: Pull distributions of the ≈ 2500 default fit model ToyMC pseudo-experiments fitted with a Gaussian function. The results from the 2012 real data fit are taken as input values for the generation of pseudo-events.

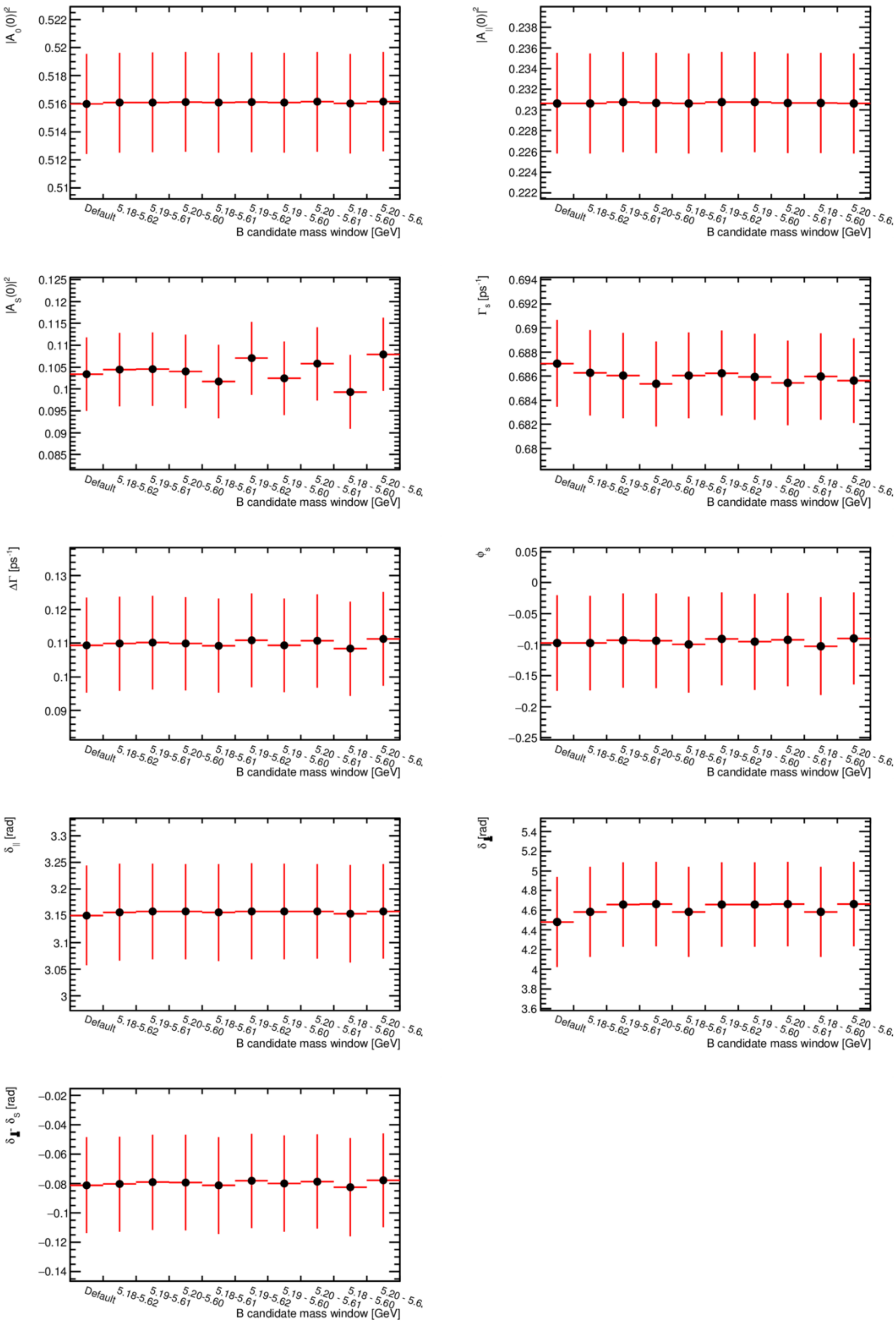

Figure 8.8: Stability of the main fit results using various B_s^0 candidate mass selection cuts.

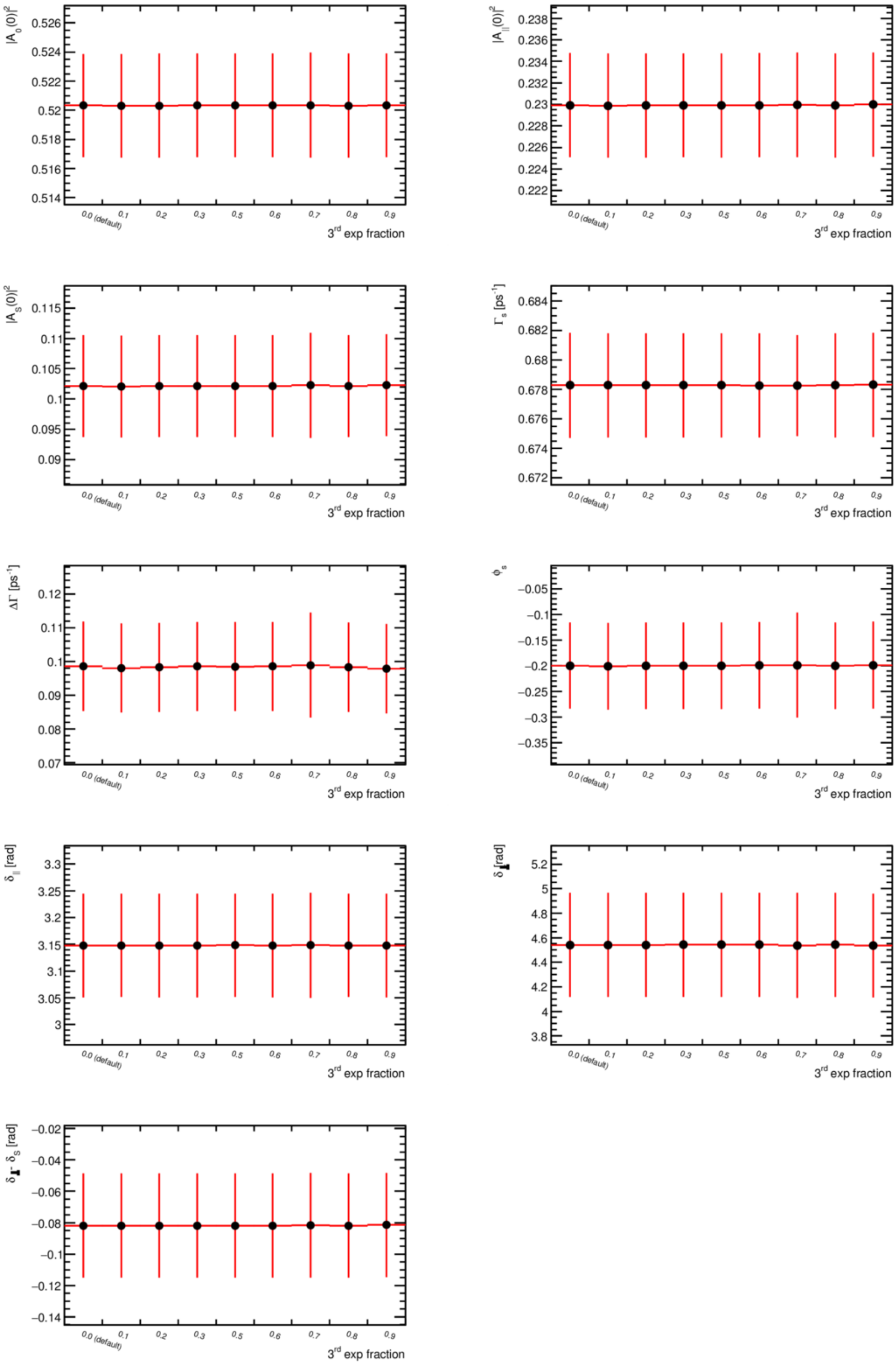

Figure 8.9: Comparison of the fit results for triple positive exponential background lifetime model with the relative fraction fixed to values from the range (0 - 1).

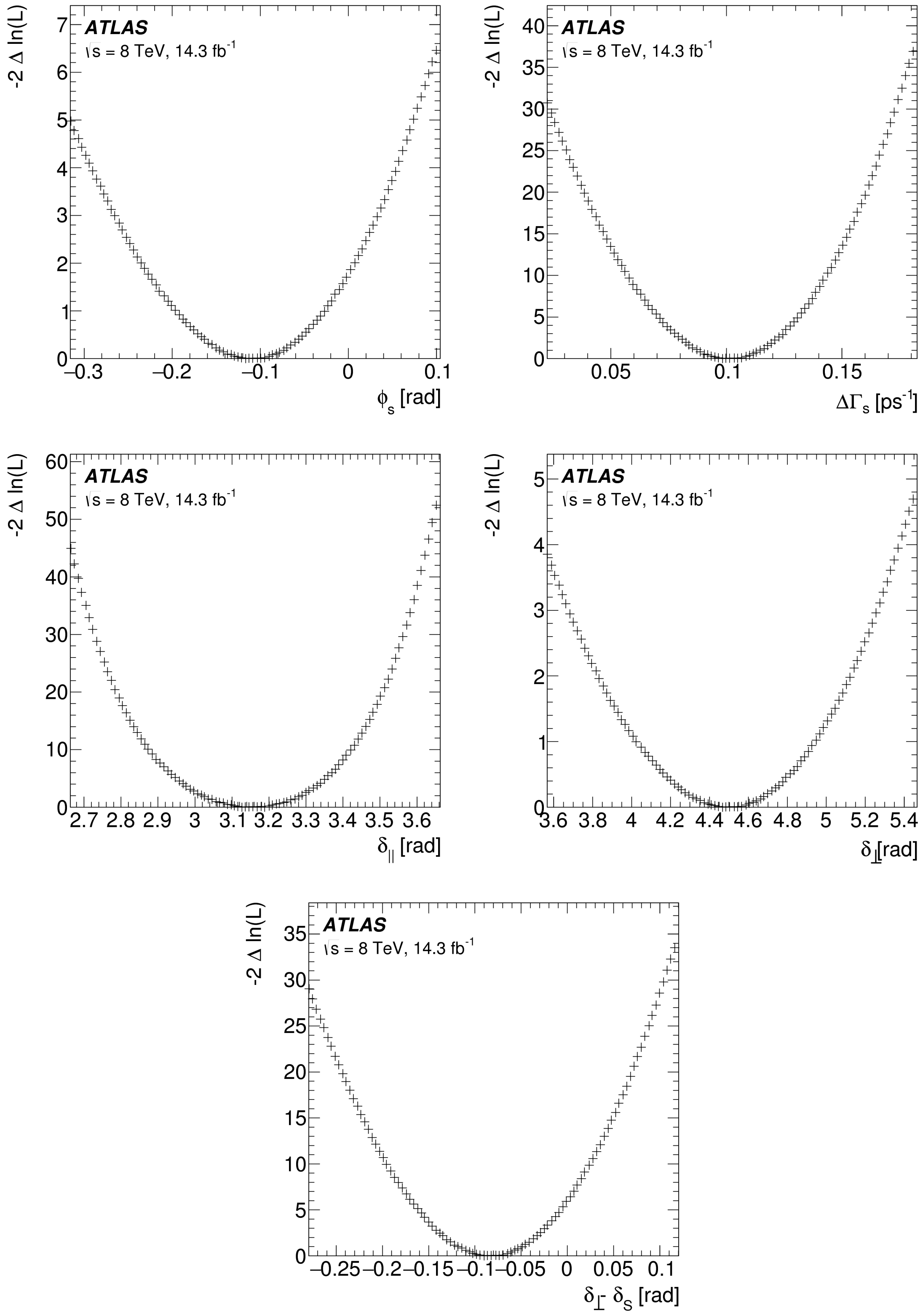

Figure 8.10: 1D likelihood scans for ϕ_s and $\Delta\Gamma_s$ parameters (top left and right, respectively) and for the strong phases $\delta_{\|}$, $\delta_{\perp}$, and $\delta_{\perp} - \delta_S$ (middle left, middle right, and bottom, respectively).

Chapter 9

Combination of the 7 TeV and 8 TeV Results

Results of the tagged analysis of the 7 TeV and 8 TeV data are consistent within uncertainties of these measurement and also with the SM prediction within 1σ, as can be seen in figure 9.1. Because of many changes made within the analysis between the two measurements, a statistical combination of the results is used to produce the overall result for Run1.

The combination makes use of a Best Linear Unbiased Estimate (BLUE) method and the relevant ROOT package [72, 73]. In this technique the combined result for parameter α from n estimates y_i is given by

$$\hat{x}_\alpha = \sum_{i=1}^{n} \lambda_{\alpha i} y_i, \tag{9.1}$$

where $\lambda_{\alpha i}$ are the weights assigned to each estimate. The variance of each parameter is given by

$$\mathrm{var}(\hat{x}_\alpha) = \sum_{i=1}^{n} \sum_{j=1}^{n} \lambda_{\alpha i} \mathcal{M}_{ij} \lambda_{\alpha j}. \tag{9.2}$$

In the simple case of combining two measurements of two parameters, e.g. a_1, a_2, b_1, b_2, the matrix $\mathcal{M}$ can be written as

$$\mathcal{M} = \begin{pmatrix} \mathrm{cov}(a_1,a_1) & \mathrm{cov}(a_1,a_2) & \mathrm{cov}(a_1,b_1) & \mathrm{cov}(a_1,b_2) \\ \mathrm{cov}(a_2,a_1) & \mathrm{cov}(a_2,a_2) & \mathrm{cov}(a_2,b_1) & \mathrm{cov}(a_2,b_2) \\ \mathrm{cov}(b_1,a_1) & \mathrm{cov}(b_1,a_2) & \mathrm{cov}(b_1,b_1) & \mathrm{cov}(b_1,b_2) \\ \mathrm{cov}(b_2,a_1) & \mathrm{cov}(b_2,a_2) & \mathrm{cov}(b_2,b_1) & \mathrm{cov}(b_2,b_2) \end{pmatrix}. \tag{9.3}$$

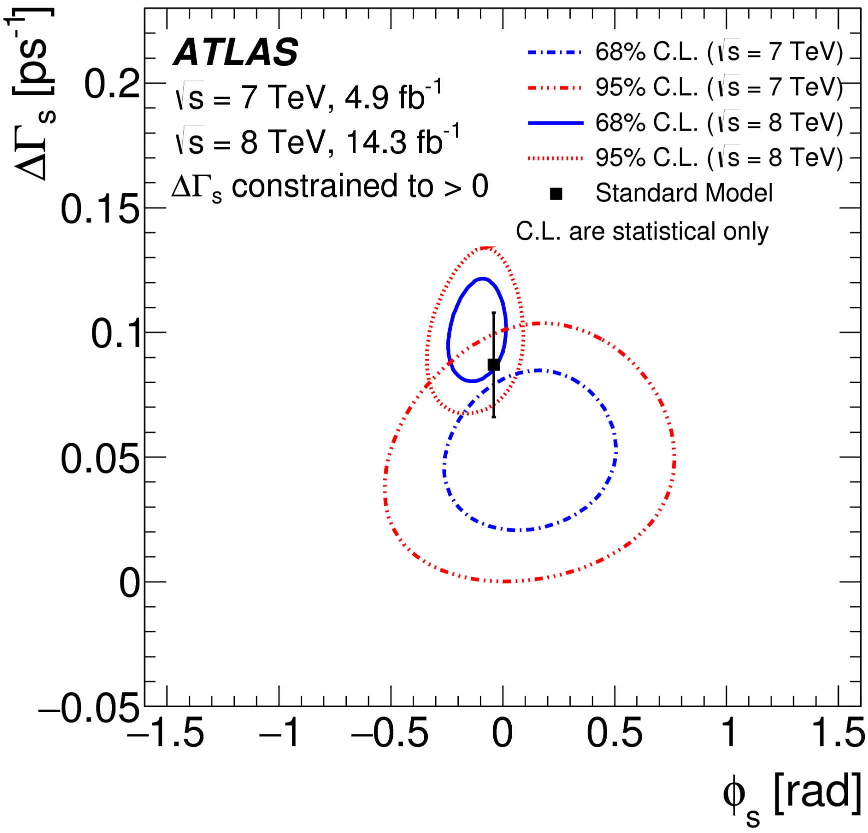

Figure 9.1: Likelihood contours in the $\phi_s - \Delta\Gamma_s$ plane for individual results from 7 TeV and 8 TeV data. The 68% likelihood contours are in blue, the 95% likelihood contours in red. Only statistical errors are used. The black line is the SM prediction.

It is also possible to split the matrix $\mathcal{M}$ into a sum of statistical and systematic correlation matrices $\mathcal{M}_{(\text{stat.})}$ and $\mathcal{M}_{(\text{syst.})}$ respectively

$$\mathcal{M} = \mathcal{M}_{(\text{stat.})} + \mathcal{M}_{(\text{syst.})}. \tag{9.4}$$

The BLUE technique involves finding the values of $\lambda_{\alpha i}$ that minimize $\text{var}(\hat{x}_\alpha)$. The measured values and uncertainties of the parameters in question as well as the correlations between them are required. Statistical correlations for individual measurements provided by the fits to 7 TeV and 8 TeV data are given in tables 7.5 and 8.5 respectively. Other correlations between the parameters for both the statistical and systematic uncertainties are estimated as follows:

- The events recorded in 2011 and 2012 are different, therefore there is no correlation between the statistical uncertainty.
- In both the 2011 and 2012 measurement, the systematic correlations between

parameters are summed in quadrature and therefore the correlation between them is assumed to be zero.

- There is clearly a systematic correlation between parameters of different years. These are split into several categories:
  - Systematic uncertainties quoted for the 2011 result only, i.e. the trigger efficiency, enter the combination along with a corresponding zero uncertainty for 2012 and no correlation.
  - Systematic uncertainties quoted for the 2012 result only. These are the background angles model, the choice of p_{T} bins and mass sidebands, and the specific Λ_b background. They enter the combination along with a corresponding zero uncertainty for 2011 and no correlation.
  - Systematic uncertainties common to both measurements: the ID alignment, the specific B_d^0 background, the fit model systematics, the acceptance and the tagging uncertainties. They enter the combination with a specific correlation coefficient ρ_i, where $i = \mathrm{ID}, B_d^0, \mathrm{mod}, \mathrm{acc}, \mathrm{tag}$, corresponding to the correlation between the 2011 and 2012 results. These coefficients can not be know exactly and have to be estimated and tested, as described below.

The ID did not change significantly between 2011 and 2012 data-taking and the ID alignment uncertainty is estimated in the same way for both measurements. Thus the correlation coefficient is set to $\rho_{\mathrm{ID}} = 1$.

For the B_d^0 contribution, while the systematic uncertainty tests are different, they are both performed to account for an imprecise knowledge of the B_d^0 contribution and are therefore assumed to be 100% correlated, i.e. using $\rho_{B_d^0} = 1$ in the combination.

The tagging, acceptance, and fit model systematic uncertainties are tested using several different combinations of values $\rho_i = 0, 0.25, 0.5, 0.75, 1$, where $i = \mathrm{tag}, \mathrm{acc}, \mathrm{mod}$. The electron tagging is added to the 2012 measurement, therefore the systematic uncertainty is not 100% correlated. Also the fit model was changed between the 2011 and 2012 measurement and it would be incorrect to estimate the correlation as 100%. However, a value of $\rho_i = 0$ represents the ideal case and $\rho_i = 1$ represents the worst case and they are used as a cross-check. Tests show only negligible differences between the combination results and thus a value $\rho_i = 0.5$ is used within the final BLUE combination.

The combined results for the fit parameters and their uncertainties for Run1 are given in table 9.1. The strong phases $\delta_{\parallel}$ and $\delta_{\perp} - \delta_S$ are given as 1σ confidence intervals. These are thus not considered in the combination and the 2012 result is taken as the Run1 result. Due to the significant negative correlation between Γ_s and $\Delta\Gamma_s$, and the change in the value of $\Delta\Gamma_s$ between the 2011 and 2012 results, the combined value of Γ_s is less than either individual result.

A graphical presentation of the combined results is shown in figure 9.2 as 68% and 95% likelihood contours. The results are consistent with the SM predictions, but they are still dominated by the statistical uncertainties. Given the precision of the theoretical prediction, new physics contributions still can not be excluded.

Parameter	2012 8 TeV Data			2011 7 TeV Data			Run1 Combined		
	Value	Stat.	Syst.	Value	Stat.	Syst.	Value	Stat.	Syst.
ϕ_s [rad]	-0.110	0.082	0.042	0.12	0.25	0.05	-0.090	0.078	0.041
$\Delta\Gamma_s$ [ps^{-1}]	0.101	0.013	0.007	0.053	0.021	0.010	0.085	0.011	0.007
Γ_s [ps^{-1}]	0.676	0.004	0.004	0.677	0.007	0.004	0.675	0.003	0.003
$\|A_0(0)\|^2$	0.520	0.004	0.007	0.529	0.006	0.012	0.522	0.003	0.007
$\|A_{\|\|}(0)\|^2$	0.230	0.005	0.006	0.220	0.008	0.009	0.227	0.004	0.006
$\|A_S(0)\|^2$	0.097	0.008	0.022	0.024	0.014	0.028	0.072	0.007	0.018
$\delta_\perp$ [rad]	4.50	0.45	0.30	3.89	0.47	0.11	4.15	0.32	0.16
$\delta_{\|\|}$ [rad]	3.15	0.10	0.05	[3.04, 3.23]		0.09	3.15	0.10	0.05
$\delta_\perp - \delta_S$ [rad]	-0.08	0.03	0.01	[3.02, 3.25]		0.04	-0.08	0.03	0.01

Table 9.1: Values for the physics parameters along with their statistical and systematic uncertainties obtained from the tagged analysis of the 8 TeV data, from the tagged analysis of the 7 TeV data, and the statistical combination of these measurement.

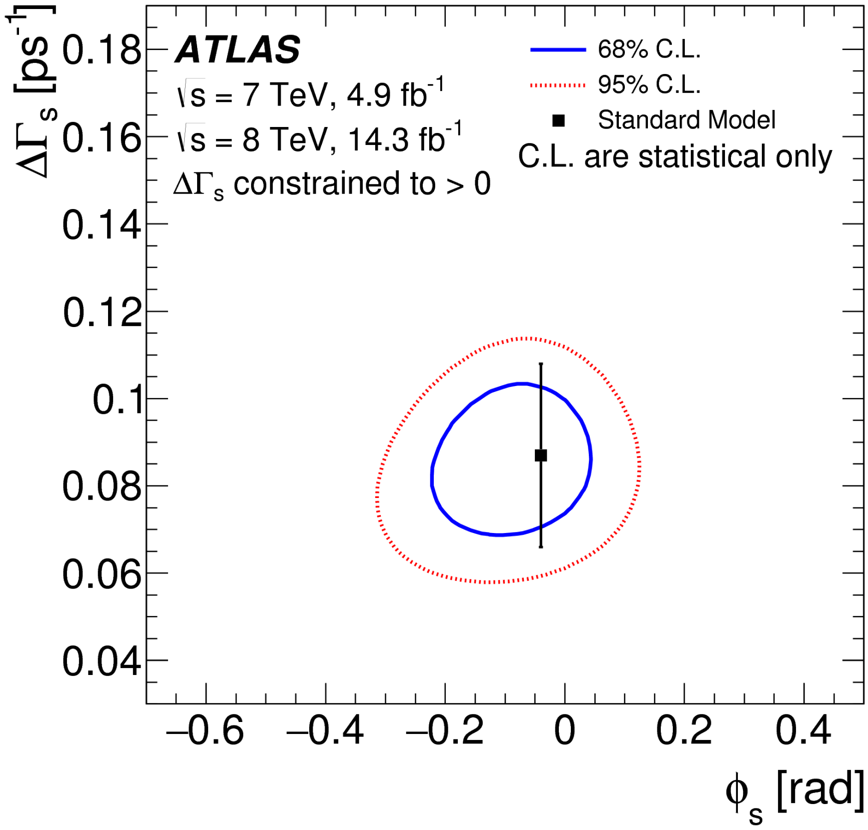

Figure 9.2: Likelihood contours in the $\phi_s - \Delta\Gamma_s$ plane for the final statistical combination of the results from 7 TeV and 8 TeV measurements. The blue line shows the 68% likelihood contour, while the red dotted line shows the 95% likelihood contour. Only statistical errors are used. The black line is the SM prediction.

Chapter 10

Conclusions

This thesis reports the results of the measurement of the time-dependent CP-violation parameters in the $B_s^0 \to J/\psi(\mu^+\mu^-)\phi(K^+K^-)$ decay in pp collisions at centre-of-mass energy of 8 TeV with 14.3 fb^{-1} and 7 TeV with 4.9 fb^{-1} of data collected using the ATLAS detector.

The current most successful theory of elementary particles and their interactions, the Standard Model, can not satisfactorily explain the large matter-antimatter asymmetry observed in the Universe. The $B_s^0 \to J/\psi\phi$ decay channel is expected to be sensitive to possible new contributions to CP-violation and thus provides us an insight to a new phenomena beyond the predictions of the Standard Model. In this channel, both the B_s^0 meson and its conjugate state $\overline{B_s^0}$ can decay into the same final state. CP-violation then occurs due to interference between the $B_s^0 - \overline{B_s^0}$ mixing and the direct decay amplitudes.

The physical parameters describing the CP-violation are extracted using the time-dependent angular analysis of the final state particles. Observed data are described by the probability density functions and fitted by the unbinned maximum likelihood fit. Nine physical parameters are obtained from the fit: the CP-violating weak phase ϕ_s, the average decay width Γ_s of the heavy and light mass eigenstates B_H and B_L respectively, the width difference $\Delta\Gamma_s$ of the mass eigenstates, three decay amplitudes $|A_0(0)|^2, |A_\parallel(0)|^2, |A_S(0)|^2$, and three strong phases $\delta_\parallel, \delta_\perp, \delta_S$.

The three consecutive ATLAS measurements are presented here. Initially an untagged analysis of the 7 TeV data was performed without using knowledge about the production flavour of the decaying B_s^0 candidate. The strong phase $\delta_\perp$ had to be thus constrained to the external measurements as well as the sign of the width difference $\Delta\Gamma_s$. The measurement was published in [7] and the results slightly improved the World averages of ϕ_s and $\Delta\Gamma_s$ (see table 6.5 and figure 6.10).

The application of the opposite-side tagging improved the sensitivity of the analysis to the weak phase ϕ_s and also released the constraint of the strong phase $\delta_\perp$. Uncertainty of the ϕ_s was thus reduced about $\sim 40\%$, as can be seen in table 7.8 and figure 7.8. The updated analysis was published in [8].

Due to the trigger tracking algorithm issues, the early 2012 data had to be disregarded. In spite of this, the amount of data available for 8 TeV analysis is almost three times larger than the 7 TeV data sample. Moreover, the additional tagging method was included into the analysis, new models were found to better describe the observed data, and the whole fitting framework was rewritten to be more stable, flexible, and faster. The values from the 8 TeV analysis are consistent with those obtained in the previous analysis. The two measurements are statistically combined into the final Run1 ATLAS result published in [9]:

$$\begin{aligned}
\phi_s &= -0.090 \pm 0.078\ \text{(stat.)} \pm 0.041\ \text{(syst.) rad} \\
\Delta\Gamma_s &= 0.085 \pm 0.011\ \text{(stat.)} \pm 0.007\ \text{(syst.) ps}^{-1} \\
\Gamma_s &= 0.675 \pm 0.003\ \text{(stat.)} \pm 0.003\ \text{(syst.) ps}^{-1} \\
|A_\parallel(0)|^2 &= 0.227 \pm 0.004\ \text{(stat.)} \pm 0.006\ \text{(syst.)} \\
|A_0(0)|^2 &= 0.522 \pm 0.003\ \text{(stat.)} \pm 0.007\ \text{(syst.)} \\
|A_S(0)|^2 &= 0.072 \pm 0.007\ \text{(stat.)} \pm 0.018\ \text{(syst.)} \\
\delta_\perp &= 4.15 \pm 0.32\ \text{(stat.)} \pm 0.16\ \text{(syst.) rad} \\
\delta_\parallel &= 3.15 \pm 0.10\ \text{(stat.)} \pm 0.05\ \text{(syst.) rad} \\
\delta_\perp - \delta_S &= -0.08 \pm 0.03\ \text{(stat.)} \pm 0.01\ \text{(syst.) rad.}
\end{aligned}$$

In such a high precision measurement, the correct evaluation of the systematic uncertainties is of crucial importance. Every aspect of the analysis, effects of the applied selections, or limitations of the chosen models, have to be carefully considered. This become even more important with the increasing statistical precision arising from the larger data sample. Due to the precise evaluation of the systematic sources, the measurement is limited by the insufficient statistics.

As can be seen in table 10.1 and figure 10.1, the ATLAS results are consistent with other LHC measurements within the given uncertainties and also with both Tevatron results, although they had significantly lower statistics. All measurements, as well as the combined result calculated by HFLAG, are consistent with the Standard Model predictions. However, ϕ_s and $\Delta\Gamma_s$ are not yet accurate enough to exclude the possible new physics contributions to the CP-violation in this sector.

The results presented in this analysis demonstrate that the ATLAS detector is capable of producing a measurement competitive even to the B-physics dedicated

	ϕ_s [rad]	$\Delta\Gamma_s[\mathrm{ps}^{-1}]$	Ref.
D0	$-0.55^{+0.38}_{-0.36}$	$0.163^{+0.065}_{-0.064}$	[27]
CDF	$[-0.60, 0.12]$, 68 % CL	$0.068 \pm 0.026 \pm 0.009$	[28]
LHC*b*	$-0.058 \pm 0.049 \pm 0.006$	$0.0805 \pm 0.0091 \pm 0.0032$	[74]
CMS	$-0.075 \pm 0.097 \pm 0.031$	$0.095 \pm 0.013 \pm 0.007$	[75]
ATLAS	$-0.090 \pm 0.078 \pm 0.041$	$0.085 \pm 0.011 \pm 0.007$	[9]
HFLAG	-0.030 ± 0.033	0.085 ± 0.007	[22]
SM	$-0.0363^{+0.0016}_{-0.0015}$	0.087 ± 0.021	[24], [64], resp.

Table 10.1: Summarized results of $B_s^0 \to J/\psi\phi$ CPV measurements from D0, CDF, LHC*b* (updated analysis), CMS, and ATLAS (combined Run1 measurement) experiments. The first error is due to statistics, the second one to systematics. HFLAG combined result is based also on the other LHC*b* measurements. SM stands for the Standard Model prediction.

experiments. A measurement that could potentially falsify the Standard Model prediction of the CP-violating parameters.

The analysis of the first portion of the Run2 *pp* data collected in 2015 and 2016 at centre-of-mass energy of 13 TeV is ongoing. Since the new data sample is almost two times larger the statistical precision will be improved by a factor of 30% under a conservative assumption that the signal to background ratio is similar between 8 and 13 TeV analysis [76]. Moreover, after the ATLAS tracking upgrade, when the new innermost Pixel layer was inserted into the Inner Detector, the precision of the lifetime measurement has significantly increased, as can be seen in figure 10.2 (cf. figure 8.5). The Run2 analysis may provide decisive evidence of the CP-violation in this sector.

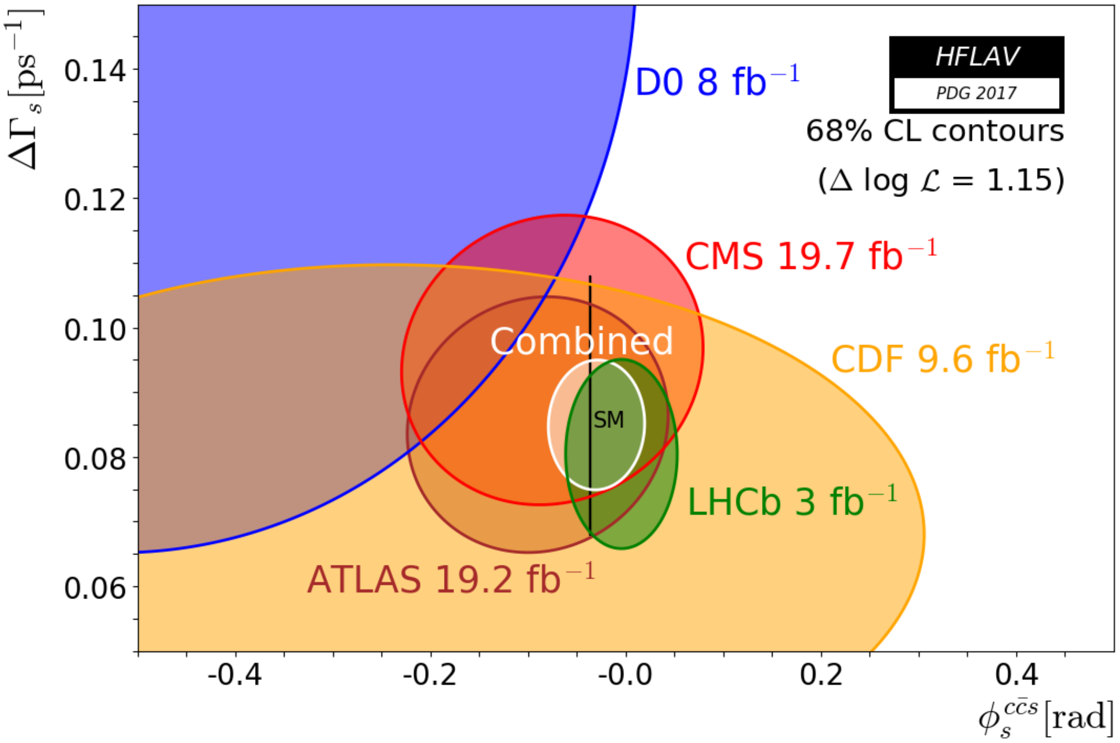

Figure 10.1: 68% CL regions in the $\phi_s - \Delta\Gamma_s$ plane obtained from individual and combined D0, CDF, LHC*b*, CMS, and ATLAS measurements. This plot presents an update of figure 7.8 with all the latest measurements. The SM expectation is shown as the black rectangle. Taken from [22].

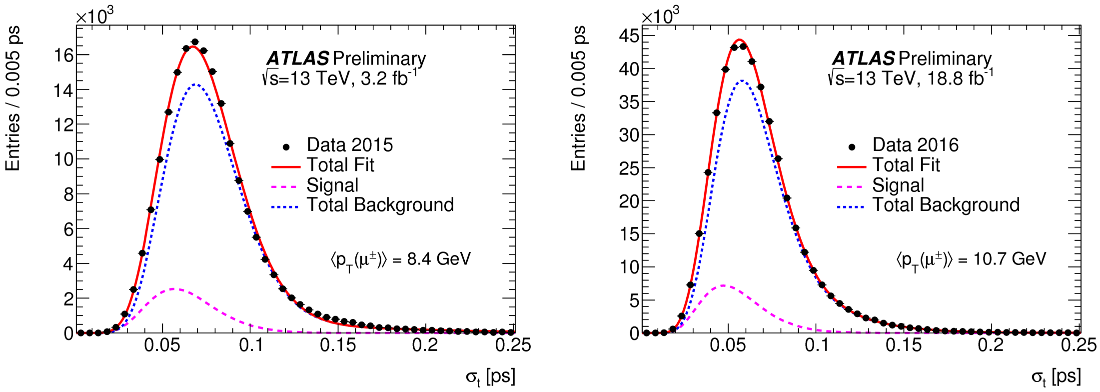

Figure 10.2: The B_s^0 proper decay time uncertainty distribution extracted from the $B_s^0 \to J/\psi\phi$ decay candidates in Run2 data collected in 2015 (left) and 2016 (right), the fits to the background and the signal fractions and the sum of the two fits. The trigger conditions in 2015 and 2016 data-taking lead to an average p_{T} of the muon candidates of 8.4 GeV and 10.7 GeV respectively. Figure prepared for the public page [77].

Bibliography

[1] ATLAS Collaboration, *The ATLAS Experiment at the CERN Large Hadron Collider*, JINST **3** (2008) S08003.

[2] CMS Collaboration, *The CMS Experiment at the CERN LHC*, JINST **3** (2008) S08004.

[3] L. Evans and P. Bryant (editors), *LHC Machine*, JINST **3** (2008) S08001.

[4] ATLAS Collaboration, *Observation of a new particle in the search for the Standard Model Higgs boson with the ATLAS detector at the LHC*, Phys. Lett. B **716** (2012) 1.

[5] CMS Collaboration, *Observation of a new boson at a mass of 125 GeV with the CMS experiment at the LHC*, Phys. Lett. B **716** (2012) 30.

[6] J. H. Christenson, J. W. Cronin, V. L. Fitch and R. Turlay, *Evidence for the 2 pi Decay of the k(2)0 Meson*, Phys. Rev. Lett. **13** (1964) 138.

[7] ATLAS Collaboration, *Time-dependent angular analysis of the decay* $B_s^0 \to J/\psi\phi$ *and extraction of* $\Delta\Gamma_s$ *and the CP-violating weak phase* ϕ_s *by ATLAS*, JHEP **1212** (2012) 072.

[8] ATLAS Collaboration, *Flavor tagged time-dependent angular analysis of the* $B_s \to J/\psi\phi$ *decay and extraction of* $\Delta\Gamma s$ *and the weak phase* ϕ_s *in ATLAS*, Phys. Rev. D **90** (2014) no.5, 052007.

[9] ATLAS Collaboration, *Measurement of the CP-violating phase* ϕ_s *and the* B_s^0 *meson decay width difference with* $B_s^0 \to J/\psi\phi$ *decays in ATLAS*, JHEP **1608** (2016) 147.

[10] ATLAS Collaboration, *Search for a Structure in the* $B_s^0\pi^\pm$ *Invariant Mass Spectrum with the ATLAS Experiment*, Phys. Rev. Lett. **120** (2018) no.20, 202007.

[11] M. Tanabashi *et al.* (Particle Data Group), *Review of Particle Physics*, Phys. Rev. D 98, 030001 (2018).

[12] D. H. Perkins, *Introduction to high energy physics; 4th ed.*, Cambridge University Press, 2000, p. 426, ISBN: 0521621968.

[13] P. W. Higgs, *Broken Symmetries and the Masses of Gauge Bosons*, Phys. Rev. Lett. **13** (1964) 508.

[14] F. Englert and R. Brout, *Broken Symmetry and the Mass of Gauge Vector Mesons*, Phys. Rev. Lett. **13** (1964) 321.

[15] M. Kobayashi and T. Maskawa, *CP Violation in the Renormalizable Theory of Weak Interaction*, Prog. Theor. Phys. **49** (1973) 652.

[16] J. Horejsi, *Fundamentals of electroweak theory*, Prague, Czech Republic: Karolinum Pr. (2002) 351 p.

[17] L. Wolfenstein, *Parametrization of the Kobayashi-Maskawa Matrix*, Phys. Rev. Lett. **51** (1983) 1945.

[18] A. J. Bevan *et al.*, *The Physics of the B Factories*, Eur. Phys. J. C **74** (2014) 3026.

[19] H. D. Politzer, *Reliable Perturbative Results for Strong Interactions?*, Phys. Rev. Lett. **30** (1973) 1346.

[20] D. J. Gross and F. Wilczek, *Ultraviolet Behavior of Nonabelian Gauge Theories*, Phys. Rev. Lett. **30** (1973) 1343.

[21] LHCb Collaboration, *Determination of the sign of the decay width difference in the B_s system*, Phys. Rev. Lett. **108** (2012) 241801.

[22] Y. Amhis *et al.* (Heavy Flavour Averaging Group), *Averages of b-hadron, c-hadron, and τ-lepton properties as of summer 2016*, Eur. Phys. J. C **77** (2017) no.12, 895 and online update at http://www.slac.stanford.edu/xorg/hfag.

[23] P. Ball and R. Fleischer, *An Analysis of B_s decays in the left-right symmetric model with spontaneous CP violation*, Phys. Lett. B **475** (2000) 111.

[24] J. Charles *et al.*, *Predictions of selected flavour observables within the Standard Model*, Phys. Rev. D **84** (2011) 033005.

[25] CDF Collaboration, *Measurement of the CP-Violating Phase* $\beta_s^{J/\psi\phi}$ *in* $B_s^0 \rightarrow J/\psi\phi$ *Decays with the CDF II Detector*, Phys. Rev. D **85** (2012) 072002.

[26] F. Azfar *et al.*, *Formulae for the Analysis of the Flavor-tagged Decay* $B_s^0 \rightarrow J\psi\phi$, JHEP **1011** (2010) 158.

[27] D0 Collaboration, *Measurement of the CP-violating phase* $\phi_s^{J/\psi\phi}$ *using the flavor-tagged decay* $B_s^0 \rightarrow J/\psi\phi$ *in 8* fb^{-1} *of* $p\bar{p}$ *collisions*, Phys. Rev. D **85** (2012) 032006.

[28] CDF Collaboration, *Measurement of the Bottom-Strange Meson Mixing Phase in the Full CDF Data Set*, Phys. Rev. Lett. **109** (2012) 171802.

[29] LHCb Collaboration, *Measurement of the CP-violating phase* ϕ_s *in the decay* $B_s^0 \rightarrow J/\psi\phi$, Phys. Rev. Lett. **108** (2012) 101803.

[30] LHCb Collaboration, *Tagged time-dependent angular analysis of* $B_s^0 \rightarrow J/\psi\phi$ *decays at LHCb*, LHCb-CONF-2012-002.

[31] Y. Amhis *et al.* (Heavy Flavour Averaging Group), *Averages of B-Hadron, C-Hadron, and tau-lepton properties as of early 2012*, arXiv:1207.1158 [hep-ex].

[32] *Timeline: The Large Hadron Collider*, `https://timeline.web.cern.ch/timelines/The-Large-Hadron-Collider`.

[33] *LHC Guide*, CERN-Brochure-2017-002-Eng.

[34] *Restarting the LHC: Why 13 Tev?*, `https://home.cern/about/engineering/restarting-lhc-why-13-tev`.

[35] C. Pralavorio, *Record luminosity: well done LHC*, `https://home.cern/about/updates/2017/11/record-luminosity-well-done-lhc`.

[36] M. Schaumann, *LHC report: xenon in action*, `https://home.cern/cern-people/updates/2017/10/lhc-report-xenon-action`.

[37] C. De Melis, *The CERN accelerator complex*, OPEN-PHO-ACCEL-2016-009.

[38] J. Pequenao, *Computer generated image of the whole ATLAS detector*, CERN-GE-0803012.

[39] J. Pequenao, *Computer generated image of the ATLAS inner detector*, CERN-GE-0803014.

[40] ATLAS Collaboration, *ATLAS Inner Detector Alignment Performance with February 2015 Cosmic Rays Data*, ATL-PHYS-PUB-2015-009.

[41] J. Pequenao, *Computer Generated image of the ATLAS calorimeter*, CERN-GE-0803015.

[42] ATLAS Collaboration, *Performance of the ATLAS muon trigger in pp collisions at $\sqrt{s} = 8$ TeV*, Eur. Phys. J. C **75** (2015) 120.

[43] T. Schoerner-Sadenius, *The Trigger of the ATLAS experiment*, Mod. Phys. Lett. A **18** (2003) 2149.

[44] ATLAS Collaboration, *Expected Performance of the ATLAS Experiment - Detector, Trigger and Physics*, arXiv:0901.0512 [hep-ex].

[45] ATLAS Collaboration, *Di-muon invariant mass for B physics triggers in 2011 data*, `https://twiki.cern.ch/twiki/bin/view/AtlasPublic/BPhysicsTriggerPublicResults#Di_muon_invariant_mass_for_B_phy`.

[46] ATLAS Software Project, *ATLAS Athena Guide*, `https://atlassoftwaredocs.web.cern.ch/athena/`.

[47] R. Brun and F. Rademakers, *ROOT - An Object Oriented Data Analysis Framework*, Proceedings AIHENP'96 Workshop, Lausanne, Sep. 1996, Nucl. Inst. & Meth. in Phys. Res. A 389 (1997) 81-86. See also `http://root.cern.ch/`.

[48] W. Verkerke, D. Kirkby, *RooFit Users Manual v2.91*, `https://root.cern.ch/download/doc/RooFit_Users_Manual_2.91-33.pdf`.

[49] T. Sjostrand, P. Eden, C. Friberg, L. Lonnblad, G. Miu, S. Mrenna and E. Norrbin, *High-energy physics event generation with PYTHIA 6.1*, Comput. Phys. Commun. **135** (2001) 238.

[50] G. Corcella, I. G. Knowles, G. Marchesini, S. Moretti, K. Odagiri, P. Richardson, M. H. Seymour and B. R. Webber, *HERWIG 6.5 release note*, JHEP 0101 (2001) 010, hep-ph/0210213; new version at `https://herwig.hepforge.org/`.

[51] M. Smizanska, *PythiaB an interface to Pythia6 dedicated to simulation of beauty events*, ATL-COM-PHYS-2003-038.

[52] M. Smizanska and J. Catmore, *EvtGen in ATLAS; rev. version*, ATL-COM-PHYS-2004-041.

[53] GEANT4 Collaboration, *GEANT4: A Simulation toolkit*, `https://geant4.web.cern.ch/`.

[54] ATLAS Collaboration, *Total Integrated Luminosity and Data Quality in 2011 and 2012*, `https://twiki.cern.ch/twiki/bin/view/AtlasPublic/LuminosityPublicResults#Integrated_luminosity_summary_pl`.

[55] ATLAS Collaboration, *ATLAS tunes of PYTHIA 6 and Pythia 8 for MC11*, ATL-PHYS-PUB-2011-009.

[56] K. Nakamura *et al.* (Particle Data Group), *Review of particle physics*, J. Phys. G **37** (2010) 075021.

[57] K. A. Olive *et al.* (Particle Data Group), *Review of Particle Physics*, Chin. Phys. C **38** (2014) 090001.

[58] T. Jakoubek, *Summary of PV systematics, Data2011 vs. MC2011 comparison*, `https://indico.cern.ch/event/172239/contributions/272460/attachments/216096/302820/bsjpsiphi_summary_jakoubek.pdf`.

[59] G. Punzi, *Comments on likelihood fits with variable resolution*, eConf C **030908** (2003) WELT002, physics/0401045 [physics.data-an].

[60] CDF Collaboration, *Observation of $B_s^0 - \bar{B}_s^0$ Oscillations*, Phys. Rev. Lett. **97** (2006) 242003.

[61] LHCb Collaboration, *Determination of the sign of the decay width difference in the B_s system*, Phys. Rev. Lett. **108** (2012) 241801.

[62] ATLAS Collaboration, *Alignment of the ATLAS Inner Detector Tracking System with 2010 LHC proton-proton collisions at $\sqrt{s} = 7$ TeV*, ATLAS-CONF-2011-012.

[63] Y. Amhis *et al.* (Heavy Flavour Averaging Group), *Averages of B-Hadron, C-Hadron, and tau-lepton properties as of early 2012*, arXiv:1207.1158 [hep-ex], "fall" online update of [31] at `http://www.slac.stanford.edu/xorg/hflav/osc/fall_2012/HFAG_Chapter3_oct2012.pdf`.

[64] A. Lenz and U. Nierste, *Numerical Updates of Lifetimes and Mixing Parameters of B Mesons*, arXiv:1102.4274 [hep-ph].

[65] ATLAS Collaboration, *Commissioning of the ATLAS high-performance b-tagging algorithms in the 7 TeV collision data*, ATLAS-CONF-2011-102.

[66] M. Cacciari, G. P. Salam and G. Soyez, *The anti-k_t jet clustering algorithm*, JHEP **0804** (2008) 063.

[67] LHCb Collaboration, *Measurement of CP violation and the B_s^0 meson decay width difference with $B_s^0 \to J/\psi K^+K^-$ and $B_s^0 \to J/\psi\pi^+\pi^-$ decays*, Phys. Rev. D **87** (2013) no.11, 112010.

[68] Y. Amhis *et al.* (Heavy Flavour Averaging Group), *Averages of B-Hadron, C-Hadron, and tau-lepton properties as of early 2012*, arXiv:1207.1158 [hep-ex], "spring" online update of [31] at `http://www.slac.stanford.edu/xorg/hflav/osc/spring_2014/HFAG_Chapter3_current.pdf`.

[69] LHCb Collaboration, *Study of the kinematic dependences of Λ_b^0 production in pp collisions and a measurement of the $\Lambda_b^0 \to \Lambda_c^+\,\pi^-$ branching fraction*, JHEP **1408** (2014) 143.

[70] LHCb Collaboration, *Study of the production of Λ_b^0 and $\overline{B}^0$ hadrons in pp collisions and first measurement of the $\Lambda_b^0 \to J/\psi pK^-$ branching fraction*, Chin. Phys. C **40** (2016) no.1, 011001.

[71] LHCb Collaboration, *Measurement of the polarization amplitudes in $B^0 \to J/\psi K^*(892)^0$ decays*, Phys. Rev. D **88** (2013) 052002.

[72] R. Nisius, *On the combination of correlated estimates of a physics observable*, Eur. Phys. J. C **74** (2014) no.8, 3004.

[73] R. Nisius, *BLUE: a software package to combine correlated estimates of physics observables within ROOT using the Best Linear Unbiased Estimate method - Program manual*, Version 1.9.2, `http://blue.hepforge.org`.

[74] LHCb Collaboration, *Precision measurement of CP violation in $B_s^0 \to J/\psi K^+K^-$ decays*, Phys. Rev. Lett. **114** (2015) no.4, 041801.

[75] CMS Collaboration, *Measurement of the CP-violating weak phase ϕ_s and the decay width difference $\Delta\Gamma_s$ using the $B_s^0 \to J/\psi\phi(1020)$ decay channel in pp collisions at $\sqrt{s} = 8$ TeV*, Phys. Lett. B **757** (2016) 97.

[76] ATLAS Collaboration, *ATLAS B-physics studies at increased LHC luminosity, potential for CP-violation measurement in the $B_s^0 \to J/\psi\phi$ decay*, ATL-PHYS-PUB-2013-010.

[77] ATLAS Collaboration, *B_s^0 proper decay time resolution in the $B_s^0 \to J/\psi(\mu^+\mu^-)\phi(K^+K^-)$ decay for Run-1, Run-2 and HL-LHC*,

https://atlas.web.cern.ch/Atlas/GROUPS/PHYSICS/PLOTS/BPHYS-2016-001.

Appendices

Appendix A

$B_s^0\pi$ Analysis

Following pages are the arXiv e-print of the paper *Search for tetraquark in* $B_s^0\pi$ *decays*, published in [10]. This measurement uses the same decay channel ($B_s^0 \to J/\psi\phi$) and shares most of the reconstruction techniques with the analysis presented in the thesis, but it does not fit into the scope, because there is no relation to the CP-violation at all. The author has spent almost two years working on this measurement as one of the main analysers and he thinks that the paper thus deserves to be at least included in the Appendix.

The whole paper is given except for the very long ATLAS author list, which is available online at [10].

EUROPEAN ORGANISATION FOR NUCLEAR RESEARCH (CERN)

Phys. Rev. Lett. 120 (2018) 202007
DOI: 10.1103/PhysRevLett.120.202007

CERN-EP-2017-333
June 21, 2018

Search for a Structure in the $B_s^0\,\pi^\pm$ Invariant Mass Spectrum with the ATLAS Experiment

The ATLAS Collaboration

A search for the narrow structure, $X(5568)$, reported by the D0 Collaboration in the decay sequence $X \to B_s^0\,\pi^\pm$, $B_s^0 \to J/\psi\phi$, is presented. The analysis is based on a data sample recorded with the ATLAS detector at the LHC corresponding to 4.9 fb^{-1} of pp collisions at 7 TeV and 19.5 fb^{-1} at 8 TeV. No significant signal was found. Upper limits on the number of signal events, with properties corresponding to those reported by D0, and on the X production rate relative to B_s^0 mesons, ρ_X, were determined at 95% confidence level. The results are $N(X) < 382$ and $\rho_X < 0.015$ for B_s^0 mesons with transverse momenta above 10 GeV, and $N(X) < 356$ and $\rho_X < 0.016$ for transverse momenta above 15 GeV. Limits are also set for potential $B_s^0\,\pi^\pm$ resonances in the mass range 5550 MeV to 5700 MeV.

The D0 Collaboration reported evidence of a narrow structure, $X(5568)$, in the decay $X \to B_s^0\,\pi^\pm$ with $B_s^0 \to J/\psi\phi$ in proton–antiproton collisions at a center-of-mass energy of $\sqrt{s} = 1.96$ TeV at the Tevatron collider [1]. The structure was interpreted as a tetraquark with four different quark flavors: b, s, u and d. The mass and natural width of this state were fitted to be $m = 5567.8 \pm 2.9(\text{stat})^{+0.9}_{-1.9}(\text{syst})$ MeV and $\Gamma = 21.9 \pm 6.4(\text{stat})^{+5.0}_{-2.5}(\text{syst})$ MeV, respectively, and the signal significance is 5.1 σ. The ratio ρ_X of the yield of $X(5568)$ to the yield of the B_s^0 meson for a transverse momentum range $10 < p_\text{T}(B_s^0) < 30$ GeV was measured to be $0.086 \pm 0.019(\text{stat}) \pm 0.014(\text{syst})$. The result initiated a discussion of the nature of the new state and prospects for observation of other tetraquark hadrons [2–6]. Recently, the D0 Collaboration reported further evidence for the resonance $X(5568)$ [7] in the decay sequence $X \to B_s^0\,\pi^\pm$, $B_s^0 \to \mu^\mp \nu D_s^\pm$, $D_s^\pm \to \phi\pi^\pm$, which is consistent with their previous measurement [1]. However, searches for $X(5568)$ in decays to $B_s^0\,\pi^\pm$, $B_s^0 \to J/\psi\phi$ performed by the LHCb [8] and CMS [9] Collaborations in proton–proton (pp) collisions at the LHC and by the CDF Collaboration [10] at the Tevatron, revealed no signal. The upper limits $\rho_X < 0.024$ (LHCb, $p_\text{T}(B_s^0) > 10$ GeV), $\rho_X < 0.011$ (CMS, $p_\text{T}(B_s^0) > 10$ GeV) and $\rho_X < 0.010$ (CMS, $p_\text{T}(B_s^0) > 15$ GeV) at 95% confidence level (CL) were determined within the acceptances of the LHCb and CMS experiments. CDF set an upper limit $\rho_X < 0.067$ at 95% CL within a kinematic range similar to that of D0 [1].

In this Letter, a search for the $X(5568)$ state by the ATLAS experiment at the LHC is presented (B_s^0 refers to both the B_s^0 and $\bar{B}_s^0$ mesons). The B_s^0 mesons are reconstructed in their decays to $J/\psi(\mu^+\mu^-)\,\phi(K^+K^-)$. The analysis is based on a combined sample of pp collision data at $\sqrt{s} = 7$ TeV and 8 TeV corresponding to integrated luminosities of 4.9 fb^{-1} and 19.5 fb^{-1}, respectively. The ATLAS detector [11] covers nearly the entire solid angle around the collision point with layers of tracking detectors, calorimeters and muon chambers. The muon and tracking systems are of particular importance in the reconstruction of B mesons. The inner tracking detector (ID) consists of a silicon pixel detector, a silicon microstrip detector and a transition radiation tracker. The muon spectrometer (MS) surrounds the calorimeters and consists of three large superconducting toroids with eight coils each, a system of tracking chambers, and detectors for triggering. To study the detector response, to estimate backgrounds and to model systematic effects, 12 million Monte Carlo (MC) simulated $B_s^0 \to J/\psi\phi$ and 1 million $B_s^0\,\pi^\pm$ events were generated using Pythia 8.183 [12, 13] tuned with ATLAS data [14]. Multiple overlaid proton–proton collisions (pileup) were simulated with Pythia soft QCD processes. The detector response was simulated using the ATLAS simulation framework [15] based on GEANT4 [16]. The MC events were weighted to reproduce the same pileup and trigger conditions as in the data. As in the D0 analysis [1], the $B_s^0\,\pi^\pm$ resonance was generated using the Breit–Wigner (BW) parameterization appropriate for an S-wave two-body decay near threshold:

$$F_\text{BW}\left(m(B_s^0\,\pi^\pm), m_X, \Gamma_X\right) = \frac{m(B_s^0\,\pi^\pm)\cdot m_X \cdot \Gamma\left(m(B_s^0\,\pi^\pm), \Gamma_X\right)}{\left(m_X^2 - m^2(B_s^0\,\pi^\pm)\right)^2 + m_X^2 \cdot \Gamma^2\left(m(B_s^0\,\pi^\pm), \Gamma_X\right)}, \quad (1)$$

where $m(B_s^0\,\pi^\pm)$ is the invariant mass of the $B_s^0\,\pi^\pm$ candidate and m_X and Γ_X are the mass and the natural width of the resonance. The mass-dependent width is $\Gamma\left(m(B_s^0\,\pi^\pm), \Gamma_X\right) = \Gamma_X \cdot (q_1/q_0)$, where q_1 and q_0 are the magnitudes of the three-vector momenta of the B_s^0 meson in the rest frame of the $B_s^0\,\pi^\pm$ system at the invariant masses equal to $m(B_s^0\,\pi^\pm)$ and m_X, respectively. The mass and the width were set to $m_X = 5567.8$ MeV and $\Gamma_X = 21.9$ MeV, as reported in Ref. [1]. The events were selected by the dimuon triggers [17] based on identification of a $J/\psi \to \mu^+\mu^-$ decay, with p_T thresholds of either 4 GeV or 6 GeV, with both symmetric, $(4,4)$ GeV or $(6,6)$ GeV, and asymmetric, $(4,6)$ GeV, combinations. In addition, each event must contain at least one reconstructed primary vertex (PV), formed from at least six

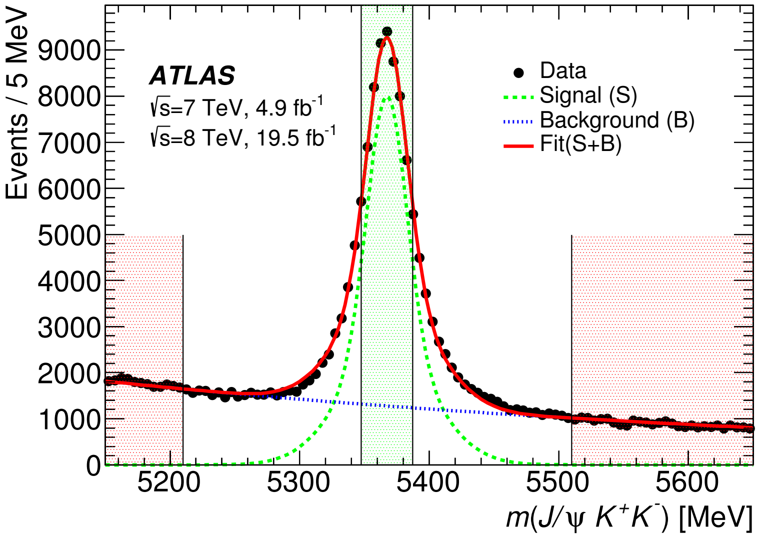

Figure 1: The invariant mass distribution for $B_s^0 \to J/\psi\phi$ candidates satisfying the selection criteria. Data are shown as points and results of fits to signal (dashed), background (dotted), and the total fit (solid) are shown as lines. The two outer (red) shaded bands and the central (green) shaded band represent the mass sidebands and the signal region of B_s^0 meson candidates, respectively.

ID tracks. The selection of J/ψ and $\phi \to K^+K^-$ candidates is identical to the one described in detail in Ref. [18]. Candidates for $B_s^0 \to J/\psi\phi$ decays are selected by fitting the tracks for each combination of $J/\psi \to \mu^+\mu^-$ and $\phi \to K^+K^-$ to a common vertex. The fit is further constrained by fixing the invariant mass of the two muon tracks to the J/ψ mass [19]. A quadruplet of tracks is accepted for further analysis if the vertex fit has a χ^2/d.o.f. < 3. For each B_s^0 meson candidate the proper decay time t is extracted using the method described in Ref. [18]. Events with $t > 0.2$ ps are selected to reduce the background from the events with a J/ψ produced directly in the pp collision. If there is more than one accepted B_s^0 candidate in the event, the candidate with the lowest χ^2/d.o.f. of the vertex fit is selected. For the selected events the average number of proton–proton interactions per bunch crossing is 21, necessitating a choice of the best candidate for the PV at which the B_s^0 meson is produced. The variable used is the three-dimensional impact parameter d_0, which is calculated as the distance between the line extrapolated from the reconstructed B_s^0 meson vertex in the direction of the B_s^0 momentum, and each PV candidate. The chosen PV is the one with the smallest d_0. Using MC simulation it was shown that the fraction of B_s^0 candidates that are assigned the wrong PV is less than 1% [18] and that the corresponding effect on the results is negligible. Finally, a requirement that the B_s^0 transverse momentum is greater than 10 GeV is applied. Figure 1 shows the reconstructed $J/\psi K^+K^-$ mass distribution and the result of an extended unbinned maximum-likelihood fit in the range (5150 – 5650) MeV, in which the signal is modeled by a sum of two Gaussian distributions and an exponential function is used to model the combinatorial background. The observed signal width is consistent with MC simulation. The fitted B_s^0 mass is $m_{\mathrm{fit}}(B_s^0) = 5366.6 \pm 0.1$ (stat) MeV, in agreement with the world average value 5366.89 ± 0.19 MeV [19]. For further investigation, only candidates with a reconstructed mass in the signal region 5346.6 – 5386.6 MeV are included, which gives $N(B_s^0) = 52750 \pm 280$ (stat) candidates.

The $B_s^0\,\pi^\pm$ candidates are constructed by combining each of the tracks forming the selected PV with the selected B_s^0 candidate. Tracks that were already used to reconstruct the B_s^0 candidate and tracks identified as leptons (e or μ) are excluded, as well as tracks with transverse momentum $p_\mathrm{T} < 500$ MeV. This p_T selection was chosen to maximize the ratio of the $B_s^0\,\pi^\pm$ signal to the background, based on MC simulation. Assigning the pion mass hypothesis to the tracks that pass these selection criteria, the mass $m(B_s^0\,\pi^\pm)$ is calculated as $m(J/\psi KK\pi^\pm) - m(J/\psi KK) + m_\mathrm{fit}(B_s^0)$, where $m_\mathrm{fit}(B_s^0) = 5366.6$ MeV. On average there are 1.8 $B_s^0\,\pi^\pm$ candidates in each selected event and all are retained for the analysis. A systematic study has shown that the effect on the results due to multiple candidates is negligible. The mass distribution of $B_s^0\,\pi^\pm$ candidates is fitted using an extended unbinned maximum-likelihood method. The probability density function (PDF) for the background component is defined as a threshold function:

$$F_\mathrm{bck}\left(m(B_s^0\,\pi^\pm)\right) = \left(\frac{m(B_s^0\,\pi^\pm) - m_\mathrm{thr}}{n}\right)^a \cdot \exp\left(\sum_{i=1}^{4} p_i \cdot \left(\frac{m(B_s^0\,\pi^\pm) - m_\mathrm{thr}}{n}\right)^i\right), \tag{2}$$

where $m_\mathrm{thr} = m_\mathrm{fit}(B_s^0) + m_\pi$ and n, a, p_i are free parameters of the fit. The background PDF was tested using events with no real $B_s^0\,\pi^\pm$ candidates from two categories. The first background sample contains data events where $B_s^0\,\pi^\pm$ candidates are formed using “fake” B_s^0 mesons from the mass sidebands, shown in Figure 1 by red shaded bands, defined as $5150 < m(J/\psi K^+K^-) < 5210$ MeV and $5510 < m(J/\psi K^+K^-) < 5650$ MeV. The second background sample is modeled using MC events containing only B_s^0 mesons not originating from the $B_s^0\,\pi^\pm$ signal, tuned to reproduce the B_s^0 transverse momentum distribution in data. In these events the B_s^0 meson is combined with each of the tracks originating from the selected PV. The first sample is normalized to the fitted number of B_s^0 background events in the B_s^0 mass signal region 5346.6 – 5386.6 MeV, while the second sample is normalized to the fitted number of B_s^0 signal events in the same region. The sum of these two distributions is consistent with the distribution of the data. The function in Eq. (2) describes both background distributions as well as their sum within uncertainties. The signal PDF $F_\mathrm{sig}\left(m(B_s^0\,\pi^\pm)\right)$ is defined as a convolution of an S-wave Breit–Wigner PDF, defined in Eq. (1), and the detector resolution represented by a Gaussian function with a width that is calculated individually for each $B_s^0\,\pi^\pm$ candidate from the tracking and vertexing error matrices. Using MC and data samples, it has been verified that the per candidate mass resolutions are the same for the $B_s^0\,\pi^\pm$ signal and for the background events passing the selection criteria. The average resolution for the $B_s^0\,\pi^\pm$ signal, with the mass and width corresponding to those of the structure reported by the D0 Collaboration ($m_X = 5567.8$ MeV and $\Gamma_X = 21.9$ MeV), is 3.2 MeV. The full probability function used is

$$F\left(m(B_s^0\,\pi^\pm)\right) = N(X)\cdot F_\mathrm{sig}\left(m(B_s^0\,\pi^\pm)\right) + (N_\mathrm{can} - N(X))\cdot F_\mathrm{bck}\left(m(B_s^0\,\pi^\pm)\right), \tag{3}$$

where $N(X)$ is the number of signal events and N_can is the number of all selected $B_s^0\,\pi^\pm$ candidates. The signal mass and width are fixed to the central values reported by the D0 Collaboration. Following other experiments, fits are performed for two subsets of $B_s^0\,\pi^\pm$ candidates, first with $p_\mathrm{T}(B_s^0) > 10$ GeV and second with $p_\mathrm{T}(B_s^0) > 15$ GeV. The results of the fits are shown in Figure 2 and summarized in Table 1. No significant $X(5568)$ signal is observed. Additional selections such as cuts on the angle between the momenta of the B_s^0 and $\pi^\pm$ candidates were investigated and did not produce evidence of a signal. These were found to introduce peaking background so are not included in the analysis. The yields $N(X)$ and

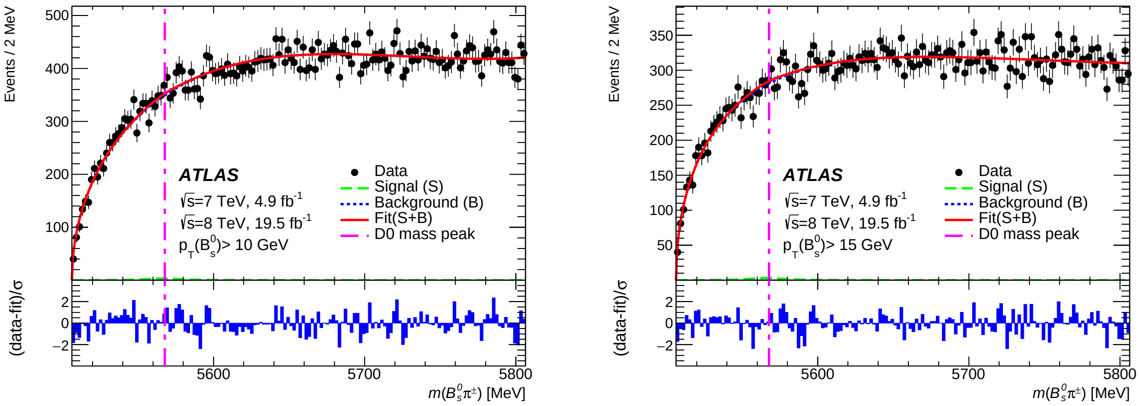

Figure 2: Results of the fit to the $B_s^0\,\pi^\pm$ mass distribution for candidates with $p_{\mathrm{T}}(B_s^0) > 10$ GeV (left) and $p_{\mathrm{T}}(B_s^0) > 15$ GeV (right). The bottom panels show the difference between each data point and the fit divided by the statistical uncertainty of that point.

$N(B_s^0)$ obtained from the fits are used to evaluate the X production rate relative to B_s^0, within the ATLAS acceptance, using the formula

$$\rho_X \equiv \frac{\sigma(pp \to X + \text{anything}) \times \mathcal{B}(X \to B_s^0\pi^\pm)}{\sigma(pp \to B_s^0 + \text{anything})} = \frac{N(X)}{N(B_s^0)} \times \frac{1}{\epsilon^{\mathrm{rel}}(X)}, \tag{4}$$

where σ represents the production cross-section for each of the particles, within the ATLAS acceptance, and the relative efficiency $\epsilon^{\mathrm{rel}}(X) = \epsilon(X)/\epsilon(B_s^0)$ is the selection efficiency for the state X, decaying to $B_s^0\,\pi^\pm$, relative to that for the B_s^0 meson and accounts for the reconstruction and selection efficiency of the companion pion, including the soft pion acceptance.

Table 1: Yields of B_s^0 and $X(5568)$ candidates obtained from the fits to the B_s^0 and $B_s^0\pi^\pm$ candidate mass distributions, with statistical uncertainties. The values given for $N(B_s^0)$ are those inside the B_s^0 signal window. The reported values for $X(5568)$ are obtained from the fits with signal mass and width parameters fixed to those reported by the D0 Collaboration. The relative efficiencies $\epsilon^{\mathrm{rel}}(X)$ and their uncertainties are described in the text.

$N(B_s^0)/10^3$	$p_{\mathrm{T}}(B_s^0) > 10$ GeV	52.75 ± 0.28
	$p_{\mathrm{T}}(B_s^0) > 15$ GeV	43.46 ± 0.24
$N(X)$	$p_{\mathrm{T}}(B_s^0) > 10$ GeV	60 ± 140
	$p_{\mathrm{T}}(B_s^0) > 15$ GeV	-30 ± 150
$\epsilon^{\mathrm{rel}}(X)$	$p_{\mathrm{T}}(B_s^0) > 10$ GeV	0.53 ± 0.09
	$p_{\mathrm{T}}(B_s^0) > 15$ GeV	0.60 ± 0.10

The relative efficiency, $\epsilon^{\mathrm{rel}}(X)$, was determined using MC simulation of events containing $X \to B_s^0\,\pi^\pm$ and B_s^0 decays. In the ratio, the acceptance of the B_s^0 decay cancels, so the value to be determined is the pion reconstruction efficiency for $B_s^0\,\pi^\pm$ events in which the B_s^0 meson satisfies acceptance, reconstruction and selection criteria. Based on MC events, $\epsilon^{\mathrm{rel}}(X)$ is determined as a function of $p_{\mathrm{T}}(B_s^0)$ and of $m(B_s^0\,\pi^\pm)$. Using an MC-based function, the acceptance is determined individually for each $B_s^0\,\pi^\pm$ candidate, based on its measured values of $p_{\mathrm{T}}(B_s^0)$ and $m(B_s^0\,\pi^\pm)$. The acceptance ratio, $\epsilon^{\mathrm{rel}}(X)$, is calculated as an average over the events included in the $m(B_s^0\,\pi^\pm)$ interval within which the search for a resonance is performed.

The width of this interval is defined by a BW function convolved with the mass resolution function, with the start and end points of the range chosen to include 99% of the signal events. The uncertainty of $\epsilon^{\mathrm{rel}}(X)$ is calculated by varying the fitted parameters of the MC-based function used to describe the acceptance as a function of $p_{\mathrm{T}}(B_s^0)$ within their uncertainties. Small variations of this function due to the pseudorapidity of the B_s^0 were investigated and are included in the systematic uncertainties. The error also includes the uncertainty in the number of data events used in the average and the statistical uncertainty in the $p_{\mathrm{T}}(B_s^0)$ distribution of these events. The error in the pion reconstruction efficiency, arising from uncertainties in the amount of ID material, is found to have a negligible effect on ρ_X.

As no significant signal is observed, corresponding to the properties of the $X(5568)$ as reported by Ref. [1], upper limits are determined for the number of $B_s^0\,\pi^\pm$ signal events, $N(X)$, and for the relative production rate, ρ_X. These are calculated using the asymptotic approximation from the profile likelihood formalism [20] based on the $\mathrm{CL_s}$ frequentist method [21]. To establish the limit on the number of $B_s^0\,\pi^\pm$ signal events, the PDF models for signal and background, defined respectively by Eqs. (1) and (2), are used as inputs to the $\mathrm{CL_s}$ method. Without systematic uncertainties, the extracted upper limits at 95% CL are $N(X) < 264$ for $p_{\mathrm{T}}(B_s^0) > 10$ GeV and $N(X) < 213$ for $p_{\mathrm{T}}(B_s^0) > 15$ GeV. Systematic uncertainties affecting these limits are included in the determination of $N(X)$. To obtain results that can be compared to the state $X(5568)$ reported by the D0 Collaboration, systematic uncertainties are assigned by varying the values of m_X and Γ_X independently within Gaussian constraints, with uncertainties equal to those quoted in Ref. [1]. The default model of the X resonance, which is assumed to be spinless, is changed to a BW P-wave resonance. To include the systematic uncertainty due to the modeling of the background, the default PDF of Eq. (2) is replaced by a seventh-order Chebyshev polynomial, allowing more free parameters in the fit. For the detector resolution, the default per-candidate mass resolution model is replaced by the sum of three Gaussian functions with a common mean. The parameters used are determined from the $B_s^0\,\pi^\pm$ MC sample. Using these alternative models, upper limits that include systematic uncertainties are extracted, leading to values $N(X) < 382$ for $p_{\mathrm{T}}(B_s^0) > 10$ GeV and $N(X) < 356$ for $p_{\mathrm{T}}(B_s^0) > 15$ GeV. To extract the upper limits on ρ_X additional systematic uncertainties are included. The calculation of ρ_X also depends on the precision of extracting the number of B_s^0 signal events and the relative efficiency $\epsilon^{\mathrm{rel}}(X)$. To include these uncertainties, the central values and the uncertainties of the number of B_s^0 signal events and $\epsilon^{\mathrm{rel}}(X)$ are used to construct Gaussian constraints, which are included as additional inputs to the $\mathrm{CL_s}$ method. Both the statistical and systematic uncertainties are included after being summed in quadrature. For the B_s^0 signal, the default fit model of two Gaussian functions is changed to a triple Gaussian function and the change in the result is taken as a systematic uncertainty. The uncertainty due to the proper decay time requirement $t > 0.2$ ps was estimated by varying it within the time resolution and found to be negligible. The resulting upper limits at 95% CL are $\rho_X < 0.015$ for $p_{\mathrm{T}}(B_s^0) > 10$ GeV and $\rho_X < 0.016$ for $p_{\mathrm{T}}(B_s^0) > 15$ GeV. A hypothesis test is performed for the presence of a $B_s^0\,\pi^\pm$ peak for every 5 MeV step in its mass from 5550 MeV to 5700 MeV, assuming a resonant state as described by Eq. (1), with a BW width of 21.9 MeV [1] and $p_{\mathrm{T}}(B_s^0) > 10$ GeV. For each $B_s^0\,\pi^\pm$ mass tested, $\epsilon^{\mathrm{rel}}(X)$ is calculated using the same method as for $X(5568)$. The values of $\epsilon^{\mathrm{rel}}(X)$ vary from 0.50 to 0.55 in the search interval. The upper limit of ρ_X at 95% CL is determined for each tested mass. The same systematic uncertainties as in the determination of ρ_X for the state $X(5568)$ are included, with the exception of the $X(5568)$ mass uncertainty. The median expected upper limit at 95% CL as a function of the $B_s^0\,\pi^\pm$ mass is also determined with $\pm 1\sigma$ and $\pm 2\sigma$ error bands. The results are shown in Figure 3.

In conclusion, a search for a new state $X(5568)$ decaying to $B_s^0\,\pi^\pm$, with properties as reported by the D0 Collaboration, was performed by the ATLAS experiment at the LHC, using $4.9\,\mathrm{fb}^{-1}$ of pp collision data at 7 TeV and $19.5\,\mathrm{fb}^{-1}$ at 8 TeV. No significant signal was found. Within the acceptance in which this analysis is performed, upper limits on the number of signal events, $N(X)$, and on the X production

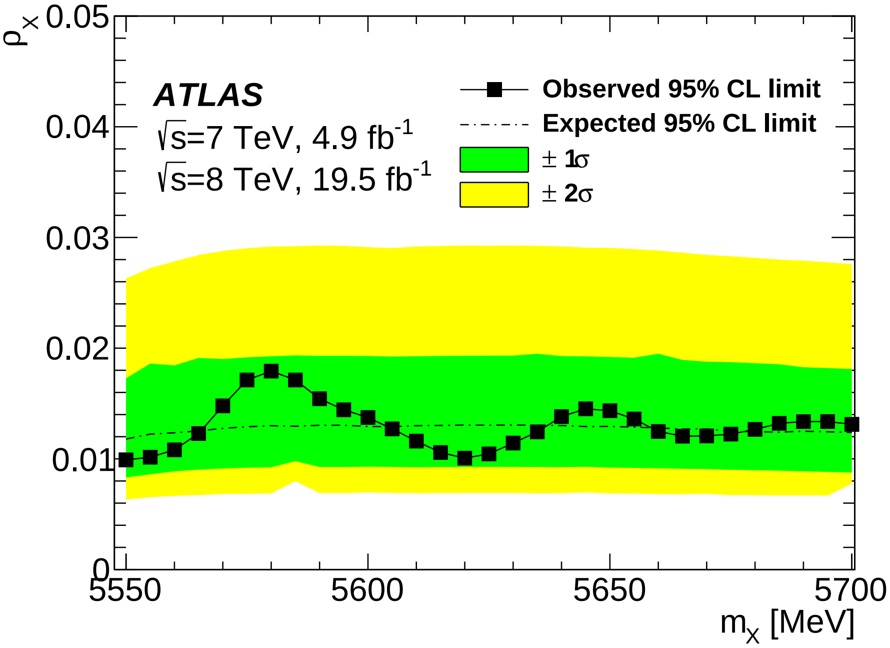

Figure 3: Upper limits on ρ_X at 95% CL (black squares connected by line) at different masses of a hypothetical resonant state X decaying to $B_s^0\,\pi^\pm$, for events with $p_{\mathrm{T}}(B_s^0) > 10$ GeV. A BW width of $21.9 \pm 6.4(\mathrm{stat})^{+5.0}_{-2.5}(\mathrm{syst})$ MeV is assumed, as reported by D0. The values include systematic uncertainties. The expected 95% CL upper limits (central black dot-dashed line) with $\pm 1\sigma$ (green) and $\pm 2\sigma$ (yellow) uncertainty bands on ρ_X are shown as a function of the assumed resonance mass.

rate relative to B_s^0 mesons, were determined at 95% CL, resulting in $N(X) < 382$ and $\rho_X < 0.015$ for $p_{\mathrm{T}}(B_s^0) > 10$ GeV, and $N(X) < 356$ and $\rho_X < 0.016$ for $p_{\mathrm{T}}(B_s^0) > 15$ GeV. Limits are also set for potential $B_s^0\,\pi^\pm$ resonances in the mass range from 5550 MeV to 5700 MeV. Across the full range, the upper limit set on ρ_X at 95% CL varies between 0.010 and 0.018, and does not exceed the $\pm 1\sigma$ error band from the expected limit.

We thank CERN for the very successful operation of the LHC, as well as the support staff from our institutions without whom ATLAS could not be operated efficiently.

We acknowledge the support of ANPCyT, Argentina; YerPhI, Armenia; ARC, Australia; BMWFW and FWF, Austria; ANAS, Azerbaijan; SSTC, Belarus; CNPq and FAPESP, Brazil; NSERC, NRC and CFI, Canada; CERN; CONICYT, Chile; CAS, MOST and NSFC, China; COLCIENCIAS, Colombia; MSMT CR, MPO CR and VSC CR, Czech Republic; DNRF and DNSRC, Denmark; IN2P3-CNRS, CEA-DRF/IRFU, France; SRNSFG, Georgia; BMBF, HGF, and MPG, Germany; GSRT, Greece; RGC, Hong Kong SAR, China; ISF, I-CORE and Benoziyo Center, Israel; INFN, Italy; MEXT and JSPS, Japan; CNRST, Morocco; NWO, Netherlands; RCN, Norway; MNiSW and NCN, Poland; FCT, Portugal; MNE/IFA, Romania; MES of Russia and NRC KI, Russian Federation; JINR; MESTD, Serbia; MSSR, Slovakia; ARRS and MIZŠ, Slovenia; DST/NRF, South Africa; MINECO, Spain; SRC and Wallenberg Foundation, Sweden; SERI, SNSF and Cantons of Bern and Geneva, Switzerland; MOST, Taiwan; TAEK, Turkey; STFC, United Kingdom; DOE and NSF, United States of America. In addition, individual groups and members have received support from BCKDF, the Canada Council, CANARIE, CRC, Compute Canada, FQRNT, and the Ontario Innovation Trust, Canada; EPLANET, ERC, ERDF, FP7, Horizon 2020 and Marie Skłodowska-Curie Actions, European Union; Investissements d'Avenir Labex and Idex, ANR, Région Auvergne and Fondation Partager le Savoir, France; DFG and AvH Foundation, Germany; Herakleitos, Thales and Aristeia programmes co-financed by EU-ESF and the Greek NSRF; BSF, GIF and Minerva, Israel; BRF, Norway; CERCA Programme Generalitat de Catalunya, Generalitat Valenciana, Spain; the Royal Society and Leverhulme Trust, United Kingdom.

The crucial computing support from all WLCG partners is acknowledged gratefully, in particular from CERN, the ATLAS Tier-1 facilities at TRIUMF (Canada), NDGF (Denmark, Norway, Sweden), CC-IN2P3 (France), KIT/GridKA (Germany), INFN-CNAF (Italy), NL-T1 (Netherlands), PIC (Spain), ASGC (Taiwan), RAL (UK) and BNL (USA), the Tier-2 facilities worldwide and large non-WLCG resource providers. Major contributors of computing resources are listed in Ref. [22].

References

[1] D0 Collaboration, *Evidence for a $B_s^0\pi^\pm$ State*, Phys. Rev. Lett. **117** (2016) 022003, arXiv: `1602.07588 [hep-ex]`.

[2] W. Wang and R. Zhu, *Can $X(5568)$ be a tetraquark state?* Chin. Phys. C **40** (2016) 093101, arXiv: `1602.08806 [hep-ph]`.

[3] W. Chen et al., *Decoding the $X(5568)$ as a Fully Open-Flavor $su\bar{b}\bar{d}$ Tetraquark State*, Phys. Rev. Lett. **117** (2016) 022002, arXiv: `1602.08916 [hep-ph]`.

[4] Y.-R. Liu, X. Liu, and S.-L. Zhu, $X(5568)$ *and its partner states*, Phys. Rev. D **93** (2016) 074023, arXiv: `1603.01131 [hep-ph]`.

[5] Z.-G. Wang, *Analysis of the strong decay $X(5568) \to B_s^0\pi^+$ with QCD sum rules*, Eur. Phys. J. C **76** (2016) 279, arXiv: `1603.02498 [hep-ph]`.

[6] F. Stancu, $X(5568)$ *as a $su\bar{d}\bar{b}$ tetraquark in a simple quark model*, J. Phys. G **43** (2016) 105001, arXiv: `1603.03322 [hep-ph]`.

[7] D0 Collaboration, *Study of the $X^\pm(5568)$ state with semileptonic decays of the B_s^0 meson*, (2017), arXiv: `1712.10176 [hep-ex]`.

[8] LHCb Collaboration, *Search for Structure in the $B_s^0\pi^\pm$ Invariant Mass Spectrum*, Phys. Rev. Lett. **117** (2016) 152003, arXiv: `1608.00435 [hep-ex]`.

[9] CMS Collaboration, *Search for the $X(5568)$ state decaying into $B_s^0\pi^\pm$ in proton–proton collisions at $\sqrt{s} = 8$ TeV*, (2017), arXiv: `1712.06144 [hep-ex]`.

[10] CDF Collaboration, *A Search for the exotic meson $X(5568)$ with the Collider Detector at Fermilab*, (2017), arXiv: `1712.09620 [hep-ex]`.

[11] ATLAS Collaboration, *The ATLAS Experiment at the CERN Large Hadron Collider*, JINST **3** (2008) S08003.

[12] T. Sjöstrand, S. Mrenna, and P. Z. Skands, *PYTHIA 6.4 physics and manual*, JHEP **05** (2006) 026, arXiv: `hep-ph/0603175`.

[13] T. Sjöstrand, S. Mrenna, and P. Z. Skands, *A brief introduction to PYTHIA 8.1*, Comput. Phys. Commun. **178** (2008) 852, arXiv: `0710.3820 [hep-ph]`.

[14] ATLAS Collaboration, *ATLAS tunes of* PYTHIA *6 and Pythia 8 for MC11*, ATL-PHYS-PUB-2011-009, 2011, URL: `https://cds.cern.ch/record/1363300`.

[15] ATLAS Collaboration, *The ATLAS Simulation Infrastructure*, Eur. Phys. J. C **70** (2010) 823, arXiv: `1005.4568 [physics.ins-det]`.

[16] S. Agostinelli et al., *GEANT4: a simulation toolkit*, Nucl. Instrum. Meth. A **506** (2003) 250.

[17] ATLAS Collaboration, *Performance of the ATLAS muon trigger in pp collisions at* $\sqrt{s} = 8$ *TeV*, Eur. Phys. J. C **75** (2015) 120, arXiv: `1408.3179 [hep-ex]`.

[18] ATLAS Collaboration, *Measurement of the CP-violating phase* ϕ_s *and the* B_s^0 *meson decay width difference with* $B_s^0 \to J/\psi\phi$ *decays in ATLAS*, JHEP **08** (2016) 147, arXiv: `1601.03297 [hep-ex]`.

[19] C. Patrignani (Particle Data Group), *Review of Particle Physics*, Chin. Phys. C **40** (2016) 100001.

[20] G. Cowan, K. Cranmer, E. Gross, and O. Vitells, *Asymptotic formulae for likelihood-based tests of new physics*, Eur. Phys. J. C **71** (2011) 1554, arXiv: `1007.1727 [physics.data-an]`, Erratum: Eur. Phys. J. C **73** (2013) 2501.

[21] A. L. Read, *Presentation of search results: the* CL_S *technique*, J. Phys. G **28** (2002) 2693.

[22] ATLAS Collaboration, *ATLAS Computing Acknowledgements*, ATL-GEN-PUB-2016-002, URL: `https://cds.cern.ch/record/2202407`.

Appendix B

Curriculum Vitæ

The author's curriculum vitæ, a list of publications, and a list of conference contributions are presented on the following pages.

Tomáš Jakoubek

`https://linkedin.com/in/tomasjakoubek`
tomas.jakoubek@cern.ch

Education

2011 - today **Ph.D. candidate in particle physics**,
Czech Technical University in Prague, Faculty of Nuclear Sciences and Physical Engineering,
High Precision CP*-Violation Measurements in Flavour Physics at the ATLAS Experiment.*

2009 - 2011 **Master degree (Ing.) in particle physics**,
Czech Technical University in Prague, Faculty of Nuclear Sciences and Physical Engineering,
Physics properties of J/ψ *events in testing of Inner Detector performance.*

2005 - 2009 **Bachelor degree (Bc.) in particle physics**,
Czech Technical University in Prague, Faculty of Nuclear Sciences and Physical Engineering,
ATLAS Inner Detector and its Testing with Cosmic Muons.

Professional Experience

2007 - today **ATLAS Collaboration Membership**,
CERN, Geneve, Switzerland.

- Trigger B-physics and Light States Signature Coordinator (starting from 10/2018),
- Physics analysis in B-physics group,
- Development of a common software framework for the analysis team,
- Inner Detector operator.

2007 - today	**Research Associate** at Institute of Physics of the Academy of Sciences of the Czech Republic. • Physics analysis and performance studies for the ATLAS experiment.
2009 - 2017	**Teaching Assistant** at Czech Technical University in Prague, Faculty of Nuclear Sciences and Physical Engineering. • Laboratory courses for undergraduate students, • Bachelor students supervision (09/2014 - 09/2017).

Schools and Courses

2008 - 2011	Lectures of CERN Summer Student Programme, CERN, Geneve, Switzerland.
05/2009	The XIV LNF Spring School “Bruno Touschek” in Nuclear, Subnuclear and Astroparticle Physics, Frascati, Italy.
12/2008	PASC Winter School, Sesimbra, Portugal.

Other Activities

2009 - 2015	Main organiser of an annual “Workshop of Experimental Nuclear and Particle Physics”, Bílý Potok, Czech Republic.
2013 - 2015	Supervisor at “RATAB” (summer camp for high school students), planning and supervision of physical and psychological games.

Skills and Expertise

Languages	English (advanced); German, French (basic conversation); Czech (native).
General	Statistical analysis, Scientific writing, Presentation skills, Driving license.

Soft skills	Presented scientific results at major scientific conferences, Lectures for academic purposes, teaching, Public lectures on various topics from High Energy Physics.
Computers	C++, BASH, Python, PHP, MySQL, HTML, XML, CSS, ROOT, Athena, MATLAB, Mathematica, GNU/Linux, Microsoft Windows, GIT, Subversion, LaTeX, LibreOffice, Microsoft Office.

Personal Life, Interests

Science and technology,
Travelling and sports (hiking, skydiving, sailing, skiing, strength training),
Literature (especially sci-fi), music (guitar playing), art.

List of Publications

ATLAS Collaboration, *Search for a Structure in the* $B_s^0\pi^\pm$ *Invariant Mass Spectrum with the ATLAS Experiment*, Phys. Rev. Lett. **120** (2018) no.20, 202007.

ATLAS Collaboration, *Measurement of the CP-violating phase* ϕ_s *and the* B_s^0 *meson decay width difference with* $B_s^0 \to J/\psi\phi$ *decays in ATLAS*, JHEP **1608** (2016) 147.

ATLAS Collaboration, *Flavor tagged time-dependent angular analysis of the* $B_s \to J/\psi\phi$ *decay and extraction of* $\Delta\Gamma_s$ *and the weak phase* ϕ_s *in ATLAS*, Phys. Rev. D **90** (2014) no.5, 052007.

ATLAS Collaboration, *Time-dependent angular analysis of the decay* $B_s^0 \to J/\psi\phi$ *and extraction of* $\Delta\Gamma_s$ *and the CP-violating weak phase* ϕ_s *by ATLAS*, JHEP **1212** (2012) 072.

List of Notes

ATLAS collaboration, $B^\pm$ *mass reconstruction in* $B^\pm \to J/\psi K^\pm$ *decay at ATLAS at 13 TeV pp collisions at the LHC*, ATLAS-CONF-2015-064.

List of Conference Contributions

T. Jakoubek (on behalf of the ATLAS collaboration), *B-physics studies for HL-LHC ATLAS upgrade*, PoS FPCP **2017** (2017) 045. Poster at "15th meeting in the conference series of Flavor Physics & CP Violation" (06/2017, Prague, Czech Republic).

T. Jakoubek (on behalf of the ATLAS collaboration), *Recents results from ATLAS in beauty and charm physics*. Talk at "Lake Louise Winter Institute 2017" (02/2017, Lake Louise, Canada).

T. Jakoubek (on behalf of the ATLAS collaboration), *Measurement of* CP *violation and mixing in* $B_s \to J/\psi\phi$ *in ATLAS*, PoS BEAUTY **2016** (2016) 067. Poster at "The 16th International Conference on B-Physics at Frontier Machines" (05/2016, Marseille, France).

T. Jakoubek (on behalf of the ATLAS collaboration), *Flavour-tagged time-dependent angular analysis of the* $B_s^0 \to J/\psi(\mu^+\mu^-)\phi(K^+K^-)$ *decay with the ATLAS detector*. Poster at "Lake Louise Winter Institute 2015" (02/2015, Lake Louise, Canada).

T. Jakoubek (on behalf of the ATLAS collaboration), *Flavour tagging techniques for CPV studies in the* B_s *system with ATLAS*, arXiv:1410.8732 [hep-ex]. Poster at "50 years of CP-violation" (07/2014, Queen Mary University of London, UK).

T. Jakoubek (on behalf of the ATLAS collaboration), *B-hadrons spectroscopy and decay properties with the ATLAS experiment*, Nucl. Part. Phys. Proc. **258-259** (2015) 125. Talk at "17th High-Energy Physics International Conference in Quantum Chromodynamics" (06/2014, Montpellier, France).

T. Jakoubek (on behalf of the ATLAS collaboration), *Production of beauty and quarkonia in ATLAS*, J. Phys. Conf. Ser. **455** (2013) 012018. Talk at "Kruger 2012: Workshop on Discovery Physics at the LHC" (12/2012, Kruger National Park, South Africa).